

GEOGRAPHISCHE INSTITUTE DER
RHEINISCHEN FRIEDRICH-WILHELMS-UNIVERSITÄT BONN

ESTIMATION OF WATER STORAGE CAPACITY AND EVAPORATION
LOSSES OF SMALL RESERVOIRS IN THE UPPER EAST REGION OF
GHANA

DIPLOMA THESIS

SUPERVISOR:

PROF. DR. B. DIEKKRÜGER

SUBMITTED BY
JENS LIEBE

BONN,
SEPTEMBER 2002

Table of Contents

Table of Contents.....	<i>ii</i>
Figures & Tables.....	<i>iv</i>
Abbreviations.....	<i>vi</i>
1. Introduction	1
2. The Upper East Region of Ghana and Reservoir Basics	4
2.1 Location and socio-economic attributes	4
2.2 Environmental Properties	6
2.2.1 Climate and rainfall characteristics	6
2.2.2 Vegetation and Agro-Ecological Zones	11
2.2.3 Geology and Relief	13
2.2.4 Drainage systems and Water Balance	14
2.3 General Properties of Reservoirs	18
3. Materials and Methods	21
3.1 Evaporation from surface water bodies	21
3.2 The Landsat 7 ETM+ System and Remote Sensing of Surface Water Bodies	23
3.2.1 Characteristics of Landsat 7 ETM+ - a brief overview	23
3.2.2 Influence of date selection on classification results	24
3.2.3 Water body Detection with LANDSAT ETM+ and the reflectance properties of surface water bodies	25
3.2.4 Pre-processing, classification and data extraction	28
3.3 Collection and Processing of Field Data	33
3.3.1 Set-up and realization of field work	33
3.3.2 Modeling of reservoirs and volume derivation	35
4. Data Description and Results	38
4.1 General Distribution of Reservoir Sizes	38
4.2 Spatial distribution of Reservoirs and Reservoir Sizes throughout Upper East Region.....	40
5. Data Analysis	46
5.1 Examination of postulated relations	46
5.1.1 Area _(Satellite) – Area _(Field) – Correlation	46
5.1.2 Area _(Field) – Volume – Correlation	51
5.2 Exploration and use of Depth-Area-Volume interrelations	54
5.2.1 General approach	54
5.2.2 Derivation of Area – Volume – Curve	56
5.2.3 Derivation of Depth – Volume – Curve	59
5.2.4 Creation of a “Super-Reservoir”	60
5.3 Evaporation losses from the Super Reservoir	69
5.4 Outlook	73
6. Conclusion	76
Literature	78
WWW – sources	82

Appendices	85
Appendix 1: Summary of Climatic Data at Navrongo	86
Appendix 2: Characteristic Rainfall Patterns for different types of Rainfall	87
Appendix 3: The Upper East Region of Ghana within the Volta Basin	88
Appendix 4: Technical Summary of evaporation calculation with CRU-Data	89
Appendix 5: Landsat and CRU Coverage	91
Appendix 6 : LANDSAT ETM+ Scene Parameters	92
Appendix 7: Spatial Average Rainfall Estimates (RFE) for Ghana	94
Appendix 8: Effect of Bushfires	95
Appendix 9: ID and sizes of the randomly selected reservoirs	96
Appendix 10: Surfer script for 0-replacement of blanking value	97
Appendix 11: Area _(Satellite) -Area _(Field) Deviations in hectares and NDAI	98
Appendix 12: IDL-Routine to calculate each reservoirs area and volume at all depth steps of 5 cm	99
Appendix 13: Equation variables for logArea-logVolume Relations	101
Appendix 14: Variables for Equations used for logDepth-logVolume extrapolation	102
Appendix 15: Variables for Equations used for logDepth-logArea extrapolation	103
Appendix 16: Equation variables for extrapolated logDepth-logVolume Relations	104
Appendix 17: Equation variables for extrapolated logArea-logVolume Relations	105
Appendix 18: Equation variables for extrapolated logArea-logDepth Relations	106

Figures & Tables

Figure 1: The Upper East Region of Ghana and its districts	4
Figure 2: Climatic Data for Navrongo.....	6
Figure 3a: Structure of the Intertropical Front over western Africa in northern summer.....	8
Figure 3b: Navrongo’s membership to different weather zones in the course of a year.....	8
Figure 4: Surface and vertical view of a squall line.....	9
Figure 5: TRMM scene and associated rainfall of a squall line that passed Northern Ghana on the 09.09.2001.....	10
Figure 6: Monthly rainfall and the proportion of monthly rainfall due to line squalls (shaded) in 1955 in Navrongo/Ghana.....	11
Figure 7: The vegetation zones of West Africa.....	12
Figure 8: Elevation Model (TIN) of the Upper East.....	14
Figure 9: System of stream-ordering after Horton-Strahler.....	15
Figure 10: Valley head, midstream part and downstream part of Inland Valleys.....	16
Figure 11: Valley cross-sections.....	17
Figure 12: Water Budget for Navrongo.....	18
Figure 13: Seasonal Rainfall in Northern Ghana for 1998 and 1999 (in mm)	25
Figure 14: Reflectance vs. Wavelength for soil, vegetation and water.....	26
Figure 15: Spectral reflectance curve for surface water layer (solid line) and 20m (dashed)	26
Figure 16: Processes acting on solar radiant energy in the visible part of the spectrum over an area of shallow water.....	26
Figure 17: Possible reflectance curves of water bodies (relative reflectances).	27
Figure 18: Arrangement of compact sub-classes in the Feature Space.....	29
Figure 19: Equi-probability contours as used in Maximum Likelihood classification.....	29
Figure 20: Size distribution of reservoirs and categorization.....	32
Figure 21: 3D model of Reservoir No. 101 and distribution of measurements.....	37
Figure 22: Frequency Distribution of Reservoir Sizes.....	39
Figure 23: Distribution of Reservoir Sizes with regard to administrating boundaries.....	41
Figure 24: Distribution of Reservoir Sizes with regard to infrastructure and political units/boundaries.....	42
Figure 25: Distribution of Reservoirs with respect to Upper East’s Topography.....	43
Figure 26: Distribution of Measured Reservoirs.....	45
Figure 27: $Area_{(Satellite)}-Area_{(Field)}$ correlation.....	47
Figure 28: Normalized Difference Area Index of surface areas between 1999 and 2002.....	49
Figure 29: Herbaceous water plants in the tail part of reservoir No. 282.....	50
Figure 30: $\log Area_{(Field)}-\log Volume$ relation.....	53
Figure 31: Area-, Depth-, and Volume-Interrelations of reservoirs.....	55
Figure 32: $\log Area-\log Volume$ correlation.....	57
Figure 33: Distribution of a and b from the $\log Area-\log Volume$ equations of the form $(y = ax +b)$	58
Figure 34: $\log Depth-\log Volume$ correlation.....	59
Figure 35: Creation of a Super-Reservoir.....	60
Figure 36: Data Extrapolation of field measurements to maximum dimensions (defined by spillway, $d+\Delta h_{max}$) and derivation of reservoir dimensions for Nov. 1999.....	62
Figure 37: Possible source of error in depth derivation by surface area.....	63
Figure 38: Area-Volume relation based on reservoir data extrapolated to 1999 level.....	64
Figure 39: $Area_{-average}Depth$ -relation based on reservoir data extrapolated to 1999 level.....	65
Figure 40: Depth-Volume curve from extrapolated data.....	66
Figure 41: Super Reservoir in evaporation-mode.....	68

Figure 42: Super Reservoir in fill-mode.....	69
Figure 43: Decadal (1986-1995) monthly averages of Potential Evaporation.....	70
Figure 44: Estimation of Evaporation losses from the Super Reservoir.....	71
Figure 45: Worst-case Estimation of Evaporation losses from the Super Reservoir.....	72
Figure 46: Reservoir shapes regarding their flexion.....	74
Figure 47: Relation of in- and encircle dimensions for different reservoir shapes.....	75
Table 1: Relief Properties of the Upper East Region.....	13
Table 2: Spectral and Spatial Resolution of the Landsat 7 ETM+ Sensor.....	23
Table 3: Equipment used for the collection and handling of the field data.....	33
Table 4: Reservoir Frequency and Area Distribution by District.....	42

Abbreviations

AEJ	African Easterly Jet
AEZ	Agro Ecological Zone
AVG	Average
CDF	Cumulative Density Function
CORREL	Coefficient of correlation
COST	Atmospheric correction using the cosine of the solar zenith angle
CRU	Climate Research Unit
DOS	Dark Object Subtraction
ERS	European Remote Sensing Satellite
E_a	Actual Evaporation
E_p	Potential Evaporation
E_o	Reference Evaporation
ET_o	Reference Evapotranspiration
ET_p	Potential Evapotranspiration
ETM +	Enhanced Thematic Mapper Plus
GPS	Global Positioning System
ICOUR	Irrigation Company of Upper Region
ID	Identifier
IDL	Interactive Data Language
IR	Infra-Red part of the electromagnetic spectrum
ITCZ	Intertropical Convergence Zone
ITD	Intertropical Discontinuity
Log	Logarithm
NDAI	Normalized Difference Area Index
NDWI	Normalized Difference Water Index
RFE	Rainfall Intensity Estimate
RGB	band combination in the red/green/blue color space
RS	Remote Sensing
STD	Standard deviation
TIN	Triangulated Irregular Network
TM	Thematic Mapper
TRMM	Tropical Rainfall Measuring Mission
RMS	Root Mean Square Error
UNEP	United Nations Environment Programme
UTM	Universal Transverse Mercator
VIS	Visible part of the electromagnetic spectrum
WEAP	Water Evaluation And Planning System
WMO	World Meteorological Organization
WRS	Worldwide Reference System
3D	Three Dimensional

Chapter 1

Introduction

Ghana's fame on the subject of reservoirs is undoubtedly due to Lake Volta, the largest man made lake of the world regarding its surface extent. After the dam was closed near Akosombo in 1963 the water of the Black and White Volta, and the Oti River flooded an area of 8,515 km² (148 km³). Large dams dominate the controversial discussion whose matter found an institutional forum with the World Commission on Dams (UNEP). Moving the focus away from reservoirs of such spectacular dimensions to the other extreme, we find a large number of small reservoirs. Not only in the Upper East Region of Ghana, where this study is conducted, but also in most other semi-arid environments, these are of utmost importance for the water supply of the mainly rural population. Rainfed and some irrigated agriculture are the backbone in their society and, for a majority the principle source of income. Population growth furthermore places additional pressure on land and water resources (GLOWA VOLTA PROJECT PROPOSAL 1999, p. 3). For these rural societies, surface water is a scarce and valuable resource, and dam development is crucial for economic development and of vital interest for their agricultural subsistence. The collection of water in these small water bodies allows dry-season farming and contributes to even out the seasonality of workload and income.

A conclusion drawn from the International Conference on Freshwater that was held in Bonn in December 2001 is that "policies for all aspects of water should be clearly linked to policies for poverty reduction and economic growth. Governments should review the priority given to water [...] and to productive water infrastructure in national and international programmes to tackle poverty" (INTERNATIONAL CONFERENCE ON FRESHWATER 2002, p. 25). Yet,

these policies must rest upon scientifically sound decisions if they claim to be termed sustainable policies.

Small dams represent an adequate tool to manage fresh water storage and its timely distribution and use. The special appeal of small dams is that their construction requires comparably little expenditure. The construction of small reservoirs in larger numbers and well spread throughout a region reaches a wide population and facilitates its water demands. This, in turn, has feedback effects on the environment that need not to be waved away. Dam development needs to be pursued in a strategic manner and requires water resources management and planning that takes into account these effects. While their widespread distribution has the advantage of serving many people, in turn it complicates the evaluation of their environmental effects. Questions that need to be addressed are, amongst many others, where further dam development can take place without affecting already existing reservoirs, and whether the costs of increased evaporation losses as induced from the newly created water bodies are in a justifiable relation to their benefit.

To answer these questions from a hydrologic point of view, their recent existence in number, as well as their distribution and reservoir storage volumes must be known. The absence of knowledge on reservoir storage volumes is a constraint that needs to be included in such an evaluation.

This thesis seeks to find a methodology that makes it possible to estimate storage volumes of reservoirs as a function of their surface area. Knowledge of such a function allows calculating reservoir volumes on the basis of remotely sensed data. Satellite images were evaluated in order to receive up-to-date baseline data on reservoirs in the Upper East Region of Ghana, giving information on their spatial distribution and surface extent. In an extensive field campaign, 61 reservoirs were precisely measured and modeled to derive regularities and interrelations between the three variables 'area', 'depth', and 'volume'. Transferring their geometric properties into a generalized equation allows the estimation of storage volumes based on surface areas. In combination with remotely sensed reservoir surface areas, this relation can be utilized to make reservoir volume inventories on regional or even higher level.

The second aim is to use such a dataset to evaluate evaporation losses from reservoir surface areas. In contrast to evapotranspiration from adjacent irrigation-fields where water is productively used for crop growth, the evaporation losses that directly occur from the reservoir surface are unproductive losses. Volumes and evaporation losses can then be compared. The determination of evaporation losses in the course of a year, gives a better overview of the amounts of water that are available at different times.

The study is conducted as an integral part of the GLOWA Volta Project, an interdisciplinary research project with focus on ‘Sustainable Water Use under Changing Land Use, Rainfall Reliability and Water Demands in the Volta Basin’. Its objective is to develop a “scientifically sound decision support system for the assessment, sustainable use and development of water resources in the Volta Basin” (GLOWA VOLTA PROJECT PROPOSAL 1999, p. 3). Therein, the Upper East Region of Ghana was identified as a hot spot of land use change, which also includes the dam development that took place in the last decades (GLOWA VOLTA ANNUAL REPORT 2001 2002, pp. Land use 7 – 8; VAN DE GIESEN et al. 2002, pp. 164-167). Recently, the Water Resources Commission (WRC) of Ghana accommodated the water related problems as they exist in the Upper East Region by designating this region as pilot project on water resources management and improving water use efficiency in this Region.

To give a brief outline on the flow of the thesis, the following chapter gives an overview on the Upper East Region of Ghana and its environmental properties. Emphasis is set on those factors that are attached the greatest importance to regarding the further work. Chapter 3 explains the methods and underlying theories that were used to generate, process and evaluate the data used in this study. Upon the description of reservoir distributions in Chapter 4, the focus is then set on the evaluation of reservoir properties. These are finally used to estimate the reservoir storage capacity of the Upper East Region, and to calculate the evaporation losses.

Chapter 2

The Upper East Region of Ghana and Reservoir Basics

2.1 Location and socio-economic attributes

The Upper East Region of Ghana is the north-easternmost of Ghana's ten regions. To the west, it borders the Upper West region and on its southern side the Northern Region. Its

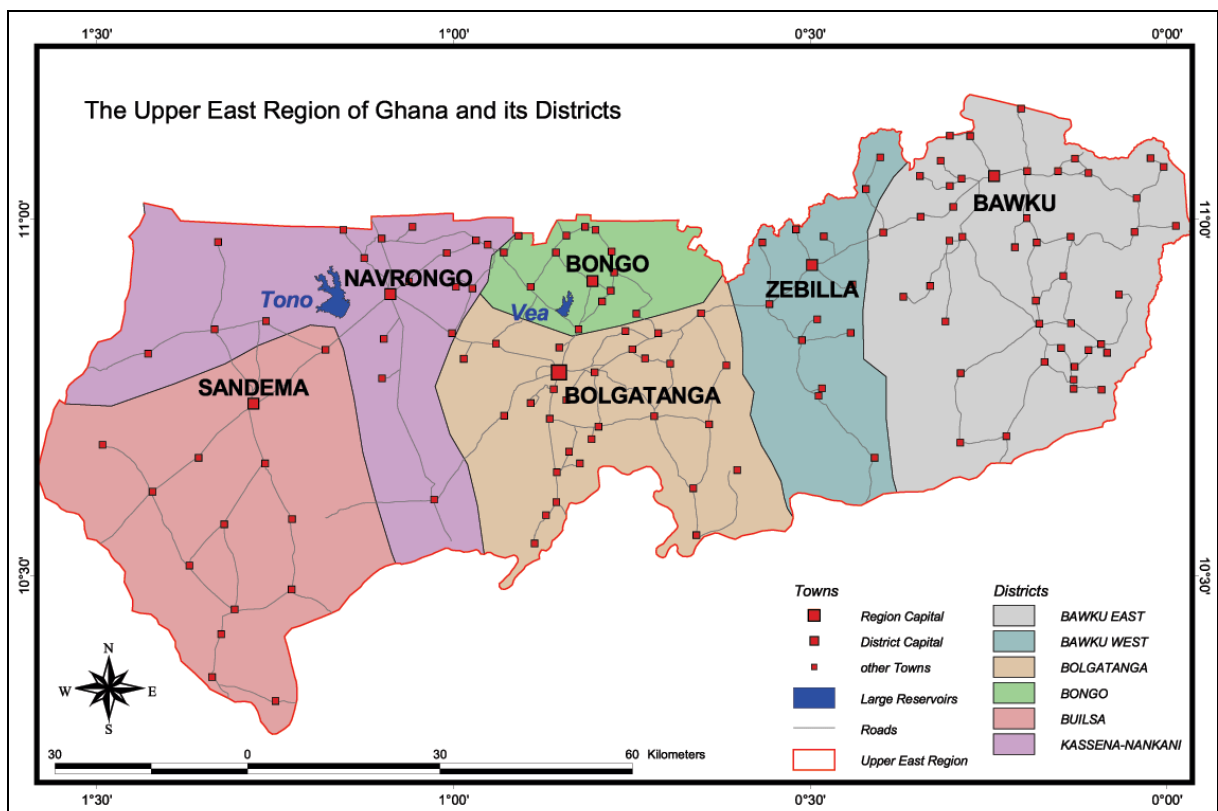


Figure 1: The Upper East Region of Ghana and its districts.

The Upper East Region of Ghana consists of six districts. Its regional capital is Bolgatanga. To the north, the Upper East shares its boundary with Burkina Faso, and to the east with Togo.

northern and eastern boundaries are international boundaries. North of the Upper East region lies Burkina Faso, whereas to the east is Togo. The Region splits up into six districts (Figure 1).

Approximately one million people inhabit the Upper East Region (ASENSO-OKYERE et al. 2000, p. 1), which has a population density of 96.5 inhabitants/km² (SCHMIDT-KALLERT 1994, p. 217). In comparison with the mean annual household incomes of other regions of Ghana, the Upper East holds the second last rank (1,446,000 Cedis¹) with an almost negligible surplus of 2000 Cedis (≈ 0.33 €) ahead of the adjacent Upper West Region. With a poverty² incidence of 88 % in 1998/1999 (GHANA STATISTICAL SERVICE 2000, p. 12-14), the Upper East is the region with the largest portion of poor people. Together with the Upper West Region, the Upper East is the economic rearlight within the general north-south contrast. The household income structure predominantly composes of “household agricultural income” (63.6 %), “non-farm self-employment” (15 %) and “wage income from employment” (12.9 %). In addition, Ghana’s largest irrigation schemes are situated in the Upper East Region. The Irrigation Company of Upper Region (ICOUR) manages the two largest schemes at Tono and Veve (Figure 1), which were constructed in the mid-80s. The major irrigated crops in these schemes are rice, tomatoes, and soybeans, which in smaller schemes are supplemented with onions, okra, pepper, aubergines, cowpeas and maize. Groundnuts are a common dry-farming crop. Besides its dominant role in the composition of household incomes, agricultural production is also a vital to the Upper East’s food supply (ASENSO-OKYERE et al. 2000, pp.72-73, 84, 100-104).

Almost a quarter century ago, OBOLI wrote about the north-south contrast in agricultural production that “the north is much poorer, living mainly on subsistence farming, and is faced with the severe problem of water-supply, climatic severity, distance from ports and poverty” (1978, p 111). This sentence is still valid.

¹ Conversion is 1€ \approx 8500 Ghanaian Cedis (rate of 26.08.2002)

² The poverty line was defined as 900,000 Ghanaian Cedis (GHANA STATISTICAL SERVICE 2000, p. 12-14).

2.2 Environmental Properties

2.2.1 Climate and rainfall characteristics

In a general climatic characterization, the Upper East Region belongs to the semi-arid tropics. Climatologically, they are defined by an average monthly rainfall that exceeds potential evaporation for 2-7 months per year with an average monthly temperature above 18°C (KASEI 1988, p. 350).

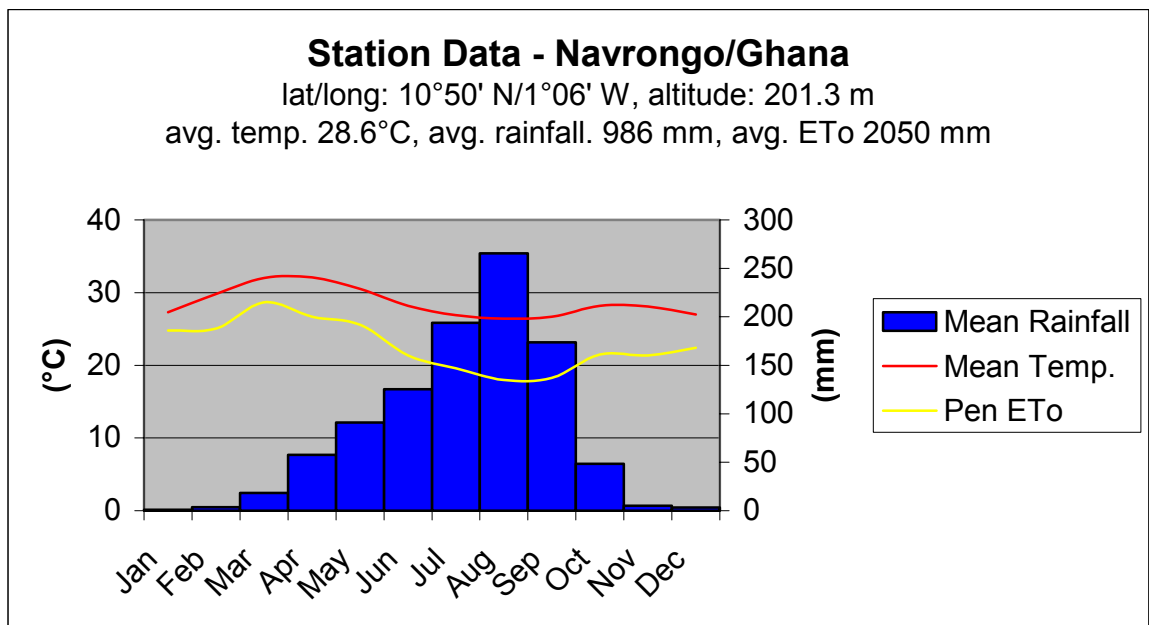


Figure 2: Climatic Data for Navrongo.

(Data source: Ghana Meteorological Services Department. In: KRANJAC-BERISALJEVIC' et al. 1998, pp. 55-56.)

The data from the meteorological station in Navrongo (Figure 2, Appendix 1) characterizes the local climatic conditions:

Temperature: With an average of 28.6°C, temperatures are consistently high. Monthly averages range from 26.4°C at the peak of the rainy season in August to a maximum of 32.1°C in April. As it is common for the tropics, diurnal temperature changes exceed monthly variations.

Rainfall: Navrongo shows a monomodal rainy season. The monthly totals increase slowly from March until they reach a peak in August or September after which there is a sharp decrease (BOATENG 1959, p. 32). The average monthly rainfall sums up to 986 mm per year. In reference to ACHEAMPONG's definition, "a month is considered 'wet' if rainfall for

that month is 102 mm or more³ and is over and above the [... potential evaporation] rate for that same month” (1988, p. 127). With only three humid months (July to September), Navrongo is clearly semi-arid.

Evaporation: Analogous to the temperature, the evaporation curve follows a similar shape. The total evaporation of 2050 mm exceeds the annual rainfall more than twofold. Besides the total, the interplay of the course of precipitation and evaporation throughout the year are of greater importance. With the sharp decrease of rainfall at the end of the rainy season in September, the evaporation rises simultaneously until it accounts for the greatest water deficit in May. Thereafter, the deficit diminishes until rainfall exceeds evaporation again in July. From the end of the rainy season onward, dry spells and drought stress gradually become more likely due to the combination of precipitations and evaporations annual cycles. Thus, for both agricultural and domestic use, the retention of water then becomes a key issue.

Type and Intensity of Rainfall and general circulation: While climate records from meteorological stations describe general climatic characteristics well, the type and intensity of rainfall cannot be determined from the averaged data. The cause of the different type of rainfall is the distribution of different air masses, and their interactions. The formation processes that generate these different rainfall types become clear when looking at the atmospheric circulation at a sub-continental or regional level.

Situated within the zone of Hadley circulation, the region is predominantly influenced by two air masses that differ considerably, namely monsoonal air masses in summer (also known as SW-monsoon) and Harmattan (or NE-trade winds) during winter in the northern hemisphere.

Figure 3a illustrates the constellation of these two air masses as they occur over West Africa. Indicated by the diagonal line is the boundary that schematically separates the Harmattan and monsoonal air masses, referred to as Intertropical front⁴. The constellation of these two air masses is not a static or localized phenomenon. As a part of the Hadley circulation, it rather shifts in accordance with the Intertropical Convergence Zone⁵ (ITCZ), where air masses converge and convect. Modified through the land-sea-constellation, the relocation of the ITCZ is induced by the yearly cycle of the sun’s zenith stand between the tropics of Capricorn and Cancer. A ground-point, as e.g. Navrongo, which is situated in the influence of the Hadley

³ ”Gregory (1965) defined the wet season as that sequence of months in which the mean rainfall is at least four inches (102 mm)“ (HAYWARD/OGUNTOYINBO 1987, p.120).

⁴ The nomenclature for this air mass boundary is disputatious. Especially the suitability of term “front” is questioned due to the minor differences between the two air masses. The World Meteorological Organization adopted the term Inter-tropical Discontinuity (ITD), which is also seen as a suboptimal description by some authors. For further discussion of the terminology, see HAYWARD/OGUNTOYINBO 1987, p. 114.

⁵ Strictly speaking, the formation of the ITCZ can only be observed over the sea. However, it is commonly used for land areas to better describe circulation models.

circulation thus falls into different weather zones⁶ (A to D) through the course of a year (Figures 3a and 3b).

The weather zones A to D are associated with different weather phenomena and different types of dominating rainfall that thereby occur in a region, which are Harmattan in zone A, thunderstorms in zone B, squall lines in zone C and monsoonal rains in zone D.

Figure 3b shows that Navrongo is under the influence of weather Zone A roughly for a four-month period from mid-November until mid of March. At that time, with the ITCZ lying on the southern hemisphere in January, West Africa is under the influence of

the northeasterly trade winds. These trade winds emerge from air masses being drawn south to compensate for the low pressure caused from heat-induced convection at the ITCZ, with the coriolis force deflecting the winds to their north-easterly direction. In West Africa, this wind is also known as *Harmattan*, a hot, dry and dust-laden wind coming from the Sahara desert.

Weather Zone B influences the Upper East Region twice for a total of roughly 3 months. Once from mid of March to mid of May and a second time from mid-October to mid of November, the region receives rainfall from tropical convectional rains. Favored by the sparsely vegetation-covered land surfaces, intense heating triggers the convection of air masses in an unstable atmosphere, which results in the formation of cumulus and cumulonimbus clouds (KAMARA 1984, pp. 50f). These discharge their humidity in the form of short-termed and localized *thunderstorms* (Appendix 2a). Situated at both ends of Zone A,

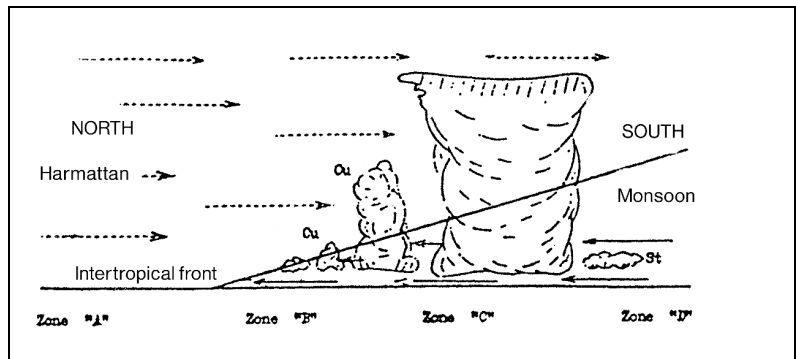


Figure 3a: Structure of the Intertropical Front over western Africa in northern summer.

The Intertropical Front separates Harmattan and monsoonal airmasses, which are related with different types of rainfall. (Source: LEROUX 2001, p. 230, after Knight and Smith. Edited.)

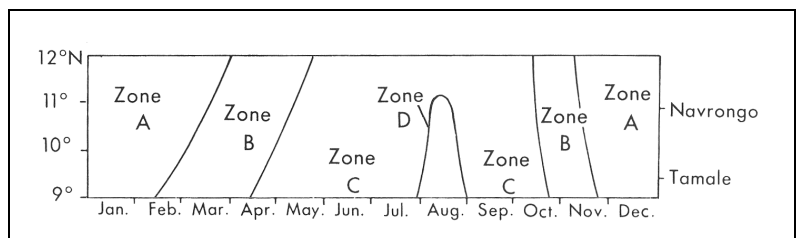


Figure 3b: Navrongo's membership to different weather zones in the course of a year.

Zone A: little clouds, low rainfall and dry air; Harmattan.
 Zone B: low rainfall but humid air; Thunderstorms.
 Zone C: rainfall in heavy showers, humid air; Squall lines.
 Zone D: cloudy/overcast, frequent, persistent rainfalls; Monsoon. (Source: WEISCHET/ENDLICHER 2000, p. 263. Edited.)

⁶ Both number and definition of the weather zones differ slightly among authors. Detailed discussions about these can be found elsewhere (HAYWARD/OGUNTOYINBO 1987, pp.114-117, LEROUX 2001, pp.229-232, WEISCHET/ENDLICHER 2000, pp. 262-269).

the two Zone B-segments may be interpreted as a lead-in into the rainy season, and a lead-out respectively.

Zone D, in anticipation, which only lasts half a month from early to late August, is associated with *monsoonal rains*. This type of rainfall is due to “large-scale convergence” (KAMARA 1984, p. 55), affecting wide areas at a time. Monsoonal rains are persistent (lasting a few hours to several days) but at low intensity (Appendix 2b). They reach the Upper East Region when the ITCZ migrates north during the north-hemispheric summer, causing the land south of it to be under the influence of air masses from the southern part of the Hadley circulation. The originally southern hemispheric southeastern trade winds then cross the equator and are deflected to southwestern monsoonal winds through the coriolis force. Having picked up a lot of humidity over the sea, the greatest rainfall occurs in proximity to the Guinea Coast. Further north and in the Upper East, monsoonal rains yield small amounts of rainfall.

Finally – and most important for northern Ghana’s precipitation yield – is Zone C, which mainly mirrors the rainy season (compare with Figure 2). The rain in this zone, which ranges from mid of May to early August, and from late August until mid-October (total ca. 4½ months), is mainly due to “*squall*

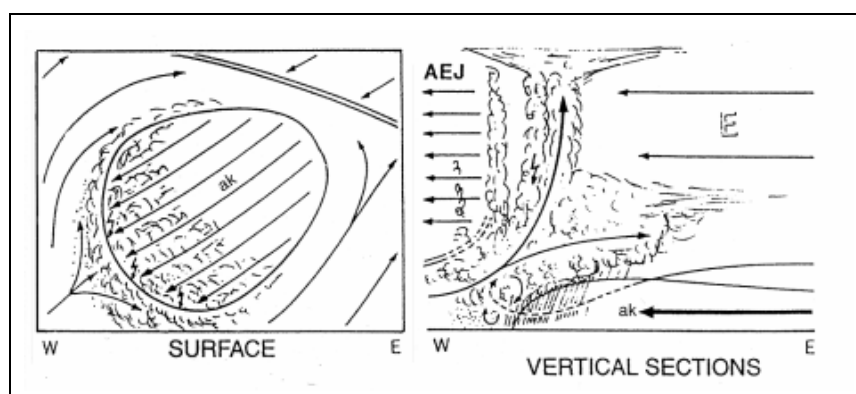


Figure 4: Surface and vertical view of a squall line.

A moving cold core (ak) intrudes under unstable monsoonal air masses and forces them to lift up. In higher altitudes, the AEJ “compresses” them to a cloud tower. Its backside is accompanied by a stratiform cloud tail.
(Source: LEROUX 2001, p.253. Edited.)

lines” (LEROUX 2001, pp. 234-265; PETERS et al. 1989). While the formation of squall lines is not yet fully understood, one theory explains its formation by an intrusion of a moving cold core (ak) under unstable monsoonal air masses (Figure 4). The disturbed humid monsoonal air mass compensates for this with uplift, whereby the African Easterly Jet (AEJ), a strong high-altitude wind in the higher troposphere, catches its upper parts. The humid air is then pushed westward by the AEJ, building up a cloud tower that is followed by a tail of stratiform clouds.

The characteristics of rainfall from squall lines differ considerably from those of monsoonal rains. Figure 5 exemplary illustrates the rainfall characteristics of the westward passage of such a typically north-south oriented squall line that passed the Upper East Region on the

09.09.2001. Depicted to the left is a radar image of the squall-line that was recorded during the Tropical Rainfall Measuring Mission (TRMM). The graph on the right hand side shows the corresponding rainfall record for Tamale (Northern Region), about 200 km south-southwest of Navrongo. The rainfall event starts with a sudden peak of high intensity and then declines again, yielding approximately 80% of this events rainfall within 45 minutes (2700 sec). The rain stems from the convection tower in the front parts of the squall line depicted in the reddish-yellowish colors on the TRMM-image (compare with Figure 4). After a period of moderate to low rainfall (30 minutes), the intensity rose slightly again due to the gentle rains from the tail of the squall line (greenish colors), and then faded again until it ended after 3 hours and 40 minutes.

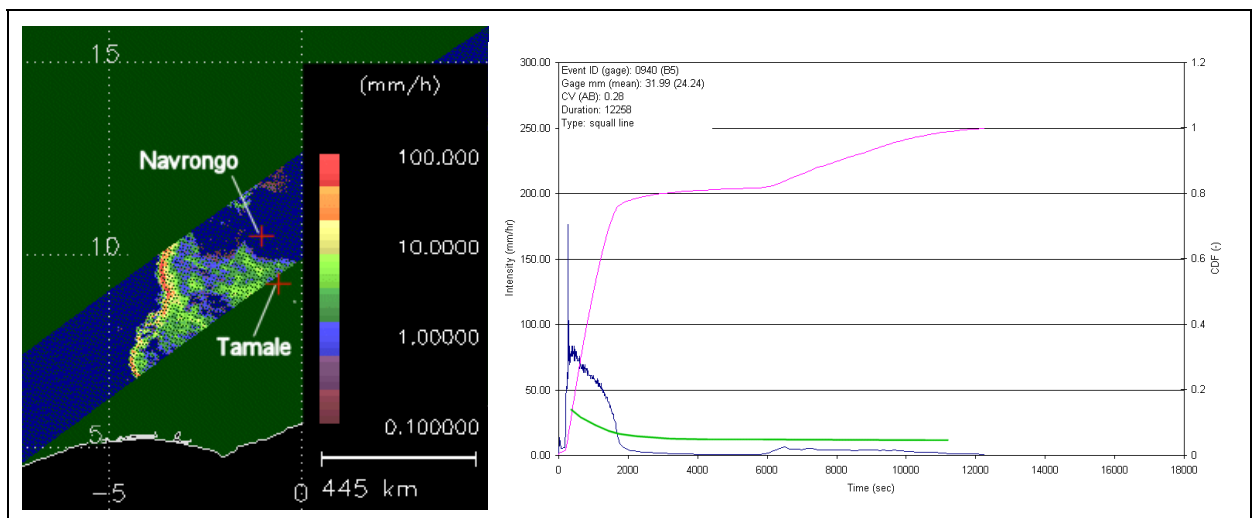


Figure 5: TRMM scene and associated rainfall of a squall line that passed Northern Ghana on the 09.09.2001.

The colors depicted in the swath of the TRMM-image are associated with different rainfall intensities. Depicted on the right-hand graph is rainfall intensity over time (blue) and its cumulative density function (CDF, pink). Where rainfall exceeds the simplified infiltration curve (green), surface runoff occurs.

The crosshairs mark the rainfall observation site Tamale (Northern Region), and Navrongo (Upper East Region). (Sources: TRMM image from GSFC DAAC (2002).

Rainfall observation from FRIESEN 2002, p. 79. Edited.

Infiltration rate curve (green) from HERRMANN 1977 referred to in SCHULTZ 1995, p. 386.)

In northern Ghana, roughly 90% of the total precipitation is due to squall lines (Figure 6) (WEISCHET/ENDLICHER 2000, p. 268). Particularly for the Upper East Region, KASEI verifies that “Bawku and Navrongo are characterized by short duration rains usually preceded by violent storms” (1988, p. 350). Figure 6 also mirrors Navrongo’s cycle through the weather zones. Within the rainy season, the month August stands out through comparably low rainfall. This can be interpreted as a result of the influence of monsoonal air masses (Zone D) for about half a month. As the yielded rainfall from monsoonal air masses is little, the main

effect is a reduction of rainfall totals through the displacement of zone C that is associated with the rains from squall lines.

The relevance of the predominant precipitation from squall lines becomes clear when taking into consideration the generalized infiltration curve (Figure 5). Whenever each rainfall event's rainfall intensities exceed the infiltration curve, the water surplus goes – on the cost of soil moisture recharge – into surface runoff. The Upper East Region is thus more “liable” to surface runoff, than regions that receive the same amount of rain from gentle monsoonal rains. The degree to which rainfall becomes runoff (rainfall-runoff-ratio) has two important meanings:

1. *It describes the amount of water that can be captured by dams which otherwise would be lost to downstream areas.*
2. *The amount of runoff accounts for the shape of valleys due to its morphological efficacy.*

Lead by the idea of improving economic and thus agricultural development in the Upper East Region, the retention of runoff in man made reservoirs can contribute to an increased and more stable agricultural production. Through water retention in reservoirs, larger amounts of Upper East's precipitation can be utilized and water availability can be extended into the dry season.

2.2.2 Vegetation and Agro-Ecological Zones

The vast part of Sub-Saharan West Africa belongs to the savanna zone, which is partitioned into sub-groups. From north to south, these are named the Sahel-, Sudan-, and Guinea- Savanna Zones (Figure 7). Adjoining to the south is the Forest Zone that stretches along the Guinea Coast Countries. It is split into two blocks by the “Togo Gap” (WINDMEIJER et al. 1994, p. 74) where the Guinea Savanna Zone reaches down to the coast, mainly owing to lower rainfall.

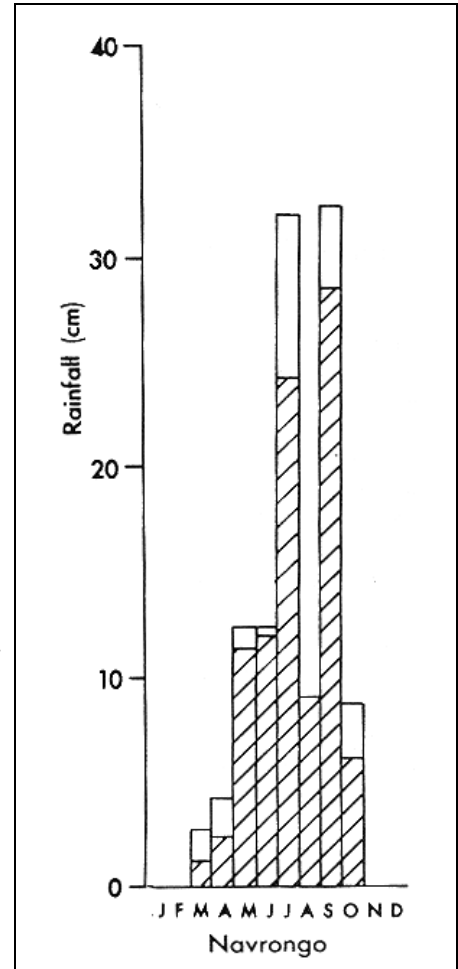


Figure 6: Monthly rainfall and the proportion of monthly rainfall due to line squalls (shaded) in 1955 in Navrongo/Ghana.

Navrongo receives roughly 90% of its rainfall from squall lines. The undefined proportions mainly compose of thunderstorms, and possibly monsoonal rains.

(Source: After ELDRIDGE 1957 referred to in HAYWARD/OGUNTOYINBO 1987, p 112. Edited.)

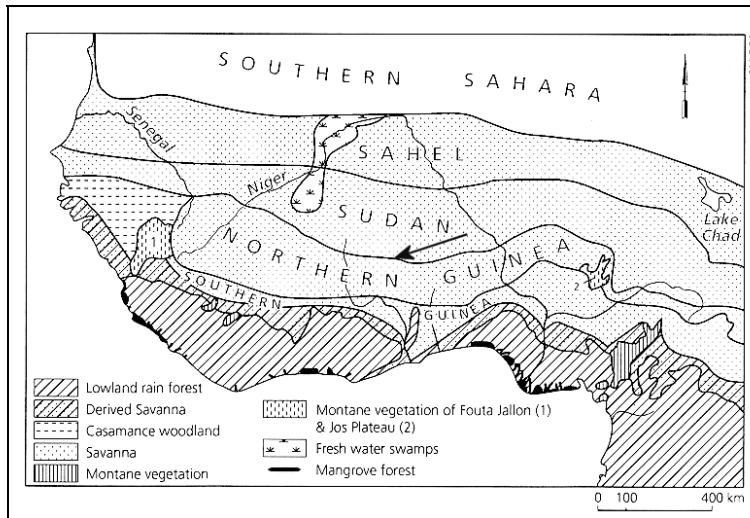


Figure 7: The vegetation zones of West Africa.

The Upper East Region lies in the fringe area between the Northern Guinea Savanna Zone and the Sudan Savanna Zone (see arrow). The boundary between these two zones fluctuates in accordance with climatic variations. (Source: WINDMEIJER/ANDRIESSE 1993, p. 73.).

The Upper East Region of Ghana is situated in the transitional area of the northern Guinea and the Sudan savanna zone. For both the northern edge of the Guinea Savanna Zone and the southern edge of the Sudan Savanna Zone, the vegetation is characterized by open woodland savannas, associated with perennial grasses in the south, and increasingly annual tussock grasses in the northern zone (BOATENG 1959, pp. 50-51; ILOEJE 1980, pp. 29-32; WINDMEIJER et al. 1993, pp. 73-78).

Similarly to the Vegetation Zones described above, West Africa can be divided into Agro-Ecological Zones. Depending on the author, the zones are solely defined by mean annual precipitation, or by the length of the growing period⁷ to represent the land's agricultural potential better. Following the termination of the vegetation zones, the extents of agro-ecological zones also only differ slightly from the vegetation zones. The Upper East's agro-ecological affiliation is the Guinea Savanna Zone, which - in its northern part - is defined by a growing period of between 165 and 210 days per year, monomodal rainfall, 900 – 1500 mm of rainfall and radiation characteristics favorable for plant growth (WINDMEIJER et al. 1993, pp. 28f).

The boundaries of these zones fluctuate within the range of climatic variations they are defined with, and thus have to be seen as zones of transition rather than clearly defined boundaries.

⁷ Definition of growth length: „A continuous period during the year when the precipitation is more than half the potential evapotranspiration ($P > 0.5 ET_p$), plus a number of days required to evaporate an assumed 100 mm of water stored in the soil after the rains have ceased. The growing season must exhibit a distinct humid period during which the precipitation is more than the potential evapotranspiration ($P > ET_p$)“ (FAO 1978, TAMS/CIEH 1976-1978, referred to in WINDMEIJER et al. 1993, p. 28, accentuation edited).

2.2.3 Geology and Relief

The Upper East Region of Ghana predominantly consists of intruded granites and Pre-Cambrian Rocks of the *Birimian* and *Tarkwaian* series. The Birimian series is older and consists of metamorphic lavas, various intrusive rocks, phyllites, schists and tuffs. The Tarkwaian, which only occurs to a very small extent, consists of quartzites, phyllites, schists and conglomerates. They both show traces of intense folding, but all the mountains which were built up due to the folding have worn down long ago, leaving only a few roots and resistant beds as upstanding masses today (BOATENG 1959, pp. 16-21).

From a topographic point of view, the Upper East Region is part of the “Savanna High Plains” (DICKSON/BENNEH 1995, pp. 11f). Most of its areas are “gently undulating, with broad, poorly drained valleys and extensive flood plains adjacent to the Volta [...] river” (KRANJAC-BERISALJEVIC’ et al. 1999, p. 9). Along parts of the Upper East’s southern boundary rises the Gambaga Scarp, which is a result of differential erosion of beds of varying hardness.

The relief also plays an important role regarding (possible) dam construction. On the one hand, dam construction necessitates a certain landscape roughness. On the other hand, homogeneous relief properties are of great importance to the feasibility and success of this exercise. As long as the surface roughness is approximately constant, the presence of area-volume relations is expected. In this context, “constant” refers to the surface undulating at a relative steady frequency and amplitude. If changes in roughness were identifiable, e.g. as they develop in areas with a significant change in geologies, splitting up the area into relatively homogeneous sub-areas is a reasonable means to (re-)achieve good area-volume correlations, if needed. This, however, is not the case in the Upper East Region.

Table 1: Relief Properties of the Upper East Region

Minimum elevation (m)	122
Maximum elevation (m)	455
Mean elevation (m)	197
Standard deviation (m)	35.33
Coefficient of variation of elevation	0.18
Average slope angle (°)	0.49
Total area (km ²)	8689.03
Total evaluated area (km ²)	8646.72
Area within ±1 St.D. from mean (km ²)	6186.65
Area within ±1 St.D. from mean (%)	71.6

Summarized in Table 1 are a number of variables used to describe the relief properties of the Upper East’s landscape. While the range between minimum and maximum elevations are – with respect to the overall appearance – relatively high, they occur localized and do not affect great areas. The flatness and uniformity of elevations is expressed in the large area of 71.6 % lying

within one standard deviation from the mean elevation. If the elevation was statistically normal distributed, 2/3rds of the area were expected within ± 1 standard deviation of the mean. Having such a large proportion of the Upper East’s area within this close range of

elevations, the low average slope angle of 0.49° is not surprising. Figure 8 shows a digital elevation model, which was created from contour lines by triangulation. Indicated by the top arrow is the highest point of Upper East Region that is located directly at the border with Burkina Faso. The elevation rises there towards the escarpment that follows the border on the Burkinese side. In opposition, the lowest points cluster along the southern edge of the Upper East Region. At the level of 122 m these are reached where the River Sisili flows out of the Upper East Region (descending arrow), and, in a second cluster, along the White Volta after it has passed the Gambaga Scarp to its south (ascending arrow).

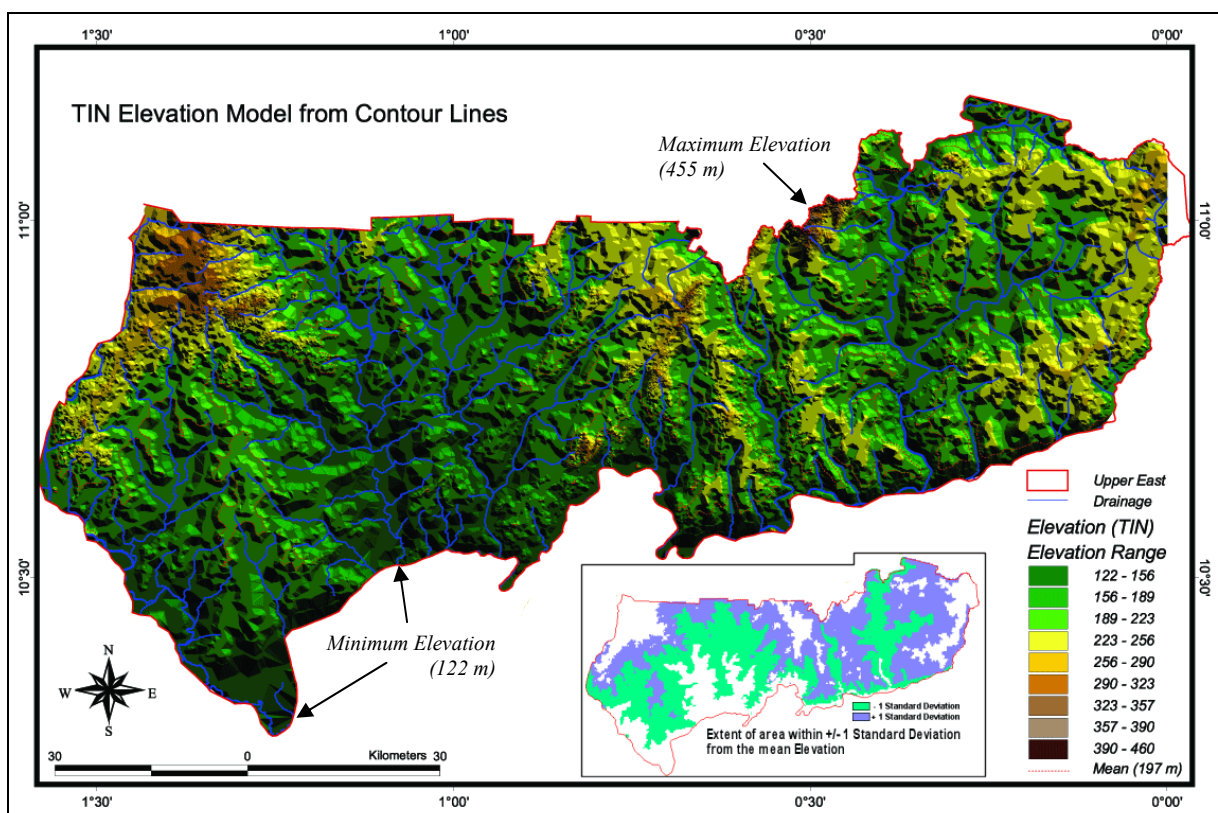


Figure 8: Elevation Model (TIN) of the Upper East.

By means of triangulation, the elevation model was created from contour lines with a vertical resolution of ≈ 15 m (50 feet). The inset graphically displays the extent and spread of plus (blue) and minus (green) one standard deviation from the mean elevation.

The large extent of the area within ± 1 standard deviation is shown by the inset.

2.2.4 Drainage Systems and Water Balance

The drainage system of the Upper East Region is a part of the White Volta sub-basin, the second largest of the Volta's four major sub-basins (see Appendix 3). The White Volta is its

largest river, which finally assimilates the runoff from all rivers that drain the Upper East Region. Its major tributaries are the Red Volta, the Sisili and the Tono River, all flowing into Ghana from Burkina Faso. The outlet from Bagré dam in Burkina Faso mainly regulates the river flow-level of the White Volta, but otherwise the variation of annual runoff is very large. Approximately 60 % of the total runoff concentrates in September and October (LEDGER 1964, p. 88).

As it is typical for regions primarily made up out of intrusive and metamorphic rock which are furthermore relatively flat, the drainage network is dendritic to subparallel (WINDMEIJER et al. 1993). Among others, a common method to hierarchically “rank” stream segments in a drainage network is the stream order classification after the “Horton-Strahler approach” (KNIGHTON 1998, p. 10). According to this, the segments of a drainage network are assigned numbers

(Figure 9). Starting from the source (stream order 1) the stream order increments by one where two stream segments of the same order form a downstream channel segment. Where two stream segments of different order flow together, the downstream channel segment inherits the number of the higher order headwater stream, but does not increment. A further characteristic in the description of drainage networks is the

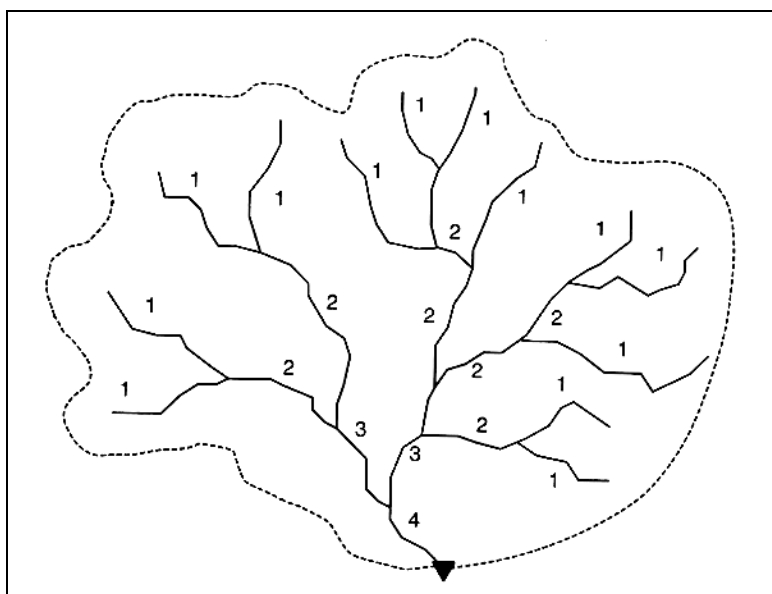


Figure 9: System of stream-ordering after Horton-Strahler.

(Source: BEVEN 2001, p. 101)

drainage density, which is defined as the sum of length of streams per km². In the Upper East Region this is low (0.3-0.6) to medium (0.6-1.2) (after WINDMEIJER et al. 1993, Annex 4).

The White Volta, Upper East’s river of the highest stream order, constitutes an asymmetric modification to the mainly dendritic network. It only takes up tributaries coming from northern directions as the Gambaga Scarp, whose cliffy side rises along the Upper East’s southern boundary and dips south, causing the area south of the White Volta to drain southward away from the Upper East Region.

Especially seen in association with the dominant role of intense rainfall through squall lines, “the [drainage] network is a reflection of the runoff-producing mechanisms of the hillslopes

operating over a long period of time, but development of the network has a feedback effect on the form of hillslopes and consequent runoff production. These geomorphologic linkages result in structural regularities in the form of catchments and it should be possible to take advantage of these regularities in making hydrological predictions” (BEVEN 2001, p. 100). Based on the uniformity of the geological basement, these findings are expected to be also transferable to the stream channel morphometry. Merging this postulate with the hierarchical stream orders, this means that a stream of low order has a small catchment area and develops a comparably moderately shaped valley. In contrast, higher order stream segments, which are related to larger catchments and thus have to take up more runoff, show a more distinct shape in the cross-section of their valleys. Both “the magnitude of discharge and the character of the flow regime” influence channel forms (HARVEY 1969 and STEVENS et al. 1975 referred to in KNIGHTON 1998, p. 151).

As the shape and volume of reservoirs depend on the shape of the stream channel beds and valleys they are constructed in, it should also be possible to take advantage of the above-described regularities in making reservoir volume predictions derived from their surface areas. The stream channels and valleys at stake, where small and medium sized reservoirs are usually located in, are so-called “inland valleys”. They are defined as “the upper reaches of river systems (inland with respect to the main rivers and main tributaries) [...] which [...] do not yet have any distinct systems of floodplains and levees” (WINDMEIJER et al 1993, p. 37). Based on Raunet’s inland valley characterization, WINDMEIJER et al. subdivide them into “stream inland valleys” and “river inland valleys” (1993, p. 37). Stream inland valleys compose of the valley head

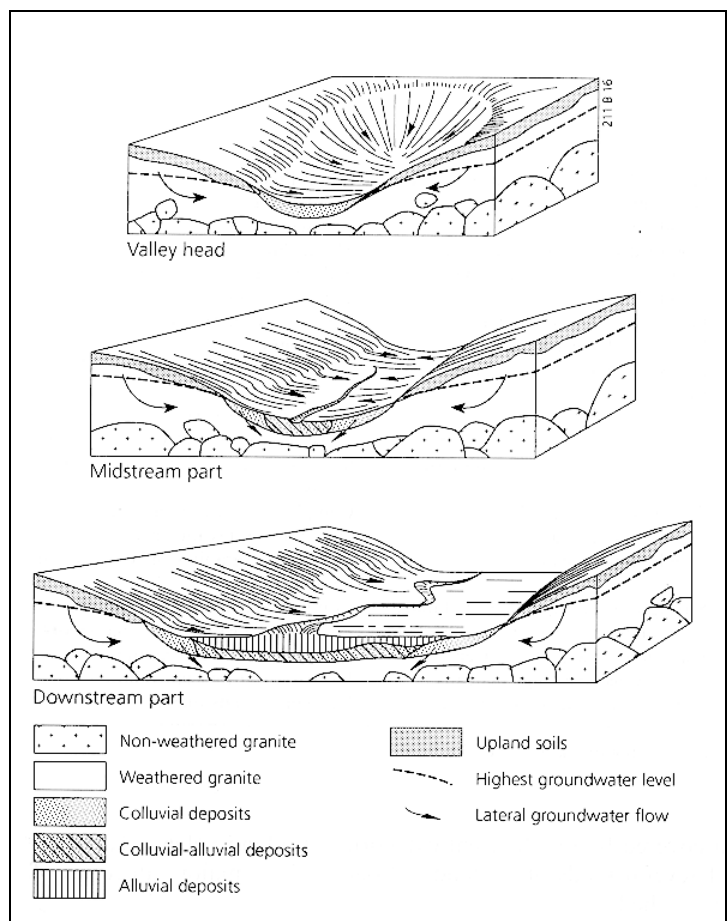


Figure 10: Valley head, midstream part and downstream part of Inland Valleys.

Valley head and midstream part are summarized by the term “stream inland valley”, whereas the downstream part is also referred to as a “river inland valley”.

(Source: After RAUNET 1985 referred to in WINDMEIJER et al. 1993, p. 39)

and the midstream part (Figure 10).

While the valley head refers to a concave indentation at the upstream section of a valley under the absence of a stream channel, the latter part does feature a stream channel in the center of its concave valley, which widens from 10 m in its upper reaches to 100 m in the lower reaches. Further downstream follow the river inland valleys, which have a wider stream channel and floodplains up to 200 m wide. In Raunet's characterization they resemble the downstream part.

Besides the general description of typical valley sequence categories

along the longitudinal extent, the cross-section profiles of valleys are of interest. Valley shapes are the result of interaction between climate, geology and geomorphology. Figure 11 shows the cross-section of two valleys as they develop on granite-gneiss in different rainfall regimes, and thus under conditions similar to those occurring in northern Ghana.

With an annual precipitation of 986 mm for Navrongo (Appendix 1), the Upper East's valleys mainly have the shapes as shown by the upper profile. However, shapes associated with higher rainfall as the lower cross-section in Figure 11 are also present in the Upper East Region. This might be the consequence of the previously described liability to runoff upon torrential rainfalls (high rainfall-runoff coefficient). Summarizing the above it becomes clear that the whereabouts of reservoir locations along a stream determine the morphometry of their basins.

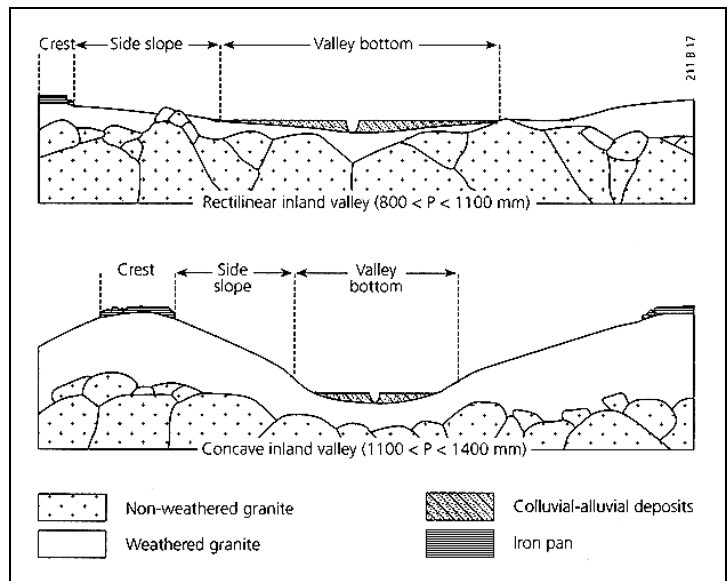


Figure 11: Valley cross-sections.

Cross sections of inland valleys in West Africa, developed in granite-gneiss in different rainfall regimes.

(Source: After RAUNET 1985 referred to in WINDMEIJER et al. 1993, p. 43. Edited.)

Water balance: For agricultural production, soil moisture is of great importance. ACHEAMPONG (1988) deducts water budgets from potential evaporation and rainfall data and shows via a simple water balance study that the surplus of water of the first two wet months mainly goes into soil moisture recharge. As it reaches a saturation threshold value (102 mm), most of the precipitated water is disposed of as runoff. In Navrongo, soils are thus at field capacity from August to September (Figure 12). From late October onward, the soil moisture deficit begins to build up as precipitation falls below the potential evaporation and lasts until June-July when precipitation rises above potential evaporation again. This poses a major restriction to agricultural production.

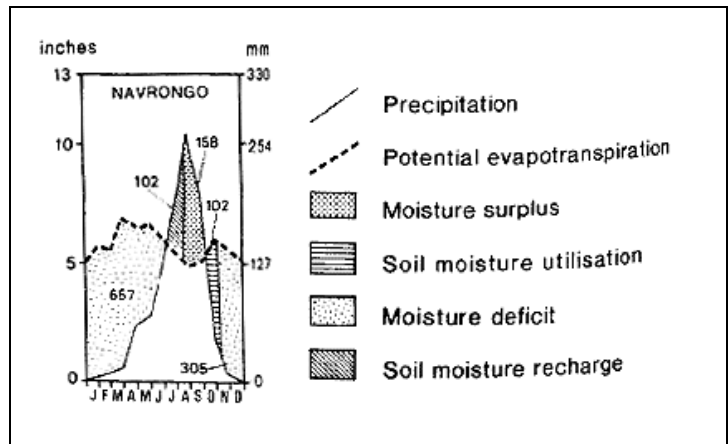


Figure 12: Water Budget for Navrongo.

The longest period of the year, Navrongo is characterized by a moisture deficit (Nov. to Jun/Jul). From June/July to mid August, precipitation exceeds potential evaporation. Its excess goes into soil moisture recharge. Then, the moisture surplus goes into runoff, and as the precipitation falls below the potential evaporation, the soil moisture deficit begins to build up again. (Source: ACHEAMPONG 1988, p. 128. Edited.)

2.3 General Properties of Reservoirs

Especially in semi-arid environments such as the area studied, the presence and extent of surface water bodies shows considerable seasonal and inter-annual variability. Reservoirs capture the artificially dammed surface runoff from ephemeral and intermittent streams that occur in terms of a direct or prolonged response to rainfall.

Small and medium sized reservoirs usually have one or two inflows and are located in the above described stream and river inland valleys, provided the undulating landscape makes enough difference in elevation to facilitate the construction of a dam. In general, these are earth dams with a clay core, and, ideally with a rock riprap for the prevention of dam wall erosion. The presence, dimension and quality of a spillway are of utmost importance for the dam's durability. Often, rainfall in the tropics occurs localized but can be torrential, causing runoff in terms of sheet floods as the amount of rainfall exceeds infiltration rates. When the inflow of runoff water exceeds the storage capacity of a reservoir, spillways allow excess water from the peak flows to drain out of the reservoir in a controlled way. The design of spillways and dam heights is normally based on design floods, the maximum probable floods

that are expected to occur at certain return periods. A “maximum probable flood” is defined as “the greatest flood that may reasonably be expected, taking into account all pertinent conditions of location, meteorology, hydrology and terrain” (CHOW 1968, p. 25 – 72). The use of consistent design floods in the history of dam development in the Upper East Region, however, can be doubted. Yet, they define the maximum capacity of a reservoir and prevent inflowing water masses from overflowing and thereby damaging the dam wall.

Maximum volumes can, in turn, be seen in two ways, namely in terms of a “relative maximum” which is defined by the highest level reached in a given year, and secondly in terms of an “absolute maximum” which is defined by the height of the spillway.

Starting from the point of relative maximum volume, which is expected to be reached at the end of the rainy season, the volumes of reservoirs begin to decrease again due to water use and losses.

As summarized below, the influences on the area and volume of reservoirs are:

1. *inter-annual rainfall variability which accounts for a relative maximum of water levels*
2. *dam height and height of spillway which define the absolute maxima of water levels*
3. *time of the year/season (intra-annual variations)*
4. *withdrawal (irrigation and gardening, cattle, households, building, etc.)*
5. *storage reduction through evaporation, seepage and percolation*
6. *age of the dam (siltation)*

The degree to which these variations in area and volume occur can vary considerably. Reservoirs can even dry up completely due to high draft for irrigation, and sometimes even just through evaporation. As, over time, small reservoirs are relatively variable surface features, it is obvious that the timing of satellite imagery to be used for their detection has a great influence on the classification result.

This study aims to derive the storage volumes of reservoirs as a function of their areas. As it is more accurate to know the maximum volume of a reservoir and then downscale it to the various lower water levels than contrariwise, the image selection should rest upon the assumption that

reservoir surface areas are greatest at the end of the rainy season and then start to decline.

Postulating that the occurrence of reservoirs and their characteristics are strongly dependant on the morphology and their location within a drainage network, a general expectation of size-dependant frequency distribution of reservoirs is thus:

The lower in the hierarchy of a drainage network dam sites are located at, the smaller they are in area and volume, and the larger is their occurrence in number, and vice-versa.

Reservoirs are built for different reasons. In contrast to stream regulation or flood control, the reservoirs in the Upper East Region capture and conserve runoff for later agricultural and domestic use. Small and medium sized reservoirs normally are multipurpose reservoirs (irrigation and gardening, fishing, building, household), but often with a dominant use pattern.

The following chapter explains the materials and methods used to acquire and evaluate man-made reservoirs throughout the Upper East Region.

Chapter 3

Materials and Methods

3.1 Evaporation from surface water bodies

The evaporation of water is a process whose scientific exploration can be traced back to the late seventeenth century (MONTEITH 1981, pp. 1-2). It describes the “emission of water vapor by a free surface [, or in other words, the transformation from the liquid to the gaseous state of aggregation] at a temperature below the boiling point” (WMO 1974, p. 75). In contrast to evapotranspiration, which also takes into consideration the influence of transpiration of vegetation, the aim of this study is the assessment of evaporation losses from man made reservoirs only. The evaporated water masses that turn into water vapor finally enter the atmospheric circulation. They represent unproductive water losses in contrast to productively used amounts of water in agricultural practices or storage reduction through seepage and percolation, which might be available further downstream again and recharge the groundwater.

The term evaporation furthermore subdivides into actual evaporation (E_a) and potential evaporation (E_p). Their difference becomes clear when considering the two basic units that determine the amount of water to evaporate. These are water availability, and the absorbing capacity of the atmosphere defined by its water vapor deficit. Actual evaporation takes into account that, with the same absorbing capacity of the atmosphere, evaporation from drier surfaces is fewer than that from wet surfaces. In other words, E_a takes into account the limitations to evaporation due to restrictions on the supply-side. It determines the various degrees of evaporation from different land covers. Potential evaporation (E_p), in contrast, refers to the “quantity of water vapor which could be emitted by a surface of ‘pure’ water, per unit surface area and unit time, under the existing atmospheric conditions” (WMO 1974, referred to

in LHOMME 1997, p. 258)⁸. It occurs, when there are no restrictions on the supply-side and the only limiting factor is the available energy-budgeted on the demand-side. From saturated surfaces like that of man-made reservoirs, the actual evaporation E_a is equivalent to the potential evaporation E_p .

For the estimation of potential evaporation from free-water surfaces, various different approaches are available⁹. Empiric-statistical methods such as the aerodynamic, or Dalton-method explain evaporation as the vertical transport of water vapor by means of vapor pressure gradients and transport coefficients, taking into account wind speed, relative humidity and the temperature at the water surface (DVWK 1996, pp. 23-25). A further kind of methods is based on energy budgets. These methods make use of the radiative balance of the open surface water. They are based on net shortwave irradiation and effective radiation calculations (DVWK 1996, pp. 25-29). In literature, we often find a reference evaporation E_o , which is the potential evaporation of a reference surface that usually is well-watered grass. To calculate potential evaporation (E_p) for other surfaces types, empirical factors are available that can be made use of.

Penman (1948) combined the aerodynamic and energy budget model into a physically based, semi-empiric combination model, which calculates potential evaporation solely from parameterized climatological data. Penman's commonly used equation for potential evaporation calculation from a free water surface is:

$$\lambda E_p = \frac{\Delta}{\Delta + \gamma} Q_n + \lambda \frac{\gamma}{\Delta + \gamma} E_a \quad (1)$$

where “ λ is the latent heat of vaporization, Δ is the slope of the saturated vapor pressure curve at air temperature, γ is the psychrometric constant, and Q_n is the net available energy at the surface” (HOBBINS et al. 2001, p. 1390). E_a represents the “drying power of air” which is composed of the vapor pressure deficit and a “wind function” (BAUMGARTNER 1996, pp. 357-362; HOBBINS et al. 2001, p. 1390).

For the purpose of this exercise, it suffices to use E_p as defined by HOBBINS et al. (2001). Based upon the above described, OGUNTUNDE (in progress) derived monthly potential evaporation for West Africa with data from the “CRU¹⁰ 0.5 Degree 1901-1995 Monthly Climate Time-Series” (NEW et al. 1999; NEW et al. 2000; CRU). This dataset consists of seven climate

⁸ An extensive discussion on definitions of the term “potential evaporation” can be found in LHOMME 1997.

⁹ Four major approaches are pursued, which can be summarized under the umbrella terms “empirical methods”, “water-balance methods”, “energy-balance methods” and “mass-transfer methods” (see VEIHMEYER 1964, pp. 11-3 – 11-14). Within these four main categories, large numbers of modified equations exist that seek to estimate evaporation adequately under different conditions and with different data requirements.

¹⁰ Climate Research Unit

elements¹¹, of which mean temperature, diurnal temperature range, wet day frequency, vapor pressure and cloud cover were used in the derivation of E_p (see Appendix 4 for a technical summary). As the focus is put on the estimation of average losses, the evaporation data from 1985-1995 was aggregated to ten-year averages of monthly E_p . The resulting decadal monthly averages of potential evaporation (mm/day) are later used to calculate and assess evaporative water losses from Upper East’s reservoirs.

3.2 The Landsat 7 ETM+ System and Remote Sensing of Surface Water Bodies

3.2.1 Characteristics of Landsat 7 ETM+ - a brief overview

Landsat 7 was launched in April 1999 and is currently the latest platform of the Landsat program¹² that started in 1972. It carries the “Enhanced Thematic Mapper Plus” (ETM+) sensor, a passive, optical across-track-scanner, which records the reflected portion of the electromagnetic radiation, and the earth’s emitted radiation in the thermal band, respectively. With an inclination to the equator of 98.2° and an equatorial crossing time at 10:00am +/- 15 min

Table 2: Spectral and Spatial Resolution of the Landsat 7 ETM+ Sensor

Band	Sensitivity (µm)	Spatial Resolution (m)
1	0.45-0.52	30
2	0.52-0.60	30
3	0.63-0.69	30
4	0.76-0.90	30
5	1.55-1.75	30
6 (thermal)	10.4-12.5	60
7	2.08-2.35	30
8 (panchromatic)	0.50-0.90	15

(Adapted from: LILLESAND/KIEFER 2000, p. 379)

(descending node), Landsat 7 belongs to the near-polar, sun-synchronous orbiters. Orbiting at an altitude of 705km, it has a period of revolution of 99 minutes and repeatedly covers an area every 16 days (LANDSAT 7 SCIENCE DATA USERS HANDBOOK).

The spectral and spatial resolutions of Landsat 7 are denoted in Table 2. For the benefit of a continuous comparable dataset, the sensitivities – or bandwidths – of the bands one through seven abut on those of ETM+’s predecessor Thematic Mapper (TM), which was mounted on Landsat 4 and 5. While the resolution of the visible and infrared bands remained unchanged at 30 m, the resolution of the thermal band six was increased from 120 to 60 m. Additionally, a panchromatic eighth band with a resolution of 15 m was introduced to the ETM+ sensor.

¹¹ The seven climate elements of the CRU 0.5° 1901-1995 Monthly Climate Time Series are discussed in (NEW et al. 2000). These are precipitation, mean temperature, diurnal temperature range, wet day frequency, vapor pressure, cloud cover and ground frost frequency.

¹² An extensive description of the Landsat program can be found in LILLESAND/KIEFER 2000, pp. 373-416.

The approximate dimension of a Landsat scene is 183 x 170 kilometers (EROS DATA CENTER). Indexed with path and row numbers according to the Worldwide Reference System (WRS), the scenes and thus the areas they cover are uniquely identifiable. The full coverage of the Upper East Region of Ghana requires four Landsat Scenes (Appendix 5).

The vast part is covered by the image strip consisting of the rows 052 and 053 in path 194, while, taking into account the overlap between neighboring paths, only a small fragment in the very western part is solely covered by the respective scenes in path 195. The scenes mainly used in this study were captured on the 7th November 1999 (194/052 and 194/053). An image captured on the 13th October 1999 (195/052), and a last one that was acquired on the 2nd February 2000 (195/053) laterally supplemented them. Their scene parameters are documented in Appendix 6.

3.2.2 Influence of date selection on classification results

In order to determine the maximum dimensions of reservoirs by means of remotely sensed data, which are represented by their largest area extent, the time of acquisition should be as close as possible to the end of the rainy season, when reservoirs are filled to their maximum capacity, and losses (draft, seepage, evaporation) are still negligible.

A look at Figure 2 showing the climatology of Navrongo reveals the end of the rainy season to be in September/October. Cloud coverage of up to 100% during the rainy season make optical remote sensing of ground features impossible. With the rains subsiding from October to November and a decline in cloud cover, the month of November turns out to meet the specified demands best. Another constraint for remote sensing, however, then arises through the emergence of the Harmattan, the dust laden NE wind, which causes considerable atmospheric scattering and reduces the contrast in the satellite images.

Having found the month of November to be most suitable with respect to seasonal variability, the year 1999 proves to have been a wet year (Figure 13, compare with Figure 2 and Appendix 7). It can thus be expected that the reservoirs absolute maximum storage volumes were reached in that year. Hence, the Landsat imagery from the 7th November 1999 is expected to optimally show the greatest extent of surface waters, both in number and area. With respect to the difficult atmospheric conditions, it has to be mentioned that the availability of useful satellite imagery is very limited. The good quality of the image strip from the 7th November that covers the greatest part of the Upper East Region is a fortunate incidence. The scenes from the 13th October 1999 and, especially, from the 2nd February 2000 are suboptimal, nonetheless they were used in that they only cover a small edge in the very west of the Upper East Region.

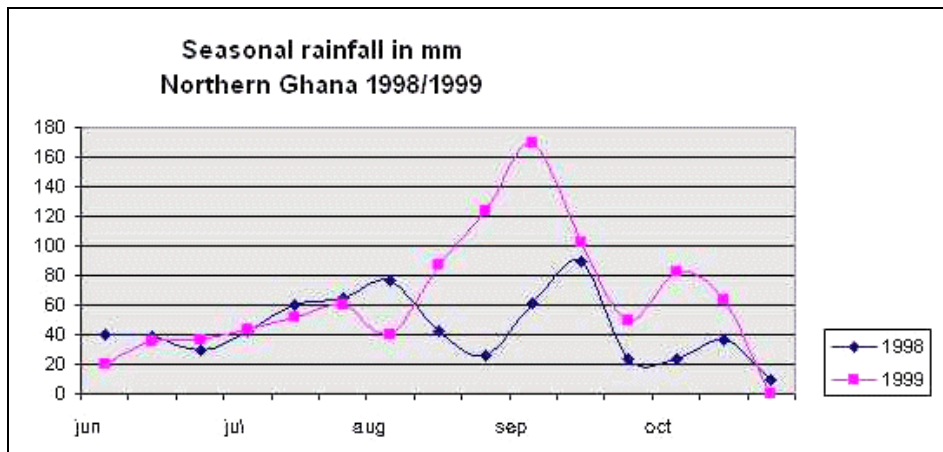


Figure 13: Seasonal Rainfall in Northern Ghana for 1998 and 1999 (in mm).
(Source: LUPO/REGINSTER 2000)

A second important date is the time of the field survey. This will be addressed together with the description of the fieldwork later in Chapter 5.1.1.

3.2.3 Water Body Detection with LANDSAT ETM+ and the reflectance properties of surface water bodies

The detection of water bodies is a concern that has been pursued since the first LANDSAT images became available in 1972. Since then, a large number of studies regarding the techniques of water detection and their quality have been published. The techniques range from visual interpretation by density slicing methods and band-ratio-approaches (NDWI¹³) to different supervised and unsupervised classification methods.

Using optical systems like LANDSAT, the detection and delineation of open surface water bodies is best done with imagery from the infrared and visible part of the spectrum. “The characteristic spectral reflectance curve for water shows a general reduction in reflectance with increasing wavelength, so that in the near-infrared the reflectance of deep, clear water is virtually zero” (MATHER 1999, p. 22). The reflectances of soils and, especially healthy vegetation are higher in these spectral bands, and therefore stand in distinct contrast to water bodies. The visible bands (VIS) enhance the contrast between water and soils (compare Figure 14).

¹³ Normalized Difference Water Index (GAO 1996, McFEETERS 1996, VONDER/CLEVERS 1998)

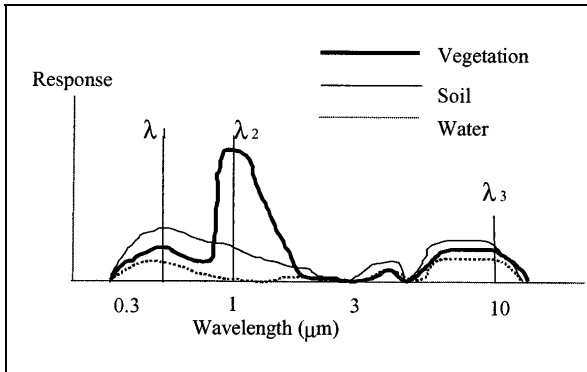


Figure 14: Reflectance vs. Wavelength for soil, vegetation and water.
(Source: KITE/PIETRONIRO 2000, p.218.)

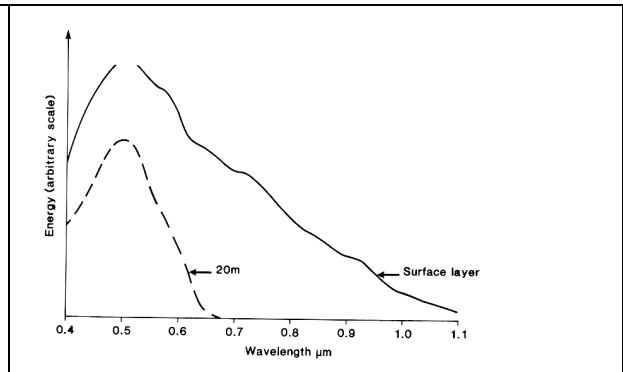


Figure 15: Spectral reflectance curve for surface water layer (solid line) and 20m (dashed).
(Source: MATHER 1999, p.24.)

This very general description of the surface water reflectance pattern, however, does not embrace the full spectrum of the diversity of surface waters as they appear in nature. Open “surface water”¹⁴ in terms of a land cover type can have a wide range of different reflectance patterns and should hence be seen as an umbrella term for various sub-classes. The spectral reflectance patterns from surface waters are composed of three influencing parameters¹⁵: Surface reflection, volume reflectance and bottom reflectance [Figure 16], meaning that “it is affected by the presence and concentration of dissolved and suspended organic and inorganic material, and by the depth of the water body [Figure 15]” (MATHER 1999, p.22).

The *surface reflection* is influenced by the sun-sensor-constellation and the roughness of the water surface created by wind. Under calm conditions, the reflection might be specular, while surface waves and certain sun-to-sensor constellation cause sunglint (MATHER 1999, p. 22). “Because of strong absorption in the middle infrared, the magnitude of the scattered component is

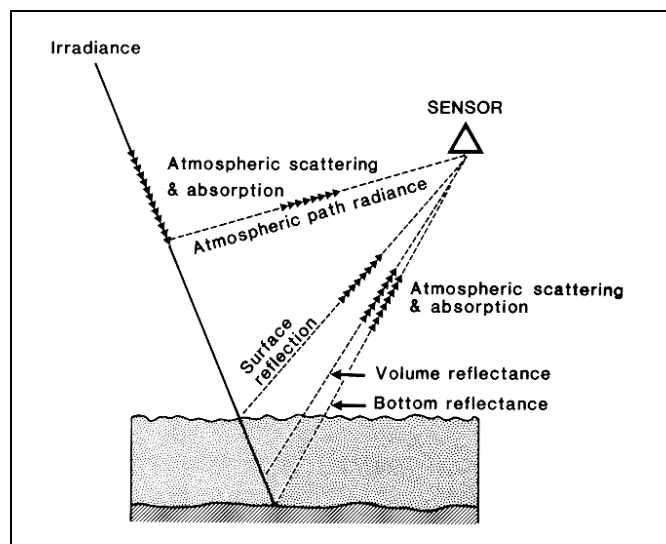


Figure 16: Processes acting on solar radiant energy in the visible part of the spectrum over an area of shallow water.
(Source: MATHER 1999, p. 24.)

¹⁴ Refers to liquid water. Snow and ice add further reflectance patterns.

¹⁵ An extensive description of influencing parameters on water return signals in optical remote sensing can be found in KONDRATYEV/FILATOV (1999, pp. 169-268).

chiefly derived from the shorter wavelengths, particularly those in the visible range” (MEIJERINK et al. 1994, p.64). Standing and floating vegetation alters the reflectance properties of a water body by adding a “red edge” (MATHER 1999, p. 20) to the return signal, the steep ascent in reflectance from the visible to the infrared part of the spectrum, which is characteristic for healthy vegetation (Figure 14).

The *volume reflection* influences the signal due to turbidity, dissolved matter, the trophic status and algae content of the reservoir water. Yet, the degree to which the volume reflection contributes to the total reflection signal of a water body depends on the penetration depth of light, which varies with the wavelengths (Figure 15). “The depth to which light can penetrate depends on the wavelength, about 10 m in the 0.5-0.6 μm waveband and less than 10 cm in the 0.8–1.1 μm range” (MEIJERINK et al. 1994, p. 64).

In shallow water bodies, *bottom reflection* occurs as a third influencing component. Similar to the volume reflection, the major influence of bottom reflection comes from the shorter wavelengths, as their penetration depth is greater than that of the higher wavelengths. Because bottom materials and the suspension freight often constitute of the same material, their influence on the reflectance can hardly be distinguished. “Therefore, it is difficult to use the penetration properties for the determination of water depths [...]” (MEIJERINK et al. 1994, p.65).

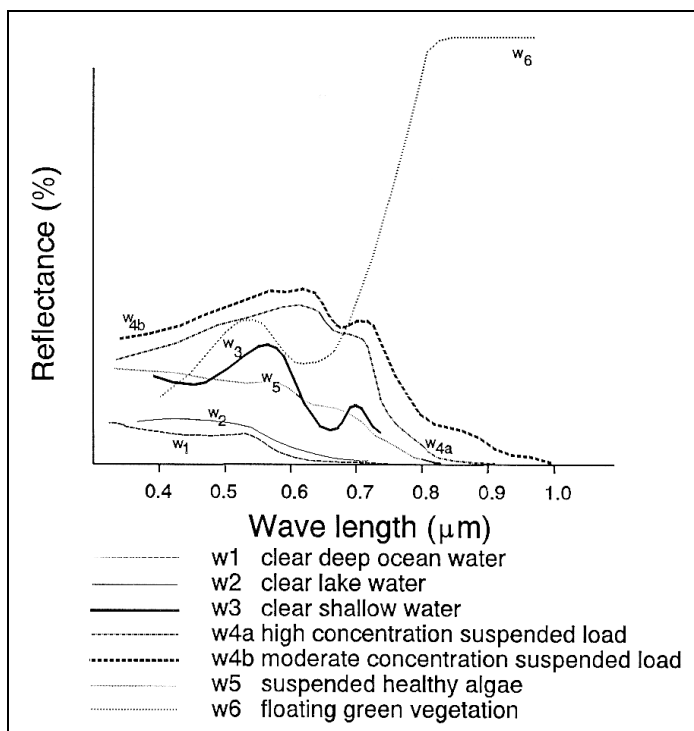


Figure 17: Possible reflectance curves of water bodies (relative reflectances).

(Source: MEIJERINK et al. 1994, p. 64.)

Resuming the influencing factors on the return signal from open water bodies, the following conclusions can be drawn:

1. *Surface water bodies can have a wide range of different reflectance patterns (Figure 17)*
2. *Water body delineation using RS data is best done with IR but also VIS bands*
3. *Bathymetry is difficult due to penetration properties of light and the often found uniformity of suspended and bottom materials*

3.2.4 Pre-Processing, classification and data extraction

The classification of the Landsat ETM+ scenes based on the above-mentioned principles and previous experience with the classification of water bodies in this area. The images 194-052 and 194-053 were geo-registered and, after pixel resizing to 30x30 m, merged into one image strip as they were recorded on the same orbit. Likewise, the images 195-052 and 195-053 were both geo-registered to each other and to the image strip 194, but not merged due to different surface water characteristics and extents, phenological states and atmospheric conditions.

Due to the lack of meteorological data on the constitution of the atmosphere at the times of acquisition, complex atmospheric corrections are hardly possible. Instead, a simple but effective atmospheric correction algorithm, the COST-Model (CHAVEZ 1996; 1989), was then applied to the scenes. It expands the dark object subtraction (DOS) method (JENSEN 1996, pp. 116-122; MEIJERINK et al. 1994, pp. 66-67; CHAVEZ 1996), which corrects the additive scattering effect and is used for the reduction of haze effects. The COST method additionally corrects for multiplicative transmittance effects of absorption by atmospheric gases and Rayleigh scattering (LILLESAND/KIEFER 1999, pp. 9f, MATHER 1999, pp. 16-17) by using the cosine of the solar zenith angle. “The corrections generated by the entirely image-based COST model are as accurate as those generated by the models that used in-situ atmospheric field measurements [...]” (CHAVEZ 1996, p. 1025, accentuation changed).

After creating false color composites with the channel combination RGB 453, the classification of reservoirs was performed using a maximum likelihood classifier. Using the channel combination RGB 453, water bodies are depicted in colors ranging from bright blue to almost black. In order to recognize reservoirs on a satellite image, the human mind makes use of several visual characteristics, such as shape, contiguity and the association with the drainage network. Image processing software, such as IDRISI, operates differently. It recognizes reservoirs as it makes use of their spectral reflectance patterns. Therefore, the image classifier needs to be “trained” with spectral information, which comes from reservoirs that were identified by visual interpretation. Lead by the approach of thematic extraction of these surface water bodies, the classifier was trained with various water sub-classes to make use of all the facets of the ‘land cover category’ water. Large numbers of training sets were therefore defined for different water classes by on-screen digitizing based on visual differences in tone. These different shades are associated with the manifold compositions and combination of the influencing factors and by this means take into account different depths as well as different algae contents and turbidity.

A clear benefit of using several sub-classes instead of one water class is that of achieving spectrally more compact classes (Figure 18). Taking into account the functioning of the maximum likelihood classifier, the advantage of this procedure becomes clearer. Whether or not a pixel is assigned to one class or the other is herein based on equi-probability contours around the statistical averages of each class, which normally show elliptical shapes, whereby each class's statistical average is calculated from its spectral training set (Figure 19). Furthermore, a threshold applied to the distance, defines the number of pixels that remain unclassified (MEIJERINK et al. 1994, pp. 91-92; MATHER 1999, pp. 181-185).

In addition to the water classes, 'dump-classes' were introduced into the classification, which are primarily not of interest, but improve the classification results significantly. As it was done for the different water sub-classes, the classifier was thus also trained with the spectral patterns of burned¹⁶ areas and parts of cloud shadows. These have a spectral overlap with what we summarize under the umbrella term "water", and lead to misclassifications. In combination with the various but compact water sub-classes, it is then possible to separate these different features. A pixel that represents a burnt surface is then assigned to the category "burnt" due to the shorter equi-probability distance to the mean of this class, rather than to a water class that is also close and would have

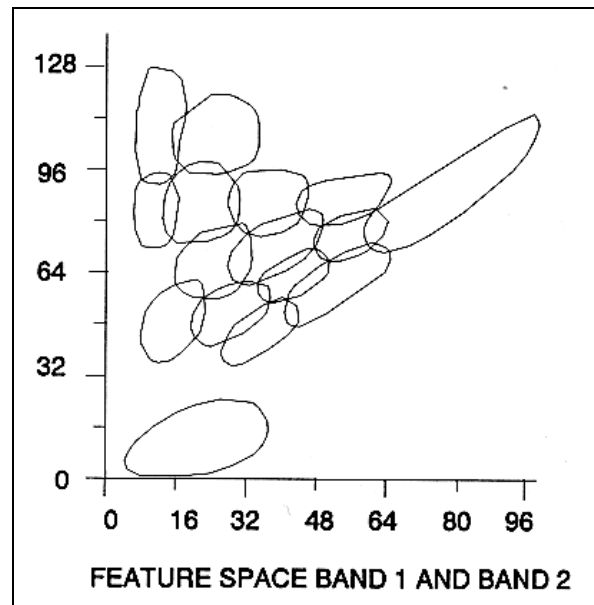


Figure 18: Arrangement of compact sub-classes in the Feature Space.

Exemplary arrangement of a large number of compact sub-classes in the feature space of band 1 plotted against band 2.

(Source: MEIJERINK et al. 1994, p. 64.)

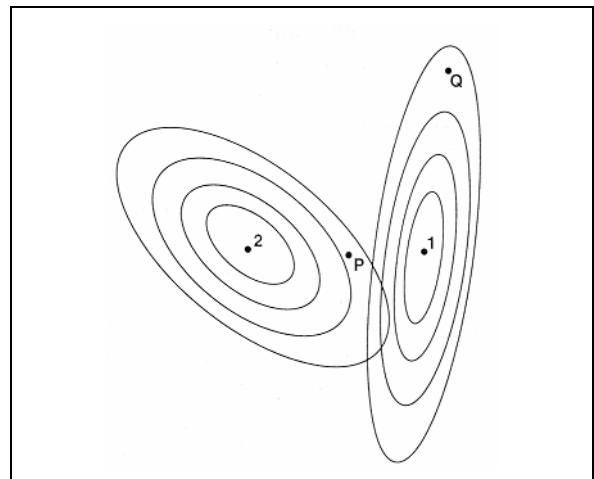


Figure 19: Equi-probability contours as used in Maximum Likelihood classification

The depicted ellipses represent equal probability contours around the classes 1 and 2. Point P, which is closer to the center of class 1, is assigned to class 2 due to the higher probability of its affiliation to class 2. Q is a member of class 1.

(Source: MATHER 1999, p. 181.)

¹⁶ A different approach to map burned land is described by (KOUTSIAS/KARTERIS/CHUVIECO 2000). They distinguish burned areas upon color space transformation (IHS). Their method was tested on a subset of the Upper East's Landsat images, which also worked well, but finally the above-described approach was chosen.

taken-up that pixel if there was no “burnt” category introduced in the classification.

The difficulties arising from the spectral overlap between water and burned areas become much clearer in the comparison of the two Landsat scenes depicted in Appendix 8 that indicate the degree to which a landscape can be affected by bushfires. In the already familiar image from the 7th November 1999, reservoirs can easily be identified, such as the two large reservoirs Tono and Vea (see also Figure 1), but also the small dark spots in the bright patches that are less vegetated due to higher population density. Mainly at the edge of these bright patches, but also in the vegetated areas (green shades) there are less contiguous dark spots that represent burnt surfaces. The second image that was recorded only one month later (9th December 1999) shows a dramatic increase in the extent of burnt areas. As it is more difficult for the human eye to spot reservoirs in this image, also the classifier underperforms when not including the above described “dump classes”. At a much lower level, the same accounts for the 7th November image.

After the classification was completed and the “dump classes” were discarded, a Boolean water image was created by regrouping the water sub-classes into one class. It was then filtered with a 3x3 median filter (JENSEN 1996, pp. 156-157; MATHER 1999, pp. 152-153) which both removes single pixels and fills ‘single-pixel-holes’ in reservoirs. Finally, based on visual interpretation, ‘misclassified’ river and riverbed pixels, oxbow lakes and the very few remaining burnt spots and cloud shadows were manually deleted.

The resulting reservoir maps were then mosaiked and georeferenced (quadratic mode) using 27 reference points derived from 1:50,000 maps that were available in digital format. The reference points were intersections, bridges and river mouths, however it was difficult to find large numbers of adequate reference points well spread throughout the image. Many times, intersections are the only points that qualify for geo-registration, but they are often located in a village or cluster of houses which appear as bright spots on the satellite image. This problem is explained by the blending of the dust roads with their mostly sparsely vegetated, bare or urban surroundings. Particularly in rural areas, houses are often built out of similar materials that lie bare in the surroundings. The same accounts for roads. Also at intersections outside villages, this problem occurs when they are surrounded by bare surfaces¹⁷. By also reverting to more variable features, such as river mouths, and bridges intersecting with rivers, lower accuracy was taken into account, resulting in an RMS of 30.17. An effect of combining the scenes of path 195 with the image strip of path 194 is best observed with the map depicted in Appendix 5. Among other things, it shows the Landsat ETM coverage of the Upper East Region and the point distribution of the classified reservoirs. Those parts of the Upper East Region that are solely covered by the

¹⁷ Bare ground at intersections is a result of behavior of pedestrians and cattle. They do not walk to the center of the intersection to turn but take shortcuts as they approach the intersection and thereby tread down vegetation. Rectangular crossroads thus often shows roughly diamond shaped bare areas.

images of path 195, turned out to contribute no additional reservoir surfaces¹⁸. Only in the overlap with the image strip of path 194, reservoirs were classified. As the image strip of path 194 from the 7th November 1999 represents larger surface extents than the scenes that were acquired later in the season (scene 195/052 from the 13th October 1999 and scene 195/053 from the 2nd February 2000), their classification results were overlain by the larger ones from the 7th November image strip. Therefore, further references to the results of the satellite image classification refer to the image strip of path 194 (rows 052 and 053) from the 7th November 1999.

For the data extraction, the Upper East Region was masked with a Boolean image of its extent, leaving only the data that correspond to this region. The contiguous water pixels were grouped to clusters that resemble reservoirs, and given unique identifiers, upon which the area calculation was performed and each reservoir could be associated with its surface area. For later use in ArcView, a raster-to-vector conversion of the reservoirs was performed.

With the previously described technique, a total of 504 reservoirs was mapped adding up to a total acreage of 3,408 ha. Reservoirs classified with an area of less than 1 ha were deleted. Also, the two largest reservoirs, Tono (1,894 ha) and Vea (435 ha), were omitted in the study. Thereafter, a total of 154 reservoirs was left, summing up to an acreage of 999.54 ha with reservoirs that range from 1 to 35 ha in size. The 348 discarded reservoirs smaller than 1 ha only account for 80 ha of surface areas. Their hydrological impact is minimal and the classification uncertainty is getting high for such small features as each pixel is already 0.09 ha.

The selection of sites to visit was based on the evaluation of the data regarding the distribution of reservoir surface areas in the Upper East Region. No significant breaks were found (Figure 20), however it was not clear whether splitting the data in categories was necessary in further steps. For the benefit of a good distribution of samples over the full range of the different reservoir sizes, the dataset was split into three approximately equal categories. Category 1 consists of 51 reservoirs and ranges from 1 to 2.79 ha. Category 2 is the largest comprising of 53 reservoirs from 2.88 to 6.93 ha, and finally, category 3 consists of 50 reservoirs and spans from 7.02 to 32.49 ha.

¹⁸ An earlier study on reservoir distribution that partially covers the same area confirms this absence of reservoirs in the area that is solely covered by scene 195/052. Further west, reservoirs are found again in the sparsely populated Upper West Region (see VAN DE GIESEN et al. 2002, p. 167).

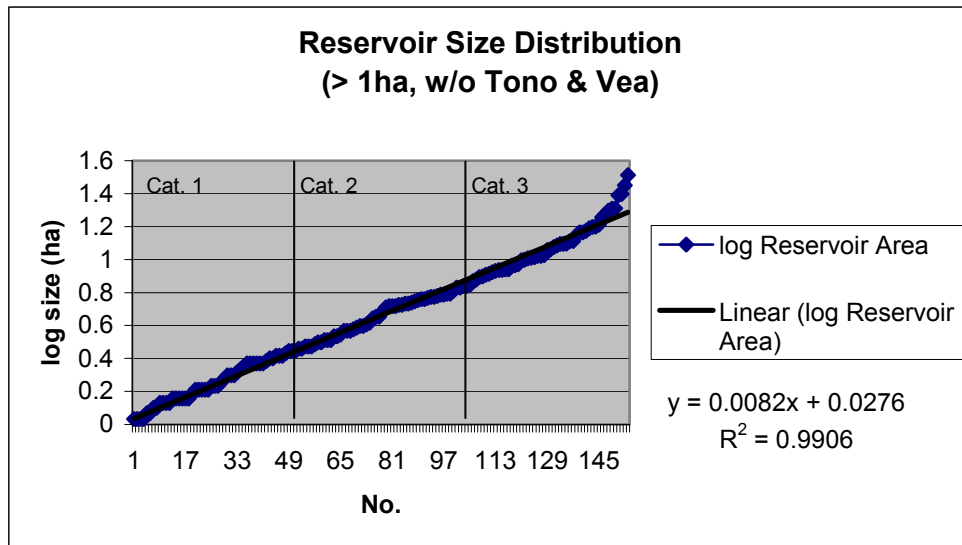


Figure 20: Size distribution of reservoirs and categorization.

Plotted against the number of reservoirs is the distribution of logarithmic reservoir sizes. The total no. of reservoirs involved is 154, which make up a total area of 999.54 ha. The vertical lines indicate the segmentation into three equally large categories. Reservoirs smaller than 1 ha, as well as the two large reservoirs Tono and Vea were discarded.

Problematic was the decision on the number of reservoirs to be measured. There is no statistical means to determine the number of reservoirs that needs to be measured in order to achieve a representative sample. A plausible solution is to have an extensive sample set to practically ensure to have a sufficient coverage. By measuring 60 out of the 154, or 40% of the total population, the variance that occurs is expected to be adequately represented.

Thereupon, 25 reservoirs were randomly selected within each category. The first 20 drawn reservoirs of each category were selected for field evaluation, leaving five spare samples per category. Following the order they were drawn, they were supposed to be subsequently used as substitutes in case of misclassification, dam failure, or other unforeseen events making the evaluation impossible (Appendix 8).

An extensive description and evaluation of the reservoirs follows in Chapter 3.3.2 and 5.

3.3 Collection and Processing of Field Data

3.3.1 Set-up and realization of field work

The randomly selected reservoirs were extensively measured during the fieldwork from 15th January 2002 until 13th February 2002. The equipment used for the collection of field data (Table 3) consisted of the following items:

Table 3: Equipment used for the collection and handling of the field data

<i>Hardware:</i>	<i>Software:</i>
1 Inflatable Boat with solid stern wall, solid floor and ore-locks	GPS Trackmaker 11.7
3 GPS Garmin GPS 12	IDRISI 32 Release2
2 Walkie-Talkies	ArcView 3.2
1 Level	Surfer 7.0
1 Tripod	
1 Telescopic Stadia Rod (5m)	
1 Rope & Plummet/Perpendicular	
1 Digital Camera and flash card reader	
1 IR Thermometer gun	
1 Laptop	
1:50,000 Maps of the Upper East Region	

The dimensions of the reservoirs were surveyed in the following way:

1. *Shape and size of the surface area were determined by walking around each reservoir with a handheld GPS, taking large numbers of points along the shoreline.*

The outlines created in this manner consisted of 25 (Dam 114, C1) to 502 (Dam 101, C3) points. Great care was taken to accurately measure the shape of the reservoir. The tail end was not always easy to locate. In the case when the reservoir merged into a stream channel, the ‘end’ of the reservoir was considered the first passable place from the one side of the shore to the other.

2. *Depths were measured at steps of 5 cm from the rowboat. Instead of a plummet, the stadia rod was used to measure the depths. Each measurement was accompanied with its GPS coordinates to locate its whereabouts within the reservoir.*

Therefore, the GPS's used were cross checked for conformity – both in dry runs before the actual field work and before the measurement of each reservoir – and rarely exceeded deviations of 1 meter between the units. This conformity was a presupposition for the use of two separate GPS units, since a match between the depth measurements and the outlines has to be given.

The general idea behind depth measurements in reservoirs with the aim of adequate volume estimation is based on finding its deepest point from which can be interpolated to the shores. Large numbers of points taken between the deepest point and the shoreline then determines shape, which is generally the convexity of the reservoir basin. The collection of the depth data, however, was not done according to a predefined grid. Each reservoir was measured according to unique judgments to take into account the local variations and characteristics, such as side arms, asymmetric basin shapes, sub-surface stream-channels, etc. Care was taken to achieve good coverage of points well spread over the reservoir while focusing on the parts close to the dam wall, where the deepest point is generally found. In addition, shallow parts at the edges, bay-like shore parts and tails were carefully measured. In the tail ends, morphological stream channel characteristics such as undercuts and slip-off slopes were also taken into account where they could be identified. For each dam, the number of measurements ranged from 25 (Dam 114, C1) to 171 points (Dam 61, C3).

The biggest problem turned out to be navigation with the most underestimated factor being the wind causing a lot of drift. For the same reason, navigation with the GPS was not possible as reading positions took too long. Instead, on-shore fixed points such as trees, rocks, houses, etc., were used to roughly gauge positioning within the reservoir and to row in approximately straight lines along which measurements were taken. Distances from one to the next measuring point could be approximated from turbulence induced by rowing. Through this turbulence on the water surface, it was generally possible to see where the rowing began and hence the distance from the last measurement point could be approximately estimated. Once rowing was stopped, the depth was quickly measured with the telescopic stadia rod. Meanwhile, a GPS waypoint was acquired and after getting the stadia rod back on the raft, the waypoint ID and depth were noted.

Taking measurements with the stadia rod revealed the benefit of better control over perpendicular immersion in comparison to using a plummet, especially when wind was causing drift to the raft. Where the reservoirs had muddy ground, the impact of the stadia rod could also be controlled better, preventing the measuring tool from sinking in the mud. In the few cases where the maximum depth of the reservoirs exceeded 5 meters, the stadia rod was extended with a rope.

Additionally, the surface temperature was always measured with the IR thermometer gun, approximately in the center parts of the reservoir. As the surface temperature varies during the course of the day, the time of acquisition was simultaneously recorded.

- 3. Difference in height between the actual water table and the maximum storage capacity as defined by the height of the spillway was evaluated with a level mounted on a tripod and the stadia rod.*

In order to get an overview of actual and maximum levels, the height difference was measured. A level mounted on a tripod was therefore used in combination with the stadia rod. The maximum level was generally defined by the lowest point along or aside the dam wall, which in general is a built spillway. Where erosion cut gullies to lower levels than the constructed spillway, these points were referred to as spill-levels. As this was not always clear at first sight, locals were often asked for the places where water overflows before reaching the dam crest.

Upon completion of the above steps, the GPS data of both the outlines and distribution within the reservoir were always checked on-site by downloading to the laptop and evaluating its quality. Thus it was always checked, whether it was necessary to acquire further points to achieve good distribution of points throughout the reservoirs. Besides the physical measurements, the survey of each dam was rounded off by taking a number of pictures as well as collecting further information such as the date of construction, the constructor, use, stated problems, time and weather conditions. Measurement of the temperature is of potential importance to the evaporation modeling. Along with the temperature, which ranged from 15 to 22 °C, the time of measurement was recorded.

3.3.2 Modeling of dams and volume derivation

In order to derive the storage volumes of the surveyed reservoirs, a 3D-Model was created for each of them. Therefore, the outline and depth data was merged and organized in an xyz ASCII table (negative z score) then being used with the interpolation software Surfer with the following characteristics:

xyz – easting/northing/depth

Spacing in x- & y-direction: 1m

Method: Kriging

Fault file: (x,y)

Using the interpolation method Kriging, an interpolation algorithm that works on the basis of spatial correlation derived from semi-variogram analysis (MEIJERINK 1994, p. 110, 137-143), the point data was interpolated over a 1x1 m grid. Aiming at the modeling of the reservoirs only, three problems have to be solved:

- 1. Mainly in the narrow tails, but also in smaller 'bays' or coves framing the reservoirs, the distance between the shores is closer than the distance from the shores to the next depth measurement. This causes these areas to be split-up by the interpolation algorithm into a segmented, non-continuous, sequence of*

puddles, instead of a talweg-like depth line roughly centered between opposite shorelines.

To eliminate these bridge effects between the shores that account for the isolated puddles, breaklines were defined along the deepest part of the channels connecting the known data points, adding points where needed to define the channel where a straight line between points would cut across the shoreline. Breaklines are lines defined by xyz values at each vertex. During the interpolation, any given point on a breakline represents the z-value of the nearest vertex defining it, and is used in combination with nearby data points to calculate the grid node value.

2. Definition of the water table as a base for interpolation with z-score 0

The water table being represented by the shoreline has to be defined as the thought 0-level. It is the only contour line that is continuously known all around. Likewise, it functions as reference for all other parallels of equal depth. It is achieved by incorporating the outline of the reservoir as a breakline polygon, so each point along the shoreline is interpreted as a 0 value in the interpolation process.

3. The shoreline of a reservoir should define its outer dimensions. With kriging, however, the surface is also extrapolated among the shorelines of the reservoir to the edges of the grid, based on the characteristics of the evaluated spatial trends. With the focus on modeling the reservoirs only, the surroundings should be set to 0 and thus be disregarded.

As through the above mentioned steps, the interior of the reservoir is already represented correctly, only the excess extrapolation parts outside the reservoir have to be deleted. This is achieved by blanking the gridded data with a blanking polygon. In contrast to the previously used breakline polygon, the blanking polygon (xy coordinates) does not enclose the reservoir but those parts of the grid that are to be deleted. The area outside the reservoir is thus assigned a flag value (1.70141E+038), which was later replaced with 0 values using a script (Appendix 10). The resulting grids were then used for volume calculation. Finally, contour line maps and wireframe models were created and draped for visualization of the interpolation results.

As an example, Figure 21 shows the 3D-model of a reservoir (No. 101, Category 3). It was created from 502 GPS-readings delineating its outline and 126 depth measurements. The inset in the top right corner shows the distribution of the depth measurements, which cluster most densely in close range to the dam wall (top edge) to capture its deepest point (3.10 m). The remaining parts of the reservoir are evenly covered. In the narrow tail part, the above described breaklines were used to prevent from bridge effects between the shores. The reservoir had an area extent of 9.01 ha, and contained 100,435 m³ of water at the time of observation.

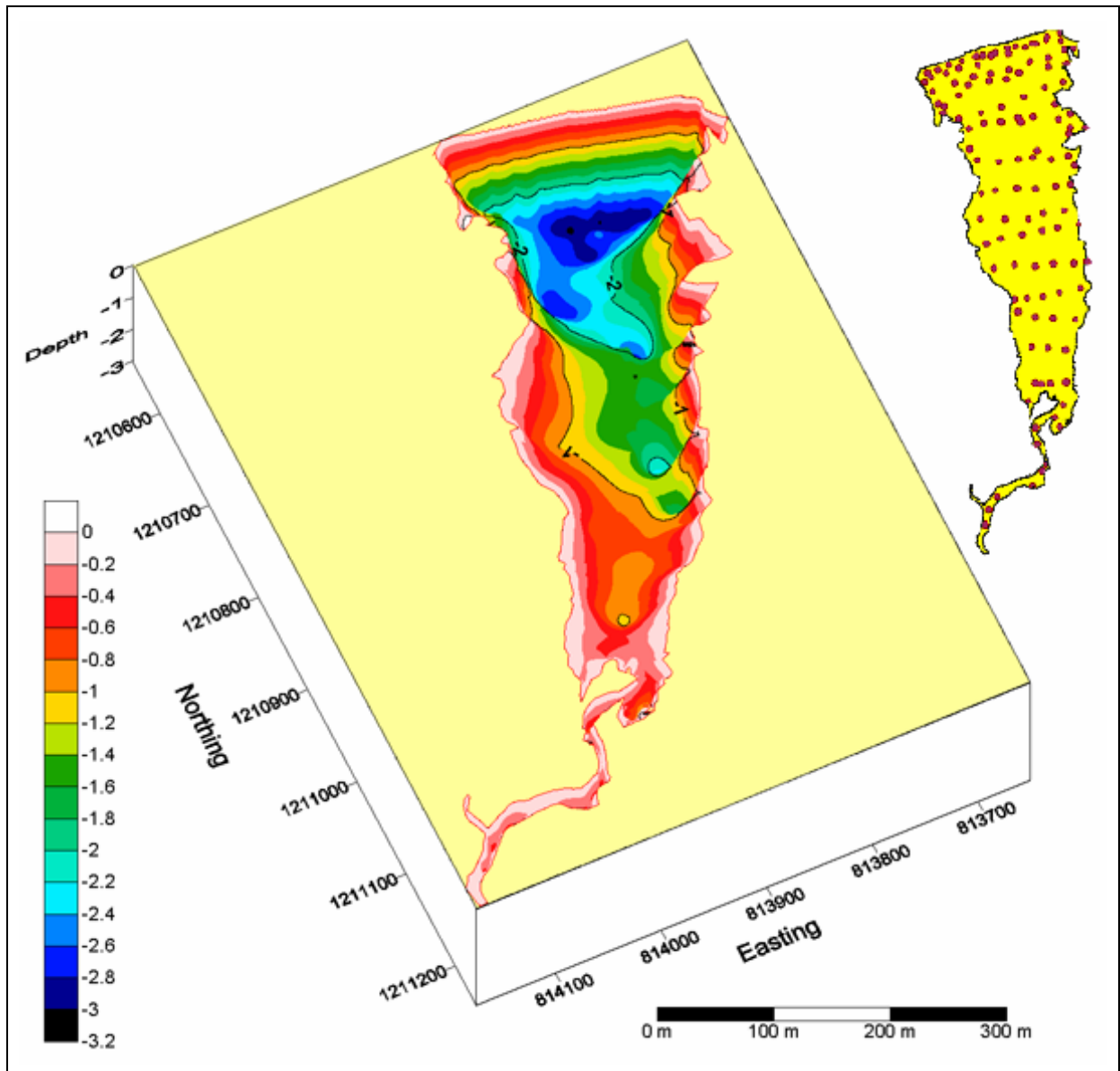


Figure 21: 3D model of Reservoir No. 101 and distribution of measurements.

The distribution of depth measurements (inset, out of scale) shows a high density in close range to the dam wall (top end), where the deepest point of a reservoir is expected. The remaining part of the reservoir was tried to cover with evenly distributed measurements (Referenced with UTM coordinates. Orientation changed).

Chapter 4

Data Description and Results

4.1 General Distribution of Reservoir Sizes

The aim of this chapter is an overview over the distribution of reservoirs in the Upper East Region. Already addressed in the previous chapter is the distribution of reservoir surface areas (Figure 20). On the log scale, the occurrence of reservoir sizes fits well with a linear regression. The smooth and constant increase of the reservoir size lined-up portends to the uniformity of the Upper East's topography. It can thus also be interpreted as a landscape measure. As the size distribution does not show abrupt breaks, the presence of different landscape units with considerably different landscape roughness can be neglected.

Besides the distribution of reservoir sizes, the distribution of their frequency shows further conformances with topographical attributes of the Upper East Region. Figure 22 shows, that – per area category – the largest number of reservoirs fall into the smallest area step (1-2 ha). In steps of one ha, the frequency distribution of reservoir sizes constantly decreases with increasing surface areas. The frequency distribution closely mirrors general laws that are applied to and derived from stream morphometry. As elucidated earlier, the Upper East's drainage network is mainly dendritic. After Strahler, drainage networks split up into segments of “stream order” (KNIGHTON 1998, pp. 10-11). The degree to which such a drainage network is branched describes Horton's “bifurcation ratio” (MARCINEK/ROSENKRANZ 1996, p. 170), the ratio between the number of streams in one order and the next. Expressed by Horton's “law of stream numbers” (KNIGHTON 1998, p. 12) is the expected number of streams of a certain stream order, calculated from the bifurcation ratio and the principal stream order. A further relationship discovered by Schumm is the “law of basin areas” (KNIGHTON 1998, pp. 11-12). It describes that the “mean basin areas of successive orders

tend to form a geometric series beginning with the mean area of the first-order basins and increasing according to a constant length ratio” (KARVONEN 2001).

Although the available drainage data is too coarse to be of use evaluating the above mentioned, general deductions out of these laws are still possible. These are:

1. *the frequency of lower order segments is expected to be greater than that of higher order (the same accounts for river junctions), and*
2. *the basin areas associated with stream segment of lower order are smaller than those belonging to higher order segments.*

Combining these, it can be further deducted that

3. *the number of small reservoirs (situated at low order streams or junctions) is larger than that of large reservoirs (situated at higher order streams or junctions).*

The last mentioned deduction, of course, requires relativization. It mixes the naturally occurring phenomena of stream morphometry with man-made features that are an expression of human decision and planning. However, a number of influencing factors make this deduction feasible. First, the construction-sites of reservoirs in the Upper East are bound to streams and their morphometry. Secondly, the higher frequency of lower order segments also stands for a greater number of opportunities for dam constructions, and vice-versa. Their dimensions are comparably small, but their construction is easier and cheaper, which, again,

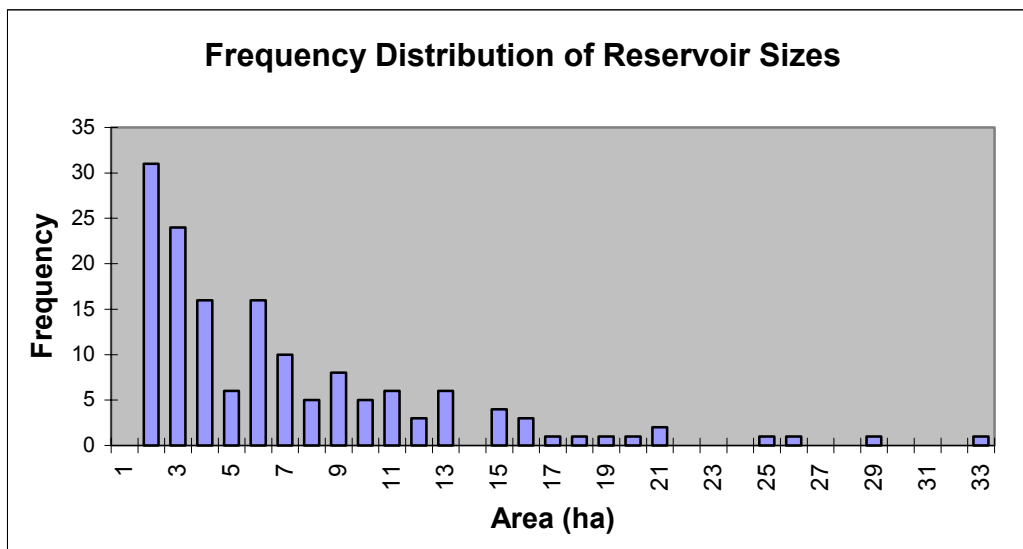


Figure 22: Frequency Distribution of Reservoir Sizes.
The histogram of area sizes mirrors structural properties of the Upper East’s mainly dendritic drainage system.

addresses a large number of potential institutions, donors, development agencies and cooperators who trust their ability to plan, build or fund such construction projects.

The conversion of Figure 22's frequency to log frequency yields a distribution that fits with a linear regression ($y = -0.0516x + 1.2933$, $R^2 = 0.7999$). The distribution of reservoir sizes frequencies, and the distribution of streams per stream order according to the law of stream numbers, is presumably indicative of having in common their fractal nature (TARBOTON et al. 1988, MANDELROT 1983).

4.2 Spatial distribution of Reservoirs and Reservoir Sizes throughout Upper East

Having found regularities in the statistical distribution of reservoir surface areas, their spatial distribution is now in focus. Of interest is both the distribution of reservoirs throughout the Upper East Region, as well as the spatial distribution of reservoir-sizes.

Linking reservoir sizes to topographic properties, such as slope angle, yielded no further insight. The reason therefore supposedly lies mainly in the coarse resolution of the hypsometric data. With a vertical resolution of 15 m (50 feet) the steps between adjacent contour lines is almost three times the greatest depth of the deepest reservoir. The fact that most of the reservoirs are located in areas above the mean elevation of (197 m), and that a large number of reservoirs is located at the transitions between areas of different standard deviations was thus only perceived, but not followed any further.

A previous study on reservoirs in Southern Burkina Faso and parts of the Upper East Region mentioned administrative boundaries to have an influence on reservoir distribution (VAN DE GIESEN et al. 2002). This is also clearly the case in the Upper East Region. The map in Figure 23 shows, how the sizes of reservoirs spread over the districts of the Upper East. The pie charts below the district names illustrate the ratio of reservoir frequency per category. The size of the pies is scaled according to the total of a districts reservoir surface area. Especially Bawku West outstands through its vast dominance of third-category reservoirs. In Bawku East, reservoirs of category two and three (in equal parts) make up 85 % of the total number of reservoirs. In all other Districts, the reservoirs of the smaller categories dominate in number, slightly differing in their make-up (Table 4).

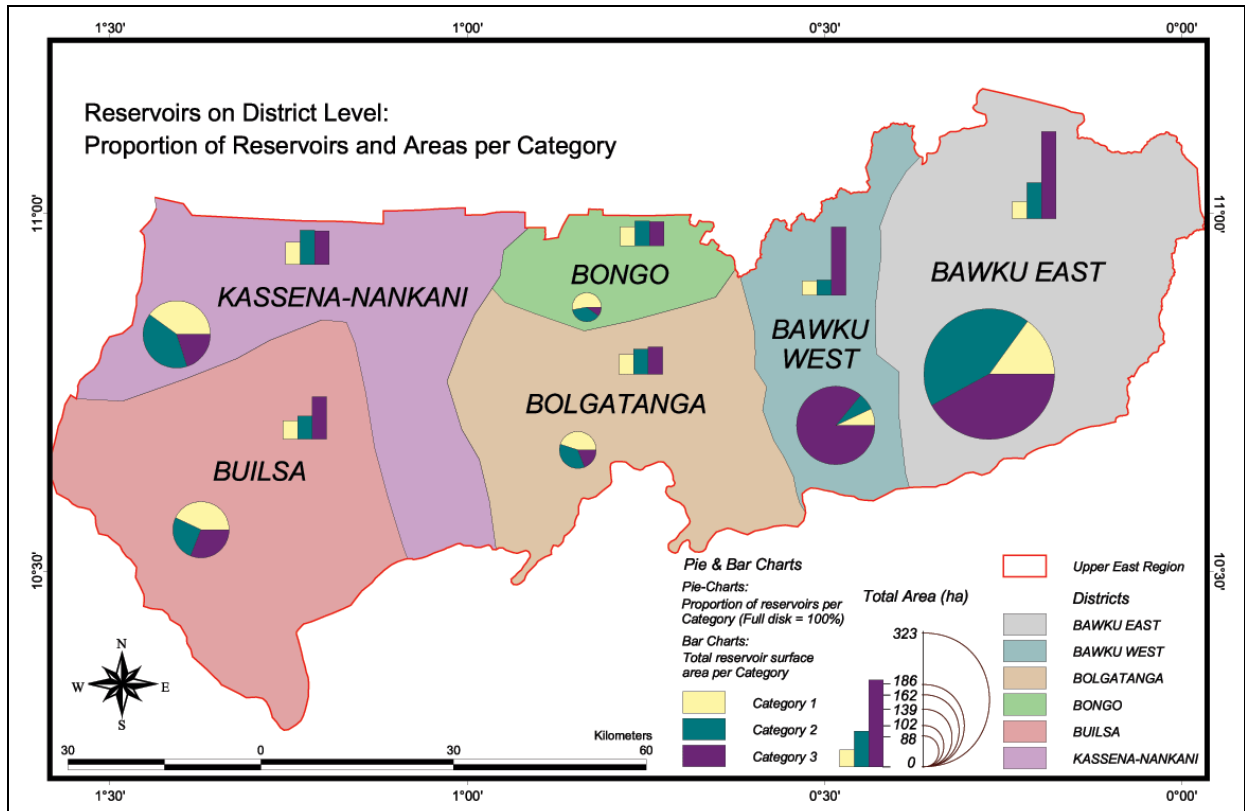


Figure 23: Distribution of Reservoir Sizes with regard to administrating boundaries.

The pies show the proportion of reservoirs per category. The size of the pies is scaled to the total surface area that were classified for each district. The bar charts split up the total surface area into the three categories.

The bar charts above the district names (Figure 23) break down each district’s total reservoir surface area as indicated by the pie size into total area per category. Clearly identifiable is the dominance of third category reservoirs in Bawku West and Bawku East, followed by the total areas of the second and first category. Less drastical is this difference in the districts Builsa and Bolgatanga, where the contributing categories rank in the same order. Bongo and Kassena-Nankani show a more balanced distribution. In these two districts, the reservoirs of category two make up for the largest surface area, closely followed by those of category three, and finally of category one (Figure 23 and Table 4).

Table 4: Reservoir Frequency and Area Distribution by District

District	No. of Reservoirs				Surface Area (ha)			
	Cat. 1	Cat 2	Cat 3	Total	Cat 1	Cat 2	Cat 3	Total
Bawku East	6	17	17	40	11.34	72.36	239.40	323.10
Bawku West	1	1	13	15	2.79	5.67	177.93	186.39
Bolgatanga	10	8	4	22	19.35	37.71	44.46	101.52
Bongo	10	7	2	19	17.91	35.91	34.38	88.20
Builsa	10	6	7	23	14.94	30.51	93.06	138.51
Kassena-Nankani	14	14	7	35	28.17	67.77	65.88	161.82
TOTAL	51	53	50	154	94.5	249.93	655.11	999.54

In a more detailed view, the human influence on reservoir location becomes even clearer. Figure 24 illustrates where the reservoirs are localized within the districts. The reservoir sites are coded with differently sized circles according to the category they fall into. Besides the reservoirs, the map also shows the drainage and the road network in blue and black color respectively.

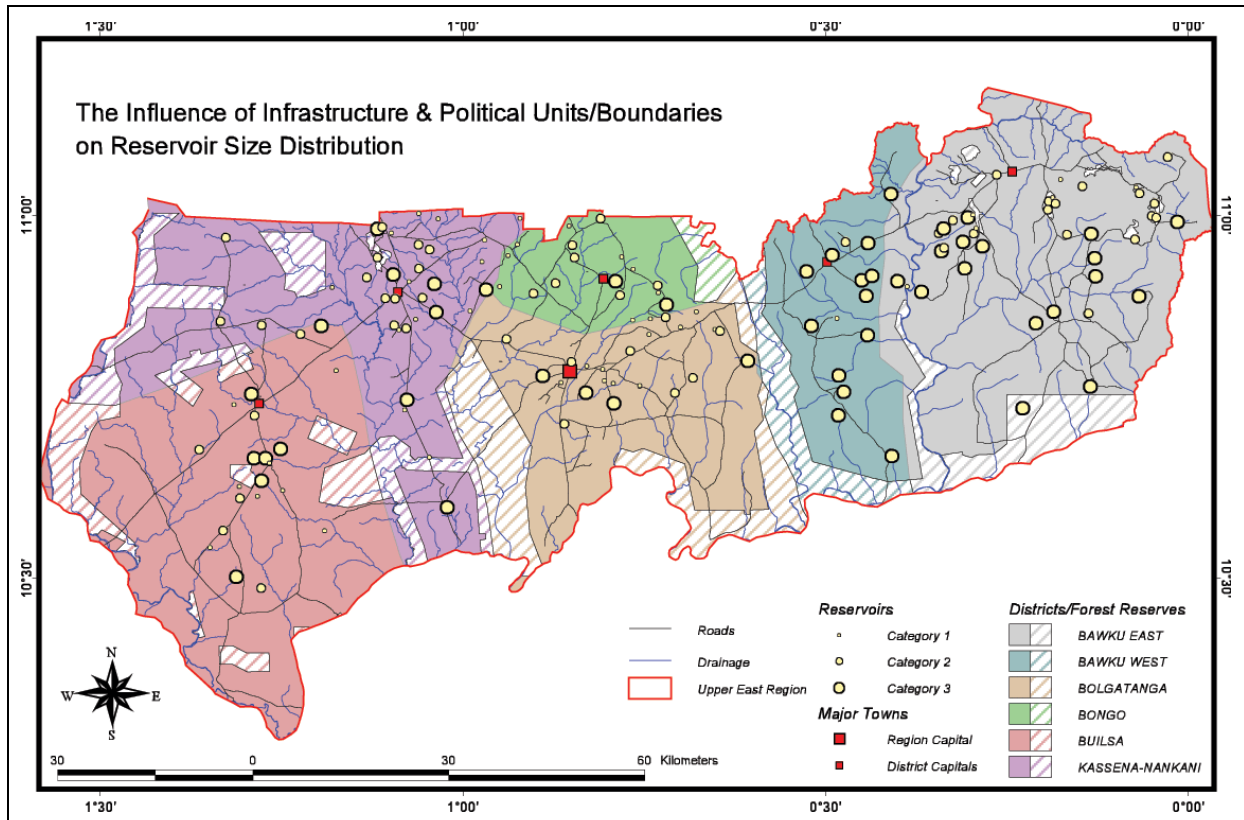


Figure 24: Distribution of Reservoir Sizes with regard to infrastructure and political units/boundaries. Rather than the river network, the presence of and access to infrastructure is the determinant factor for the construction of dams. Within the political boundaries, different degrees of commitment to agricultural development are reasons for the different size distributions. Forest reserves are a restriction to dam development.

Although the drainage network and its valley shapes are the prerequisite topographic features, it stands out that the location of a reservoir is much more determined by the fact whether or not there is a road in proximity to a potential dam site. It is obvious that these locations are favorable. Construction logistics are easier to cope with when the building site is well accessible, and once a reservoir is in (commercial) use, access to transport is important to bring the perishable goods to market fast.

A last conclusion that can be drawn from the above map relates to the distribution of forest reserves which as indicated by the hatched areas. In total, these occupy quite a large area of the Upper East Region and are there a restriction to dam construction. In the southern part of Bawku East occurs the only single case, where a reservoir lies within a forest reserve.

Although the elevation model was already identified to have a too coarse vertical resolution to obtain variables that help to explain the distribution of reservoirs or reservoir sizes, a derivate of it still deserves mentioning and interpretation. Depicted below (Figure 25) is a map that shows steps of one standard deviation (35.33 m) from the mean elevation (197 m above sea level). Most of the reservoirs are located in areas above the mean elevation. Therein again, they favorably arrange in close range to the mean elevation or at the edge to the next standard

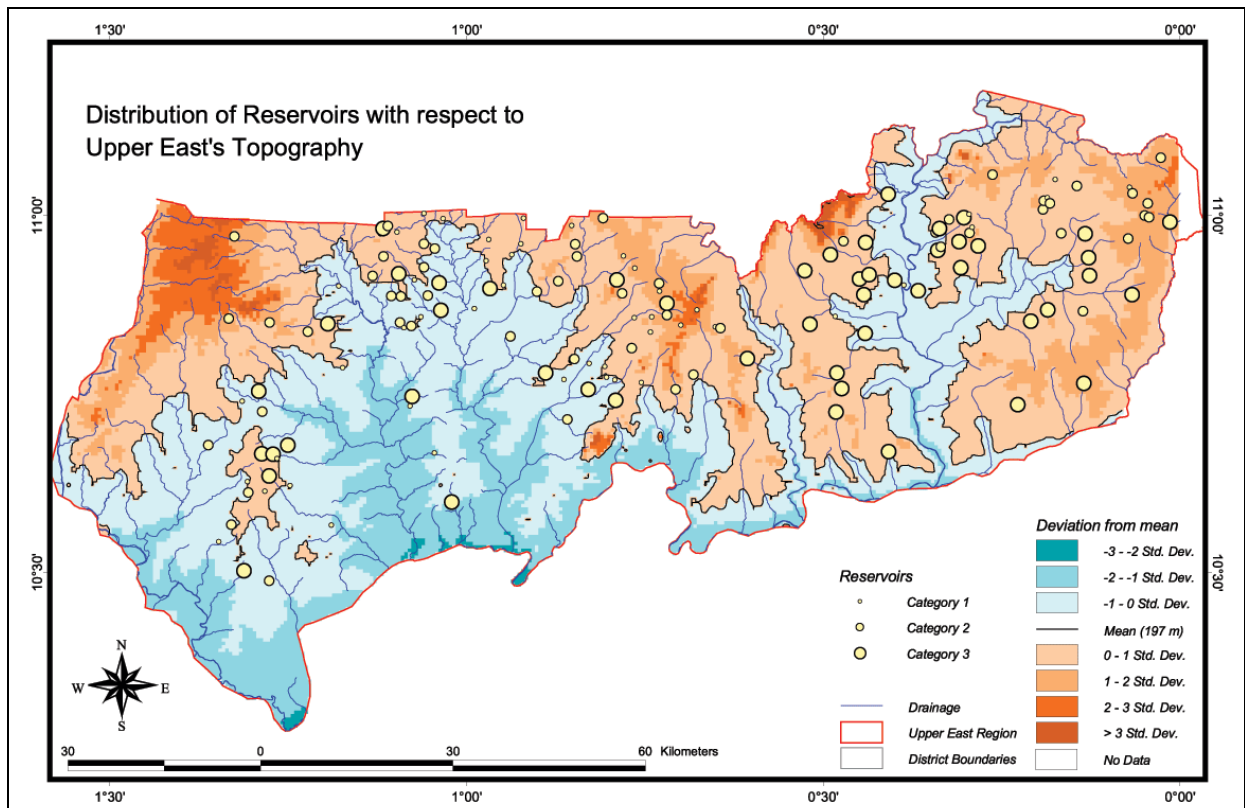


Figure 25: Distribution of Reservoirs with respect to Upper East's Topography.

The vast majority of reservoirs are located above the mean elevation of 197 m, mainly within +1 standard deviation (35.33 m) from the mean.

deviation step. Especially conspicuous is the two-sidedness of elevation distributions. Roughly the western half of the Upper East Region is mainly occupied by areas of the lower elevation ranges. These lower ranges show a lack of reservoirs in comparison to the upper elevation ranges. This is due to the fact, that these places are much less populated. The extensive floodplains and the occurrence of river blindness make these areas unfavorable habitats. Agricultural production there makes use of the waterlogged soils. In the higher elevations of the western part, or at least in proximity to the mean elevation, reservoirs suddenly occur in greater number. The larger area above the mean elevation in the very west is almost free of reservoirs. Towards the Upper West Region, the population density becomes noticeably lower. In contrast, the eastern half of the Upper East Region is mainly comprised of the upper elevation ranges, offering larger areas well suitable for settlements. In these densely populated areas the spread of reservoirs is more distinct. As already mentioned, river blindness takes its toll in the close range to the rivers, especially along the Red and the White Volta, where reservoirs are fewer.

From a topographic point of view, conditions favorable for dam construction can finally be deduced from Figure 25. The contours that are drawn by the elevation level's boundaries are not particularly straight over long distances, but lively wriggle back and forth according to the course of coves and ledges. The coves or valleys they describe offer ideal topographic conditions for dam construction.

Overall, the spatial distribution of man-made reservoirs and reservoir sizes differ from that of naturally occurring water bodies (SAGAR et al. 1995, SAGAR et al. 2002). The 'absence' of topographic explaining variables thereby needs relativization as the resolution of the available elevation data is too coarse. Despite the requirements of topographic premises, the distribution of man-made reservoirs relies to a great extent on the man-made decision whether or not to make use of the natural inventory to build them. The vast part of reservoir locations can be interpreted as based on decision-making that attaches most importance to the presence of roads in close range.

To round-off the discussion on the distribution of reservoirs, and lead into the analysis of the field data, the map below (Figure 26) shows among all reservoirs the distribution of reservoirs that were measured in the field trip. As reservoir sizes are split up into the three categories, the distribution of size categories is represented by differently sized circles. Based on the information gathered at the reservoirs depicted with blue circles, the following chapter seeks to find regularities that can be applied to the remaining reservoirs (yellow dots) in order to derive their volume.

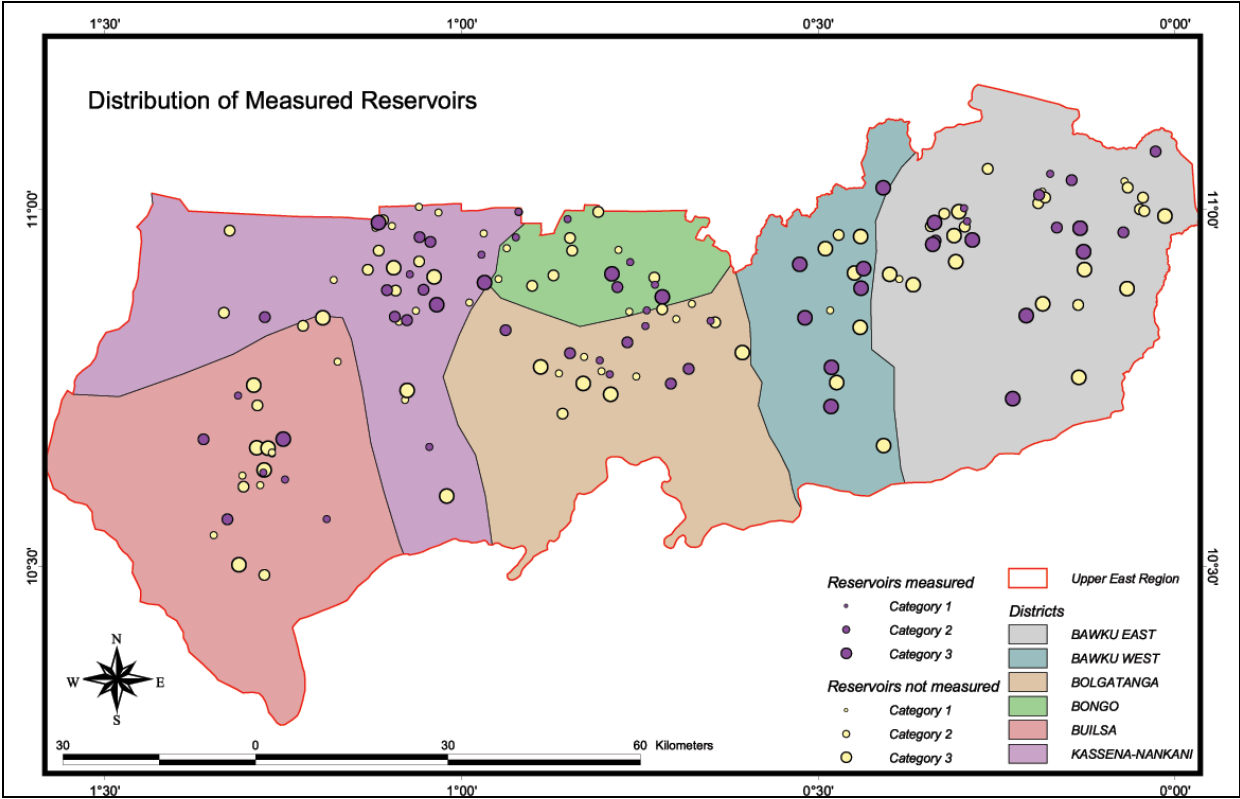


Figure 26: Distribution of Measured Reservoirs. Depicted in blue circles is the distribution of measured reservoirs. The categories are indicated by the size of the circles. The yellowish circles represent the remaining unmeasured reservoirs.

Chapter 5

Data Analysis

5.1 Examination of postulated relations

5.1.1 Area_(Satellite) – Area_(Field) – Correlation

A very basic presupposition for this study is that remote sensing may be a suitable means to detect reservoirs and adequately measure their surface areas. In the following, this assumption is tested.

In chapter 3.2.3, the reflectance properties of surface water bodies were described. One stated problem was the assignment of pixels along the edge of reservoirs. According to this, shallow areas show a higher spectral mix with soil reflectance patterns (bottom reflection), especially in cases with turbid water (volume reflection). The second problem is that of mixed pixels, where a pixel is composed of more than one land cover category, and unique assignment is not possible. Errors thus occur, depending on the decision of the classifier to omit or commit an edge-pixel to the water body. The impact on the data is bigger, the smaller the reservoir is.

Ideally, field trips for ground truthing of satellite image classifications are conducted in close range to the date of acquisition of the satellite imagery or otherwise should be scheduled near anniversary. The land cover properties that are found on near anniversary dates are expected to resemble the satellite imagery most closely. Unfortunately, the field trip had to be conducted in the range from 14th January to 13th February 2002. Different rain records of 1999 (Figure 13) and 2001/2002 (Appendix 6) account for inter-annual differences. In addition, the times of acquisition of the satellite and field data have to be seen in the context of the seasons. While the satellite image was acquired just after the end of the rainy season (9th November 1999) and is expected to closely represent its maximum dimensions, the field evaluation was conducted in the middle of the dry season, so seasonal changes (intra-annual)

have already had an effect on reservoir dimensions. These are seepage, evaporation, and mainly draft that has already taken place since the maximum fill.

The relation between the area measurements from the field data and the satellite image classification can be expressed in terms of a linear regressions of the form

$$y = ax + b \tag{2}$$

where

$$a = \frac{n(\sum xy) - (\sum x)(\sum y)}{n(\sum x^2) - (\sum x)^2} \tag{3},$$

and

$$b = \frac{(\sum y)(\sum x^2) - (\sum x)(\sum xy)}{n(\sum x^2) - (\sum x)^2} \tag{4}.$$

Over the whole range of the data the linear trend of Area_(Satellite)-Area_(Field) correlation (Figure 27) is thus expressed by the equation:

$$Area_{(Field)} = 0.9366 * Area_{(Satellite)} - 0.7746 \tag{5}$$

As assumed due to the off-near anniversary date, reduction of area is represented in this equation. The R² of 0.88 is still relatively high.

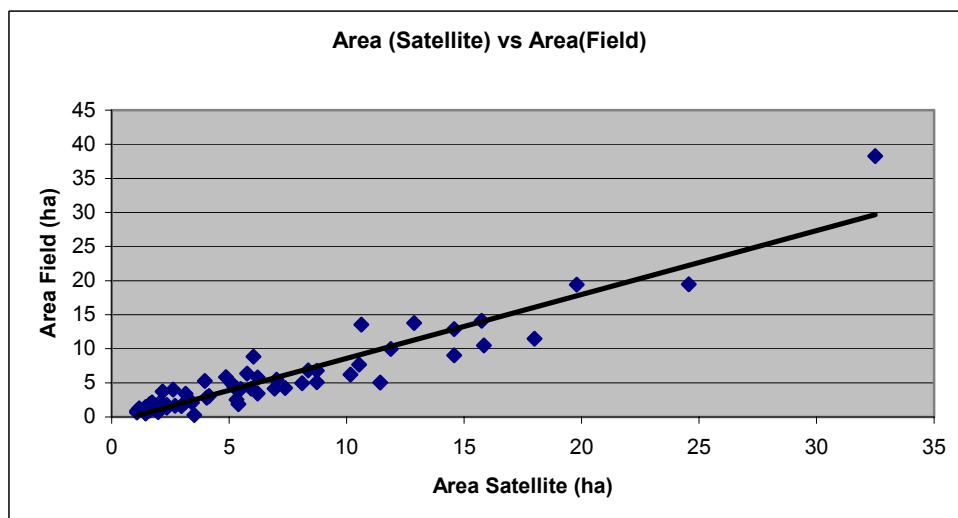


Figure 27: Area_(Satellite)-Area_(Field) correlation.

The correlation between remotely sensed and measured reservoir sizes should be very close. The differences are due to non-near-anniversary observations.

To a certain degree, the $Area_{(Satellite)}$ - $Area_{(Field)}$ -correlation can be seen as a quality measure for the classification. In this case, the commonly known confusion matrixes that are used to calculate errors of omission and commission are not particularly useful. As the area extent of reservoirs changes both inter-annually and seasonally, they would compare variable features recorded in different years at non-near-anniversary times. Errors arising from inter- and intra-annual changes can not be accused to the satellite image classification. With focus on two different kinds of correctness or accuracy, the quality of the classification results can still be assessed. The first of these is the reservoir determination. Concerning the reservoir determination, the classification proved to be good. The classified reservoirs selected by random sampling were all existent, except for two cases, where reservoirs no longer existed as their dam wall collapsed in the time range between the 7th November 1999 and the field observations. It can thus be stated that misclassifications (e.g. with swamp or burned areas) did not occur. The error of commission must thus be close to zero. The two dam failure sites were closely looked at in order to get more information on the basin shapes as they develop after the dam construction. The two above-mentioned broken dams (No. 142 and No. 266, Category 3) were then substituted with two reservoirs subsequently following on the list of spare reservoirs (No. 59 and 133, see Appendix 9) that was generated together with the random sampling of reservoirs to be evaluated.

The second kind of measure for the goodness of the classification is the area determination. It is clear that the reservoir areas derived from the satellite image are expected to be larger than those recorded during the field trip, all due to the off-near anniversary data collection. This is generally, but not always the case. The deviations from $Area_{(Satellite)}$ to $Area_{(Field)}$ should be seen in relation to their size (see also Appendix 11) so that the deviations become comparable. This can be achieved by means of a *Normalized Difference Area Index (NDAI)* which weights the deviations. It is expressed as

$$NDAI = \frac{(Area_{(Field)} - Area_{(Satellite)})}{(Area_{(Field)} + Area_{(Satellite)})} \quad (6),$$

where *NDAI*-values have a potential range from -1 to 1. Reservoirs with values close to 0 have the best match between $Area_{(Satellite)}$ and $Area_{(Field)}$, while values increasing to both extremes stand for increasing deviations between surface areas. Negative values resemble reservoirs where $Area_{(Satellite)} < Area_{(Field)}$ and positive values represent $Area_{(Satellite)} > Area_{(Field)}$ (see Figure 28).

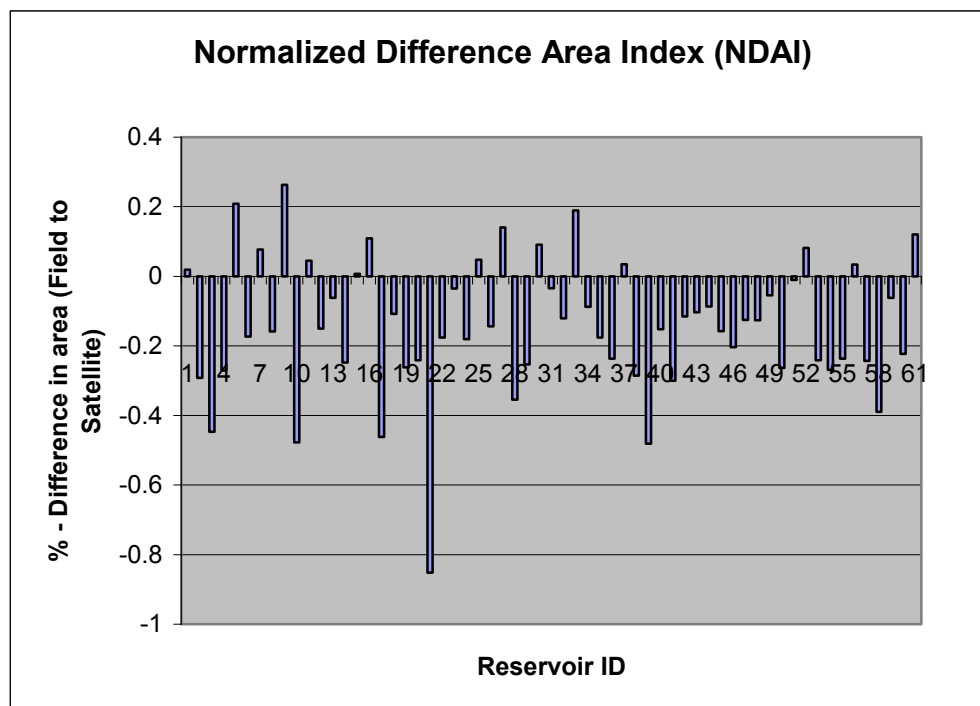


Figure 28: Normalized Difference Area Index of surface areas between 1999 and 2002. Negative values resemble reduction in area in the field compared to that of the satellite image. Positive values mirror greater areas in 2002 compared to 1999.

The NDAI levels off at a reduction in area of about 13 % in all three categories as well as over the whole range of the data set. The reasons for the reduction in area are manifold. They can be physical (low initial fill level due to rainfall, seepage, evaporation loss), human induced (draft for irrigation, building, cattle, and various domestic uses) or through image processing (median filtering). Reservoir No. 63 stands out with an NDAI larger than -0.8. This particular reservoir was almost completely drained for agricultural production. Due to this extreme drainage, an additional reservoir was therefore measured, increasing the total sample size to 61 reservoirs.

Out of the 61 reservoirs measured, 15 show larger areas in January/February 2002 than those obtained through the satellite image classification. 10 of the 15 reservoirs have a deviation in the order of less than one hectare. A simple a-posteriori explanation of this unexpected “increase” in size identifies the difference between satellite image classification and the on-site work in handling the occurrence of a special condition, which is the occurrence of dense carpets of (floating) herbaceous vegetation that is mainly found in the tail part of some reservoirs. Especially at reservoir no. 282 (Figure 29), but also at others, herbaceous water plants cover large areas in the tail part. On the satellite image depicted to the left it can be seen that these densely vegetation covered water surfaces were not classified as water during

the satellite image classification¹⁹. In fact, the water can still be deeper than 50cm, but the herbaceous vegetation can be so dense that the water is hardly visible.

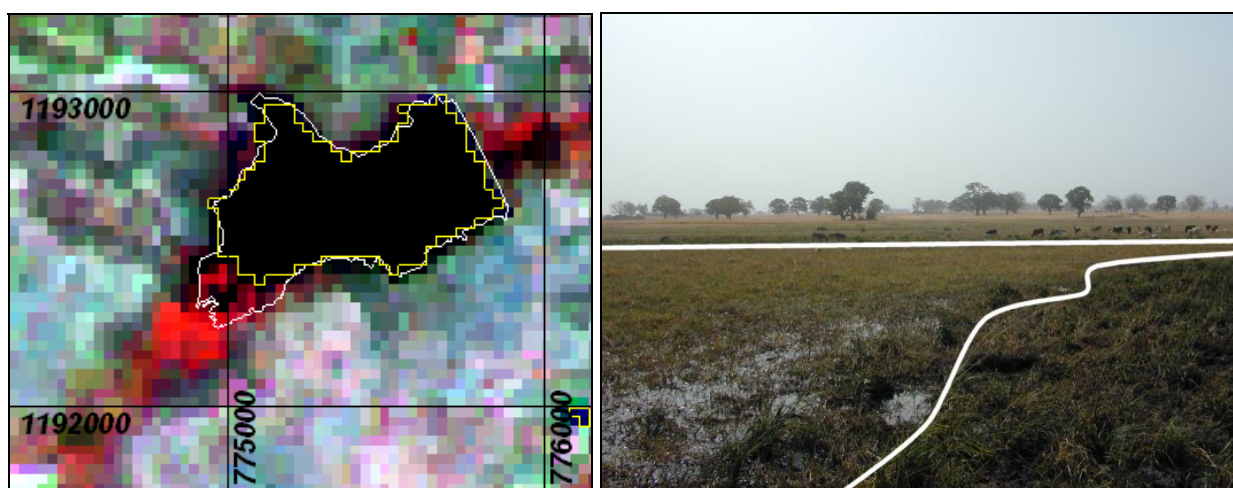


Figure 29: Herbaceous water plants in the tail part of reservoir No. 282.

The satellite image to the left shows the large extent of lush vegetation in the tail part of the reservoir. The yellow outline represents the classification result, the white outline delimits the extent that was recorded during the field trip. The picture to the right shows a part of this reservoir's tail, which resembles the red shaded part on the satellite image (left) that is within the white outline, but outside the yellow polygon. On the picture to the right, the white line separates the herbaceous water plants (bottom left section), which floats on the water, from vegetated solid ground. (Satellite image referenced in UTM coordinates, Photo taken 22.01.2002)

The second factor is the overestimation during the recording of the outlines by walking around with the handheld GPS as they are depicted in the above images. The interpretation of the land-water boundary is not definite in these cases, and “wading” in the boundary zone is both exhausting and can be dangerous, as these areas are hiding places for crocodiles.

Summarizing the above, the classification of satellite imagery is seen as an adequate means of detecting small reservoirs. Yet, seasonal and inter-annual changes have to be accounted for, as well as changes through withdrawal that can differ considerably amongst the reservoirs.

¹⁹ The problem of water or wetland detection under dense vegetation cover is a commonly known problem in optical remote sensing. BALSER (1996) proved, that multisensor data fusion, e.g. of Landsat with ERS (Radar)-Imagery is a useful solution. As in the Upper East large vegetation covered reservoir surfaces rarely occurred, multisensor data fusion was not applied.

5.1.2 Area_(Field) – Volume – Correlation

The existence of a correlation between area and volumes of reservoirs is the crucial element for the feasibility of applying satellite imagery for volume estimations over larger areas.

Generally, an area (A) can be expressed as a function of its characteristic length (l)

$$A = l^2 \quad (7)$$

while volumes (V) are generally calculated as a function of area (A) and depth (d).

In square-based bodies, a factor c defines a specific body's volume as a fraction of a cube's volume:

$$V = c * A * d \quad (8).$$

In a square based pyramid, $c = \frac{1}{3}$ as its volume is one third of a cube. As reservoirs approximately show the shape and volume of a pyramid longitudinally cut in half, the term is again multiplied with $\frac{1}{2}$. Thus,

$$V_{half\ pyramid} = \frac{1}{6} * A * d \quad (9).$$

In order to derive reservoir storage volumes by means of remote sensing, reservoir volumes have to be expressed as a function of their areas. This can be achieved by solving (7) and (9) for l and then equating them. To facilitate this, depth d of the half pyramid in (9) can be expressed as a fraction $\frac{1}{f}$ of a side length (l)

$$d = \frac{1}{f} * l \quad (10).$$

Thus, (10) and (7) combined with (9) gives

$$V_{half\ pyramid} = \frac{1}{6} l^2 * \frac{1}{f} l = \frac{1}{6 * f} l^3 \quad (11)$$

as an equation to calculate the volume for half a pyramid.

Solving equations (7) and (11) for l yields

$$\sqrt{A} = l \quad (12),$$

and

$$\sqrt[3]{6 * f * V_{half\ pyramid}} = l \quad (13).$$

Substitution of (12) into (13) gives

$$\sqrt[3]{6 * d * V_{half\ pyramid}} = \sqrt{A} \quad (14),$$

or solved for $V_{half\ pyramid}$

$$V_{half\ pyramid} = \frac{1}{6 * f} * A^{3/2} \quad (15).$$

Taking log left and right gives

$$\log V_{half\ pyramid} = \log \frac{1}{6} + \log \frac{1}{f} + \frac{3}{2} \log A \quad (16),$$

which is the equation for the expected area-volume correlation.

The first segment of this term indicates the fact that half a pyramid has $1/6^{\text{th}}$ of the volume V of a cube that has the same characteristic lengths l as the initial pyramid. The latter two parts of the equation represent the general volume definition consisting of area A and depth d , where the depth d is expressed as a fraction $1/f$ of the characteristic length l of the base area A .

In order to verify this theoretically derived assumption, the logarithms of areas and computed volumes of the reservoirs were plotted in Figure 30.

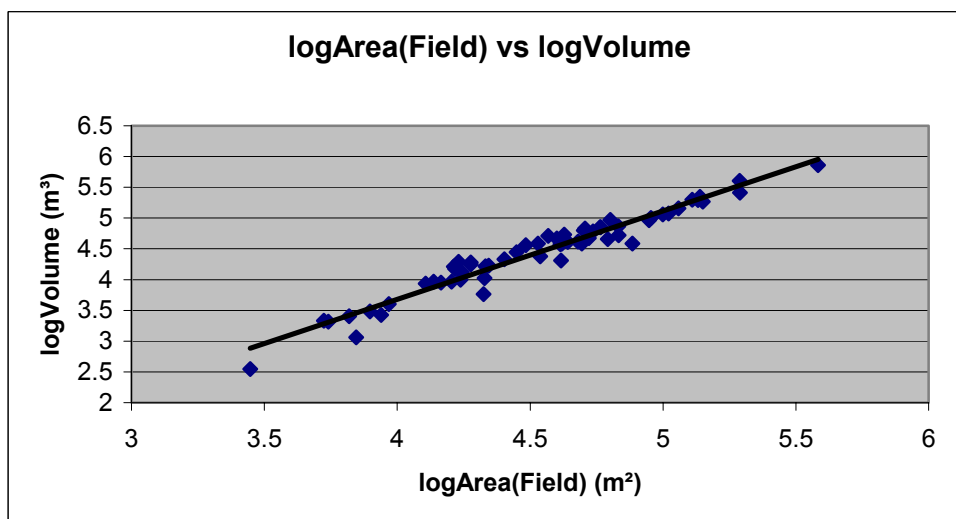


Figure 30: logArea_(Field)-logVolume relation.

The logarithms of surface area and volume show are linearly correlated.

The averaged reservoir can thus be described with the regression equation:

$$\log V_{\text{reservoir}} = -2.067 + 1.4367 * \log A \quad (17).$$

Its linear trend closely mirrors the theoretically derived relation. The second section of the equation, $1.4367 * \log A$, closely represents the correspondingly expected $\frac{3}{2} \log A$ from equation (16). Additional information is contained in the first section of the equation. Comparing (16) and (17) reveals that -2.067 in equation (17) is represented by $\log \frac{1}{6} + \log \frac{1}{f}$ in equation (16).

Thus,

$$-2.067 = \log \frac{1}{6} + \log \frac{1}{f} = -0.778 + \log \frac{1}{f} \quad (18).$$

As

$$\log \frac{1}{f} = -\log f \quad (19),$$

(19) in (18) gives

$$-2.067 = -0.778 - \log f \quad (20).$$

Solving (20) for f gives

$$\log f = 1.2889 \quad (21),$$

or

$$f = 19.45 \quad (22).$$

Substituting (22) in (16) then reveals that the depth d of a reservoir is $\approx 1/20$ of its characteristic length.

Making use of equation 16 to derive reservoir volumes by means of their area, the precision of the prediction needs to be known. Based on error variances, the goodness of fit between measured and modeled volumes can be evaluated. As quoted in BEVEN (2001, p. 225), the error variance σ_ε^2 is defined as

$$\sigma_\varepsilon^2 = \frac{1}{T-1} \sum_{n=1}^N (\hat{y}_t - y_t)^2 \quad (23),$$

where \hat{y}_t is the predicted value of the variable y for the observations $n = 1, 2, \dots, N$. The widely used model efficiency measure of Nash and Sutcliffe, which uses the ratio of the error variance σ_ε^2 and the variance of the observations σ_o^2 , is defined as

$$E = \left[1 - \frac{\sigma_\varepsilon^2}{\sigma_o^2} \right] \quad (24)$$

(referred to in BEVEN 2001, p. 225). Evaluating the goodness of the area-volume relation with this measure yields an excellent result. The model explains 97.5 % of the measured variance.

5.2 Exploration and use of Depth–Area–Volume Interrelations

5.2.1 General approach

The important conclusion drawn from the analyses conducted in Chapter 5.1 is the existence of close correlation between area and volume of reservoirs. The $\text{Area}_{(\text{Satellite})}$ - $\text{Area}_{(\text{Field})}$ -correlation, in contrast, shows lower congruence because of differences in water use intensities and non-near-anniversary comparison.

Based on the three assumptions, that

1. *the correctness of the satellite image classification and field measurement is given,*
2. *depth-area-volume interrelation may be evidenced, and*
3. *the year 1999 was a comparably wet year,*

it can be stated that the remotely sensed $\text{Area}_{(\text{Satellite})}$ approximately represents the true maximum storage capacity²⁰. Using depth-area-volume interrelations that are derived from field measurements, the measured reservoir-dimensions can be extrapolated to the 1999 level. A side effect of normalizing the field measurements to the 1999's extent is the reduction of the influence of different water use intensities. In other words, the NDAI of each reservoir then tends towards zero.

Figure 31 visualizes a reservoir's interrelations between area, depth and volume schematically. The surface plotted on the lowest level resembles the measurements taken during the fieldwork in January/February 2002. It is associated with the depth d and the volume $V_{\text{Jan/Feb 2002}}$, which was computed from the 3D-models (see Chapter 3.3.2). It further clarifies that the reduction of one of the three parameters also causes the other two parameters - as a direct consequence - to decrease, and vice versa. Deriving these regularities for each

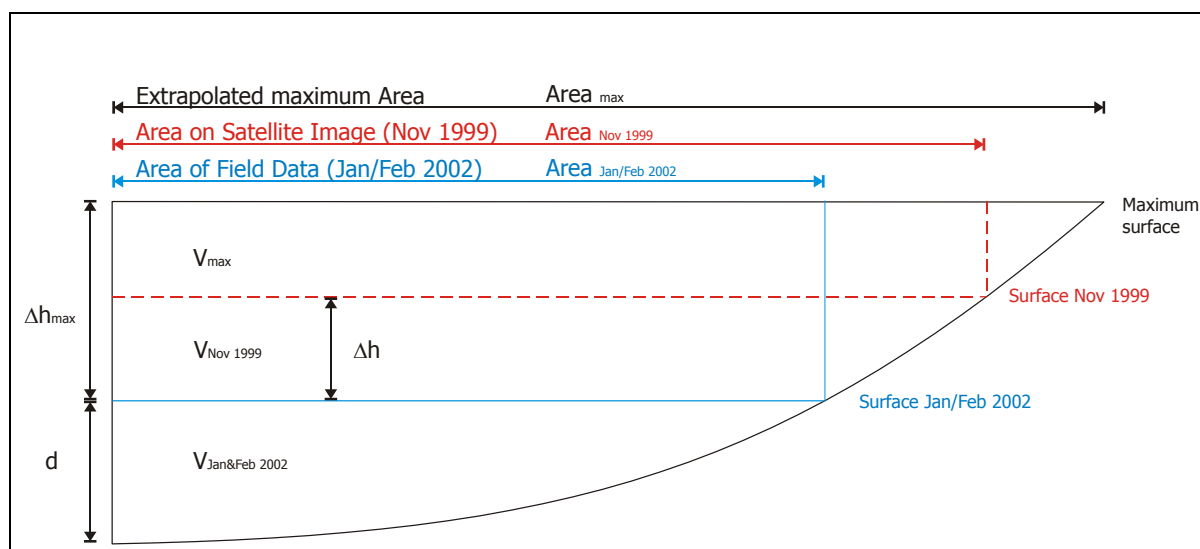


Figure 31: Area-, Depth-, and Volume-Interrelations of reservoirs.

Increasing one of the variables causes the other two to increase, and vice-versa. This interplay between area, depth and volume e.g. allows for the derivation of reservoir depth and volumes for different surface areas, both inter- and extrapolated.

²⁰ Areas and Volumes associated with each reservoir's measured depth d plus Δh_{max} are not expected to give a good representation of maximum storage volumes that are truly reached in reality. The relative height of each reservoir's spillway might be based on different return periods of events that cause spilling, aka. design floods. Poor construction and/or erosion of spillways also reveal that $(d + \Delta h_{\text{max}})$ is not a good reference point for maximum storage capacity.

measured reservoir allows their extrapolation to the desired level.

As every measured reservoir's area and volume is highly correlated with its depth, their linear regressions on log scale describe their areas and volumes very well for every depth step within the range of d . Areas and volumes can therefore be extrapolated with high confidence to each reservoir's potential maximum level, as $d + \Delta h_{max}$ are known from the field measurements. Consequently, $Area_{max}$ and volume V_{max} can be derived from this extrapolation. As elucidated above, the $Area_{Nov\ 1999}$ is seen a better indicator for real maximum fill levels. Knowing the extent of these areas from the satellite image evaluation, in turn, associated depths $d + \Delta h$ and volumes $V_{Nov\ 1999}$ can be derived (see Figure 31).

The following paragraphs seek to describe the extrapolation process and derivation of equations capable of describing the found correlations for the $Area_{Nov\ 1999}$ reference level. Upon these, the reservoirs not evaluated in the field trip are introduced in the modeling.

In a latter stage, all reservoirs are sought to be combined to one large "super-reservoir" incorporating all reservoirs' properties. Implementing such a super reservoir, evaporation losses from reservoirs can be calculated at relative ease.

The subsequent paragraphs focus on the evaluation of area-volume and depth-volume curves, which are a presupposition for the creation of such a super reservoir.

5.2.2 Derivation of Area-Volume-Curve

Based upon the findings on $Area_{(Field)}$ -Volume correlation as tested in paragraph 5.1.2, geometric regularities can be stated. Initially, this data was derived using the 3D-model, whose generation was described earlier. However, the 3D-models have further analytical value, which can be utilized for the creation of the super-reservoir. They can thus not only be used to compute volumes, areas and depths of the reservoirs at the time of measurement, but also to calculate corresponding surface areas and volumes at different depth levels. Like draining water through the sink of a washbasin, this is achieved by lowering the hypothetical water table in steps of 5 cm and re-calculating volumes and areas until the reservoir is empty. This was attained by means of an IDL routine, which was programmed to compute each reservoir's area, and volume at all corresponding depth steps (see Appendix 12). The output from this computation allows the creation and evaluation of $\log Area$ - $\log Volume$, $\log Area$ - $\log Depth$ as well as $\log Depth$ - $\log Volume$ curves for each measured reservoir. Focusing on Area-Volume relations in this paragraph, the latter mentioned relations are of value for the following paragraphs.

In log-log notation, each reservoir's Area-Volume relation has been evaluated. This relation proves to be expressed adequately by linear regressions of the familiar form (2). For the separate reservoirs, R^2 's are throughout larger than 0.9453 and correlation coefficients are above 0.9723.

Thereupon, the average was taken from the whole Area-Volume data set (in base-10 notation) and consequently transformed to log notation. Like the single reservoirs can be described well with a linear regression in log notation, also the log of their averages can be expressed well this way by the equation

$$\log Volume = 1.5814 * \log Area_{Jan/Feb\ 2002} - 2.7682 \quad (25)$$

with an R^2 of 0.9951. Referring back to Chapter 5.1.2, the equation nicely mirrors the expected relation (16).

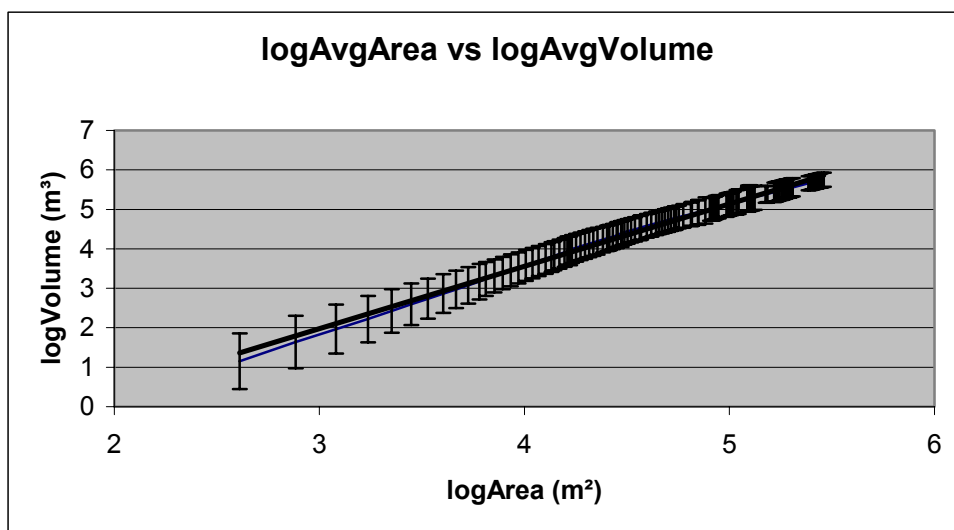


Figure 32: logArea-logVolume correlation.
The error bars indicate ± 1 standard deviation

However, it must be mentioned, that the comparison of the single reservoirs shows some variation. The error bars of ± 1 standard deviation plotted into the average diagram (Figure 32) indicate the range of variation. This reveals that the uncertainty increases with decreasing extent in area. Theoretically, the error bars would allow the interpretation that the each line representing a reservoir could seesaw between both extremes as indicated by the error bars. This, howsoever, is not the case. Rather, the range of ± 1 standard deviation gives a range, which is utilized by the multitude of linear trends. The important point to clarify is that the above described average (Figure 32), which matches the expectations well, is not a lucky hit

due to averaging a confused entirety but does give a sound representation of geometric consistency which is present in the data.

As each reservoirs $\log Area$ - $\log Volume$ relations can be expressed with a linear regression in the form $y = ax + b$ (see also Appendix 13), further evaluation of the variables a and b can give more insight.

Plotting a against b (Figure 33) already reveals the presence of regularities. The pairs of a and b arrange in a linear trend. It can be described well ($R^2 = 0.94$) with the expression

$$b = -4.1783*a + 3.8848 \quad (26).$$

With a correlation coefficient of -0.97 (see Appendix 13) a and b prove to be highly negatively correlated. As a and b define offset and slope of the reservoirs linear trends, the first important conclusion is that a confused distribution of a and b can be neglected.

Referring back to the equation expected from mathematical derivation of the Area-Volume relation (see equation 16 in Chapter 5.1.2), the variable a of the linear equation should be 1.5. It was shown that this figure is a result of explaining a three-dimensional body based on two-dimensional information. The term b represents geometric properties and a scale factor. A vague assumption is that the proven linear relation of a and b are an indicator for transition of geometries. Reservoir size dependency from the a and b interrelation could not be found.

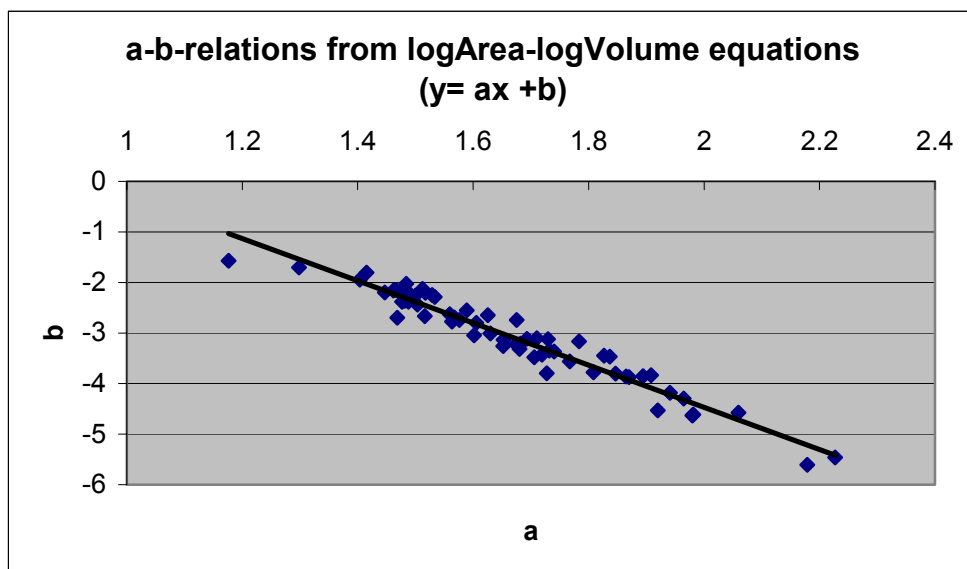


Figure 33: Distribution of a and b from the $\log Area$ - $\log Volume$ equations of the form $(y = ax + b)$.

The variables a and b are strongly correlated.

Summarizing the above, surface areas and volumes prove to be strongly correlated. The errors, as indicated by ± 1 standard deviation in Figure 32, prove to be largest for the smallest areas. Thus, the larger the reservoir surface is, the more robust its volume estimate with the general equation (25) will be.

5.2.3 Derivation of Depth-Volume-Curve

In analogy to the previously performed evaluation of Area-Volume-relations, the relations between depth and volume can be evaluated using the output data from the IDL routine.

Like the $\log Area$ - $\log Volume$ correlation, that between $\log Depth$ and $\log Volume$ can be described equally well with a linear regression (Figure 34). The R^2 s are all above 0.965 (compare with Appendix 14), and correlation coefficients are consistently above 0.9827 for the individual reservoirs. By taking the log of the averages of depth and volume, the overall relationship is described by the equation

$$\log Volume = 2.5184 * \log Depth + 3.7173 \quad (27)$$

with an overall R^2 of 0.99. Analogous to the $\log Area$ - $\log Volume$ relation, the errors become larger with decreasing depths. For greater depths, which, of course, are of greater importance and interest, the error becomes smaller. Thus, predicting reservoir volumes by their depth becomes more robust with increasing depth.

Trends between a and b of equation (27), as found in the previous paragraph, cannot be found (Appendix 14).

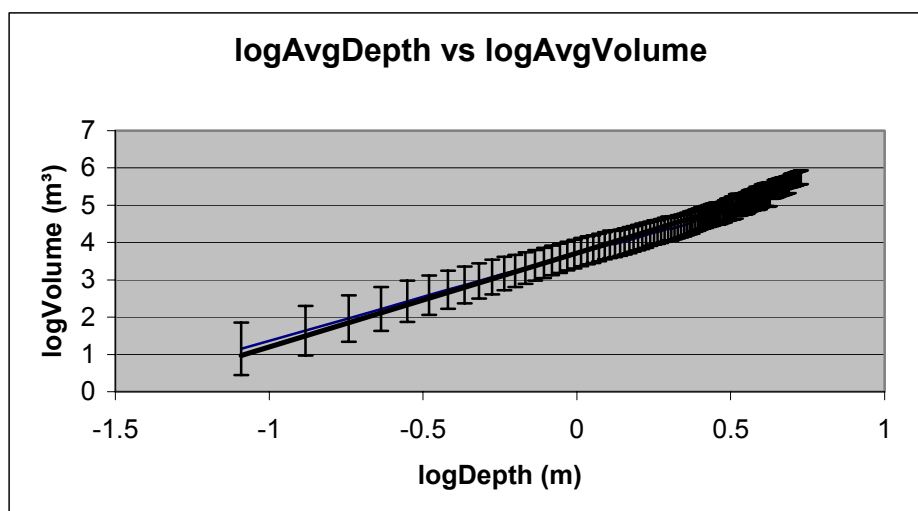


Figure 34: logDepth-logVolume correlation.
The error bars indicate ± 1 standard deviation

While the area-volume correlation is important to estimate reservoir storage volumes as acquired by means of Remote Sensing, the importance of good depth-volume correlation lies in its potential for the derivation of evaporation estimates.

5.2.4 Creation of a “Super-Reservoir”

This paragraph introduces the so-far disregarded part of the classified reservoirs, which were not visited in the field trip. With the previously described $\log Area\text{-}\log Volume$ (25) and $\log Depth\text{-}\log Volume$ (27) equations, the derivation of volume estimates will be shown. The final step is the creation of a ‘super reservoir’ which unites the geometric, and thereby the volume properties of all reservoirs. It can be described with one equation, which allows estimating water losses through evaporation in a simplified setup.

In some sections, the creation of the super-reservoir is difficult to follow. Steps are involved, where the chosen approach is not always obvious at first, but necessary to receive a super-reservoir that mirrors the desired properties. In order to guide the reader through the following procedures with greater ease, Figure 35 gives a brief overview of the steps involved in the

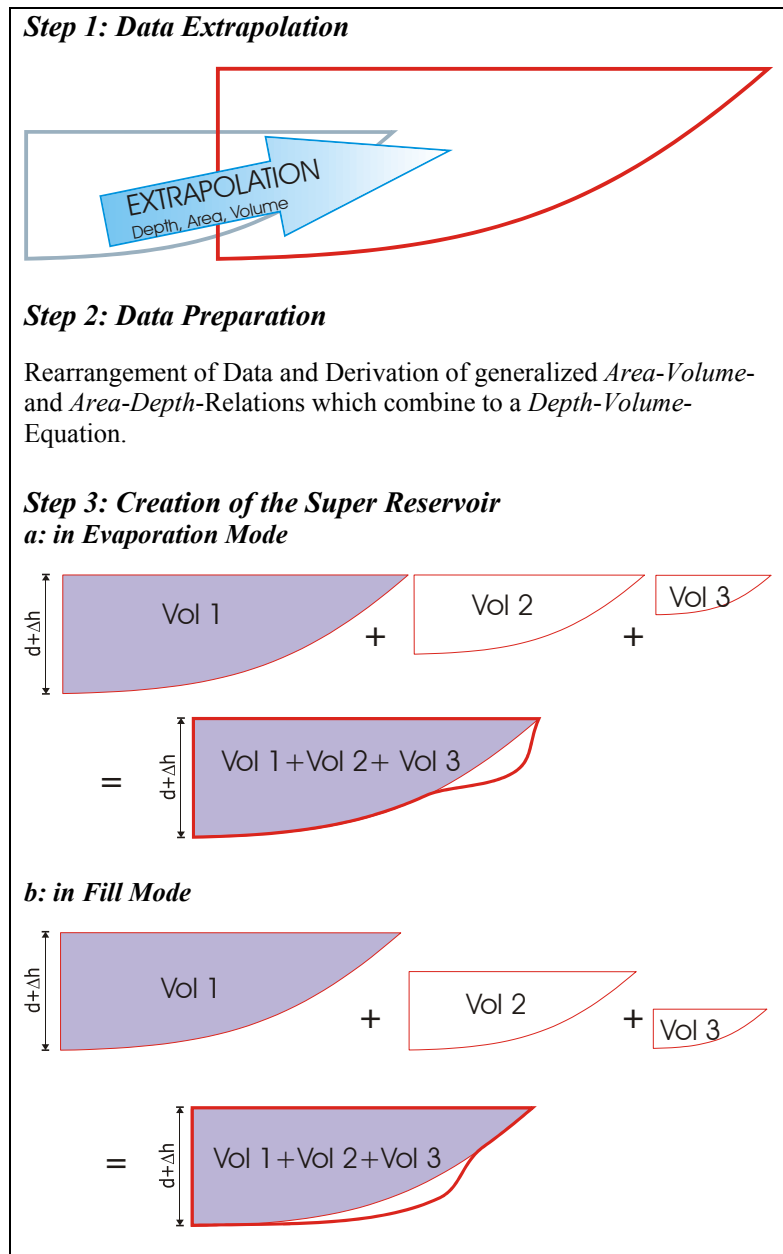


Figure 35: Creation of a Super-Reservoir.

To obtain a super-reservoir, reservoir data is extrapolated to the reference level of Nov. 1999 at equal depth steps (Step 1). Thereupon, the data is used to derive a depth-volume equation that allows deriving each reservoir’s volume distribution over its depth range (Step 2). The third step creates the super-reservoirs by adding the volumes at equal depth steps. By ‘top-aligning’ the reservoir data, the super-reservoir is calculated in evaporation mode (3a), whereas ‘bottom’ alignment yields the super-reservoir in fill mode (3b). The reference for top- or bottom- alignment is the depth $d+\Delta h$ of the deepest reservoir (blue shaded). The resulting super reservoir shows, at which depths the Volumes Vol 2 and Vol 3 (white) were added to Vol 1 (blue).

creation of the super reservoir.

In the first step, the reservoir data is extrapolated in a particular way, namely at equal area-steps, to match the area extent of November 1999. The extrapolated data is then used in the second step that seeks to derive a *Depth-Volume*-Equation, which is finally used in step 3 to calculate a super reservoir. The super reservoir can be created in two modes. By means of different data alignment these are the evaporation- and the fill-mode. The following describes these steps in detail.

Step 1: Having found strong correlations between the three variables area, depth and volume, their linear trends allow for extrapolation up to the known Δh_{max} (Figure 31), which was measured during the field trip at each reservoir. As Δh_{max} 's have to be seen as potential maxima, but with different 'spill return period designs' of the reservoirs, these levels should not be compared. As stated earlier, the results from satellite image classification are seen as a good approximation of the maximum fill that can be achieved in a very wet year. Since the satellite image is a snapshot of the state of the environment at a certain time, the comparison of remotely sensed area extent of reservoirs is feasible as they filled up under the same conditions. Rather than the comparison of the field data, where different water use patterns and water management account for inconsistent changes, the remotely sensed reservoir data qualifies as a reference level.

In order to minimize these effects, the reservoir data is extrapolated to the reference level of Nov. 1999. Known for each measured reservoir are the

1. *area, depth, volume, and Δh_{max} for the time of the field trip (Jan/Feb 2002), and*
2. *the change of area and volume for different depth-steps of 5 cm below the Jan/Feb 2002-level from the output created with the IDL routine.*

Using the information stated second in the above listed, equations for $\log Area$ - $\log Volume$ -, $\log Area$ - $\log Depth$ -, and $\log Depth$ - $\log Volume$ -relations can be derived for each measured reservoir. As depth d and Δh_{max} is known, the depth can be extrapolated in steps of 5cm until Δh_{max} is reached. Taking the log of the extended depth steps then allows its use in combination with the $\log Area$ and $\log Volume$ data, which is the extrapolation of $\log Area$ and $\log Volume$ for all steps in the range of $\log Depth_{d+\Delta h_{max}}$. Therefore, each reservoirs $\log Depth$ - $\log Area$ and $\log Depth$ - $\log Volume$ data were extrapolated based on their linear regressions.

The screenshot below (Figure 36) clarifies the above with real data. Left of the dashed vertical line is the reservoir data that is known from field measurements. The previous two chapters

explained how the data was derived for the different depth steps by means of the IDL routine. To the right of the dashed line we find the extrapolation field with yellow shading. All known values, which are all of those left of the dashed line but also $\log d + \log \Delta h_{max}$ and $\log Area_{Sat}$ to its right, are scripted in italics. The extrapolation makes use of all the known data. The data left of the dashed line is used to derive the regressions the data is extrapolated with.

Depicted in data-line 1 are the log of a reservoir's depth steps. From the known maximum depth d (blue framed field), the depths are extended in log 5 cm steps up to $d + \Delta h_{max}$, which is

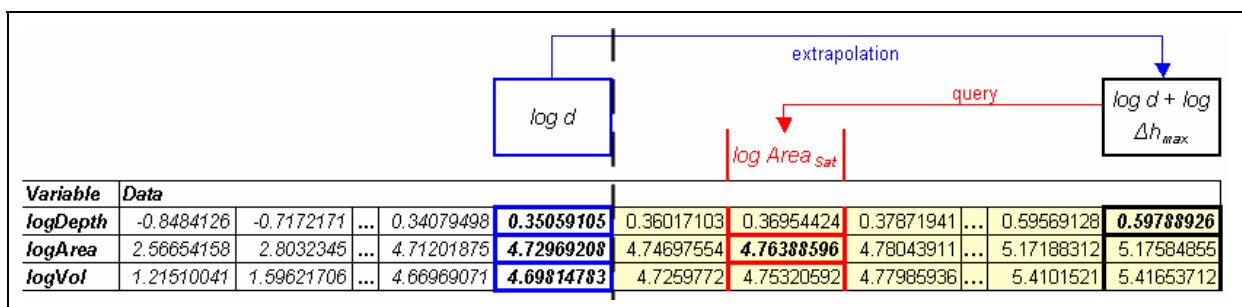


Figure 36: Data Extrapolation of field measurements to maximum dimensions (defined by spillway, $d + \Delta h_{max}$) and derivation of reservoir dimensions for Nov. 1999.

1. Depth was extrapolated in Steps of 5 cm to Δh_{max} , and thereof taken the logarithm
2. Using \logDepth - \logArea -regression, \logAreas were extrapolated for the depth steps. Accordingly, \logVolumes were extrapolated with their \logDepth - \logVolume -regression.
3. Querying the \logArea filed for the known $Area_{Sat}$, \logVolume and \logDepth can be derived

Bold-Italics are references known from measurements; the yellow shaded part to the right resembles extrapolated data.

also know. Based on the linear regressions of the measured data (left of the dashed line) for \logDepth - \logArea -, and \logDepth - \logVolume -relations (see Appendices 15 and 16), these fields can be extrapolated to the corresponding $\log d + \log \Delta h_{max}$ field in depth-steps of log 5 cm, as it is indicated by the blue arrow. Another known value is the $Area_{Nov1999}$ of the reservoir in Nov 1999 from the satellite image classification (Figure 31). Querying for its logarithm in data-line two (red arrow to bold-italic value in red framed cell in Figure 36), allows the derivation of the corresponding \logDepth and the \logVolume in the fields above and below $\log Area_{Nov1999}$, which are expected to represent maximum reservoir dimensions.

In order to visualize the data extrapolation further, the three framed columns in Figure 36 may be compared with Figure 31, where they resemble the different reservoir levels depicted in respective colors.

This procedure was implemented for all 61 measured reservoirs. The resulting table thus yields each reservoir's areas and volumes for all depth steps of 5 cm, starting from its expected dimensions in Nov 1999.

Extrapolation of data upon idealized assumptions is feasible in cases such as this; however, it is liable to introduce an error. It might thus be possible, that the depths and volumes derived from the extrapolation table (see red framed cells in Figure 36) are overestimated. This is the case when, for example, in reality the slope angle of a reservoir changes (reservoir depicted in blue in Figure 37) above the measured level (Area of Field Data in Jan/Feb 2002 and associated depth measurement d). As the expected depths and volumes for the 1999-level are derived by linear extrapolation of field-measured areas (depicted in red) until the extrapolated area matches that of the remotely sensed area (depicted in blue), the accordingly extrapolated depths ($d +$ derived Δh) and volumes might be overestimated by not taking into account this angular change. Underestimation, in contrast, is less likely, as increasing concavity in the upper range of a reservoir's slope is unlikely in a gently undulating topography as in the Upper East Region.

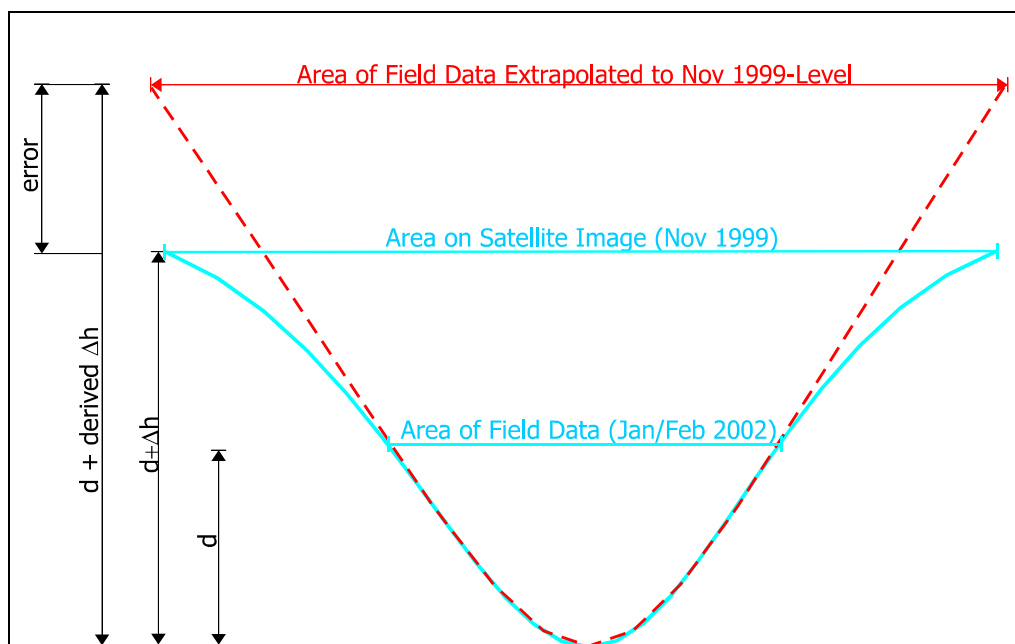


Figure 37: Possible source of error in depth derivation by surface area.

A possible source of error is the overestimation of depths by using a generalized Area-Depth regression. Therewith, the depth of a reservoir is derived for equal areas. Where, in reality, the side slopes of a reservoir are convex the desired area is associated with a shallower depth than those achieved by linear interpolation. As shown above in red, the $d +$ derived Δh contains an additive error. The order of error arising from the interpolation is not known. Underestimation of depths is least expected as concavely shaped upper slopes are unlikely to occur.

Step 2: The next step in the creation of the “super reservoir” is the re-arrangement of the data in order to achieve applicability for the satellite imagery. This is the conversion from areas and volumes for different depth steps to volumes and depths for different area steps. Based on

the above-described extrapolation, one average $\log Area$ - $\log Vol$ and $\log Area$ - $\log Depth$ equation was derived to be applied to the yet unused reservoir area data.

Focusing on the $\log Area$ - $\log Volume$ correlation, a mean volume is sought for each area-step. This is achieved by averaging the volumes of corresponding area-steps in base-10 notation (Figure 38). With an R^2 of 0.9983, the generalized Area-Volume-regression to be used for volume estimation upon remotely sensed reservoir areas can be described as:

$$Volume = 0.0122 * Area^{1.3952} \quad (28).$$

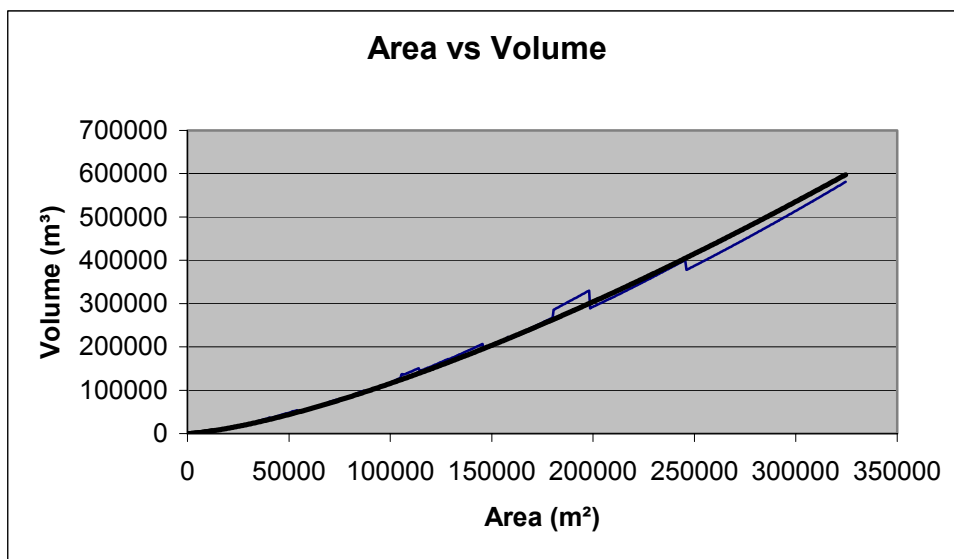


Figure 38: Area-Volume relation based on reservoir data extrapolated to 1999 level.
The area-volume relation can be described with a potential trend.

The relation of the variables a and b of each reservoir's $\log Area$ - $\log Volume$ -regression is similar to the relation that was found in Chapter 5.2.2 (see Appendix 17). With a coefficient of correlation of -0.96 between all a 's and b 's, and a standard deviation of 0.154 (a 's) and 0.518 (b 's) respectively, they are highly negatively correlated.

Accordingly, the creation of a generalized $\log Area$ - $\log Depth$ -regression resulted from reorganizing the data, converting to normal notation and then averaging depths of corresponding areas. This $Area$ - $averageDepth$ relation (Figure 39) is finally represented by the equation:

$$averageDepth = 0.0241 * Area^{0.4234} \quad (25)$$

With an R^2 of 0.9631 and a coefficient of correlation of 0.92, reservoir surface areas can adequately describe reservoir depths.

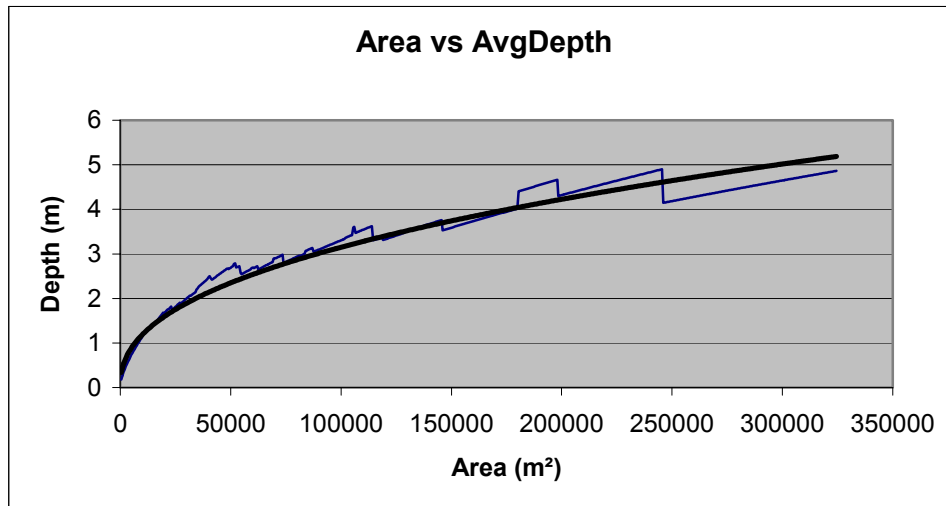


Figure 39: *Area-averageDepth*-relation based on reservoir data extrapolated to 1999 level.

The *Area-averageDepth* curve is also known as hypsographic curve. It fits with a potential trend. The breaks in the upper range of the graph are due to the small remaining number of reservoirs that make up the average depth. As one falls out of the averaging, the breaks occur. The cause is the larger difference in average depths between “large” reservoirs, in contrast to “small” reservoirs that show a lower order of fluctuation.

A noticeable feature of the generalized reservoir curve depicted in Figure 39 are the sharp breaks, which mainly occur in the tail part of the curve. They go back to the decreasing number of reservoirs that are part of the averaging. A break-off reflects the level, where a comparably deep reservoir falls out of the averaging. The most distinctive of these breaks, which occurs at an area extent of ca. 250,000 m², marks the stage where the segment to the left represents the average out of two reservoirs, whereas to the right of the break only one reservoir is left.

As seen before with the $\log Area$ - $\log Volume$ relations, also the a 's and b 's of $\log Area$ - $\log Depth$ are highly negatively correlated. Their coefficient of correlation between all a 's and b 's is -0.96, with a standard deviation of 0.184 (a 's) and 0.819 (b 's) respectively. The respective variables a and b for each reservoirs $\log Area$ - $\log Depth$ -regression are listed in Appendix 18.

The application of *Area-Volume*- and *Area-Depth*-relations to the field data finally yields the input data for the creation of the super reservoir. Now knowing each reservoir's area, volume and depth for the level of 1999, only their diminishment, or miniaturization, needs further evaluation. Referring back to Figure 31, the evaluation aims at finding a solution to describe

the interplay of the three parameters area, depth, and volume at any level below the ‘surface 1999’.

The last generalized equation necessary for the creation of a super reservoir is the *Depth-Volume*-relation. By combining the information from *Area-Volume* and *Area-Depth* into *Depth-Volume* (Figure 40), the equation

$$Volume_{Extrapolated} = 2618.1 * Depth_{Extrapolated}^{3.2952} \quad (30)$$

reflects their relation.

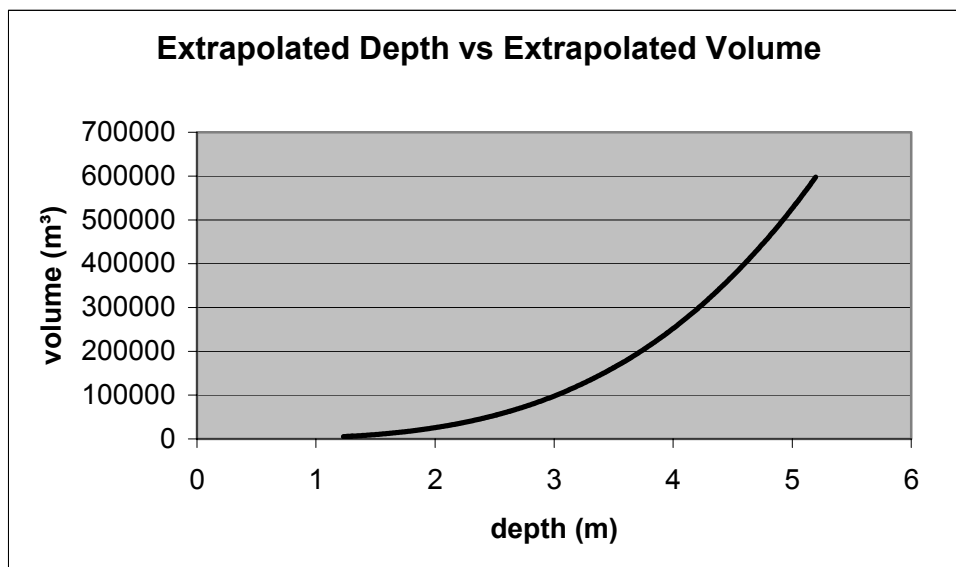


Figure 40: Depth-Volume curve from extrapolated data.

Described by the potential trend, different depth steps can be associated with volumes. The curve is based on reservoir data extrapolated to the Nov. 1999 reference level.

With this equation (30), each reservoir’s volume can be derived as a function of its depth – the most important step in the creation of the super reservoir.

Having found and described a large number of relationships between area, depth, and volumes for measured, extrapolated and derived levels, but with changing reference variables, a short interim summary may improve comprehensibility for the further: Using the 3D-models, which were computed from the field data, each reservoir’s areas and volumes were calculated for all *depth step* of 5 cm. This had to be transformed into equations that describe depth and volume for different *area steps*. Upon the derivation of reservoirs dimensions at Nov. 1999 level, the reference variable is changed back to *equal depth steps* for the creation of the “super reservoirs”. In these super reservoirs, the consideration of surface areas is not necessary.

Step 3: The creation of the super reservoir incorporates each reservoir's depth, and its volume distribution for each depth step of 5 cm. Upon deriving volumes (28) and depths (29) for each of the remotely sensed reservoir surface areas, the depth-volume equation (30) is utilized to derive the above describe distribution of volumes over their depth steps. Described more pictorially, each reservoir's model would then consist of 5 cm thick slices or layers that lie on top of each other, as an imagined reservoir model carved out of a deck of cards. The volume of each of the slices is known due to the $Depth_{Extrapolated}-Volume_{Extrapolated}$ -equation (30).

The derivation of each reservoir's volume distribution over its depth range finally laid the foundations for the creation of the super reservoir. By means of different data arrangement, this super reservoir can have two different characteristics. The mode that is of interest for the calculation of evaporation losses, herein referred to as evaporation reservoir, first "surface aligns" all separate volume slices of each reservoir and then takes the sum of volumes for each depth step (3a in Figure 35). The reason therefore is, that evaporation occurs from the surface of a reservoir, no matter how deep it is. Merging reservoirs of different depths therefore requires the top alignment to correctly represent the amounts of water contained in all depth steps. Cumulating the sum of the volume slices upwards from the bottom yields the super reservoir for the evaporation mode. Depicted in Figure 41 is the evaporation reservoir, and a second curve, which give information on the number of reservoirs that are included in the creation of the super reservoir at the various depth steps. Indicated by the plateau to the left, up to the depth of 1.20 m all reservoirs are included in the creation of the super reservoir. At depths greater than 1.20 m, the "volume-slices" are then continuously made up from a fewer number of reservoirs. Explained in other words, as a deeper reservoir consists of more 5cm thick volume slices than a shallow reservoir, deep reservoirs contribute to the volume calculation over a greater depth range than shallower ones. As soon as the super reservoir's depth falls below the maximum depth of any input reservoir, it drops out of the calculation due to the surface alignment of the volume slices. The drop at 1.20 m thus marks the point, where the smallest of the evaluated reservoirs would fall dry.

The super reservoir is 5.15 m deep and contains 185.3 million m³ of water. In order to describe the distribution of volumes over the depth range (d) with an equation, the cumulative curve was fitted with a 4th order polynomial, so the super-reservoir's volume in evaporation mode ($Vol_{EvapMode}$) is described as

$$Vol_{EvapMode} = 1.2933*d^4 - 8.5768*d^3 + 19.809*d^2 - 16.426*d + 3.2136 \quad (31).$$

The high R^2 of 0.9995 (coefficient of correlation 0.9997) merely indicates a good accordance between the data distribution and the polynomial equation, which is not surprising with a polynomial of 4th order.

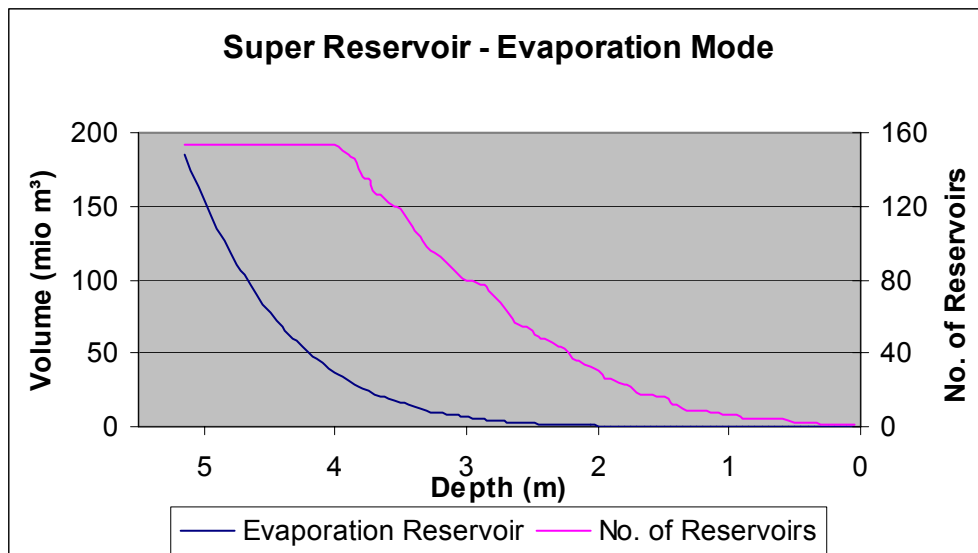


Figure 41: Super Reservoir in evaporation-mode.
 Calculated from the depth distribution of each reservoirs volume is the cumulated volume curve in evaporation mode. The super reservoir represents the full storage capacity of reservoirs in the Upper East Region of Ghana in one reservoir. The curve above describes the distribution of the total volume of 185.3 Mio m³ of stored water over the depth range of 5.15 m. The thin red line gives information about the number of reservoirs that are included in the calculation of volumes for all depth steps.

The second kind of super reservoir is referred to as a fill-reservoir. In contrast to the alignment in the evaporation reservoir, each reservoirs “volume slices” are bottom aligned in the fill reservoir before adding up the volumes of each depth step. Bottom alignment is required because reservoirs, like every other depression, fill from the bottom. Figure 42 clarifies this difference with the fill reservoirs’ depth-‘cumulated sum of volumes’-curve increasing along with depth rather than falling, as it is the case of the evaporation reservoir. Also depicted is the number of reservoirs that account for the volumes over the depth range. According to this, the first reservoirs fall out of consideration before significant volumes are achieved. Such as done before, a polynomial was fitted to the data in order to obtain an equation. With an R^2 of 0.9988 the fill reservoir’s volume ($Vol_{FillMode}$) is represented by the 4th order polynomial

$$Vol_{FillMode} = -0.6678*d^4 + 2.3584*d^3 + 16.801*d^2 - 24.276*d + 5.8659 \quad (32).$$

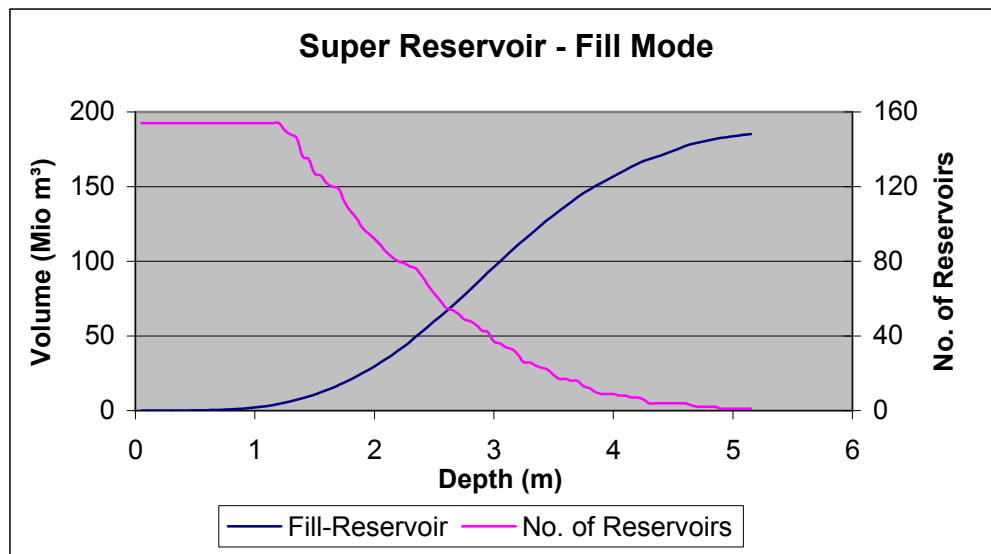


Figure 42: Super Reservoir in fill-mode.

By means of “bottom-aligning” the depth-volume input data, the Super Reservoir converts into the fill-mode, the counterpart to evaporation-mode. Starting from empty reservoirs, the curve above describes the distribution volume accumulation over the depth range of 5.15 m due to inflow. The thin red line gives information about the number of reservoirs that are included in the calculation of volumes for all depth steps. Where the line drops, the first reservoirs drop out of the fill-mode as they spill. The modifying fact that small reservoirs also have smaller catchments and thus fill slower is disregarded due to the lack of necessary data.

In contrast to the subsequently used evaporation reservoir, the fill-mode super-reservoir is shown for complementary reasons. It shows the fill-pattern starting from empty reservoirs, which is rather unnatural. More important than depicting the precise fill-properties of the Upper East’s reservoirs in reality, is the method that is used to derive it, as the data alignment to create it can be adjusted to any given start condition.

5.3 Evaporation losses from the Super Reservoir

CHOW identified “evaporation from free-water surfaces, ranging from small farm ponds to irrigation channels and large reservoirs, [...as] a major factor in reducing water storage in arid and semiarid regions” (1964, p. 24 - 17). In the following, the order of these water losses are estimated upon the above-created super reservoir in evaporation mode, which is expressed in terms of equation (31), and evaporation data. Chapter 3.1 explained that the actual evaporation E_a from open surface water bodies equals the potential evaporation E_p as they resemble saturated surfaces. Besides the theory behind evaporation calculation after Penman, also the computation of monthly potential evaporation (E_p in mm/day) with CRU data was briefly elucidated. The following describes the extraction of potential evaporation data for the

Upper East Region from the CRU-based evaporation dataset for West Africa and the calculation of evaporation losses from the super reservoir.

The Upper East Region occupies five 0.5° cells to a considerable extent of which the monthly evaporation was extracted for a ten-year period from 1986 until 1995, the end of the CRU climatology. The Upper East Region marginally covers further five 0.5° cells, however, the area they cover is minimal and there are no reservoirs in the area they cover. Thus they were not included in the average.

Depicted in Figure 43 is the average potential evaporation (mm/day) of each month's five E_p -cell values, as well as their minimum and maximum values to indicate the total range. Used in the following is the averaged monthly evaporation data, which sums up to an average yearly total of 1881 mm. For comparison, Figure 43 also depicts the daily potential Evapotranspiration (E_o in mm/day) recorded at the Meteorological Station in Navrongo. The data was calculated from long-term climatic data (1961-1990), which coincides best with the maximum potential evaporation values as derived from the CRU data set, and sums up to an average yearly total of 2050 mm. Navrongo's annual potential evaporation is thus 169 mm higher than the ten-year annual average calculated the five CRU cell values. The largest difference between these two data sets occurs in the rainy season.

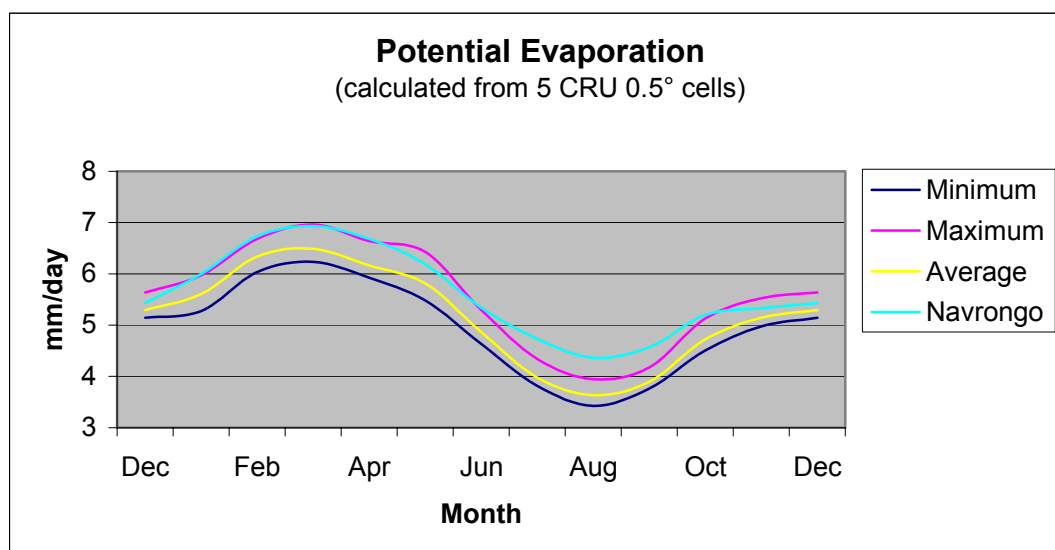


Figure 43: Decadal (1986-1995) monthly averages of Potential Evaporation.

The Upper East Region occupies five 0.5° cells. The diagram shows the average potential evaporation as well as the minimum and maximum potential evaporation values of the five cells. For comparison, the monthly potential evaporation is also depicted for the meteorological station in Navrongo (1961-1990).

Combining the super reservoir's equation (31) with the decadal monthly evaporation data (in mm/day) finally enables the calculation of evaporation losses. As the reservoirs were all extrapolated to the level of 7th November 1999 (Chapter 5.2), the start date for evaporation calculation was also set to a 7th November²¹. Multiplying the number of days per month with the CRU-based monthly potential evaporation (mm/day) returns the total monthly evaporation referenced to the last day of a month, which was converted to m per month (or part of the month in November). Upon cumulating of the monthly evaporation losses, their subtraction from the super-reservoir's maximum depth of 5.15 m yields the change in depth over time, from the start date onward. Knowing the derived depths at the end of each month then allows calculating the available water volumes and the amount of water losses by implementing the super reservoir's depth-volume equation (31).

Figure 44 depicts the above-described calculation. Starting with a total volume of 185.3 Mio m³, the evaporation losses (pink line) cause the amount of water stored in reservoirs (blue line) throughout the Upper East region to reduce constantly. By the end of February, 56 % of the water has already evaporated. The yellow line with the triangular ticks illustrates the number of reservoirs that make up the volume of the super reservoir at all depth and time

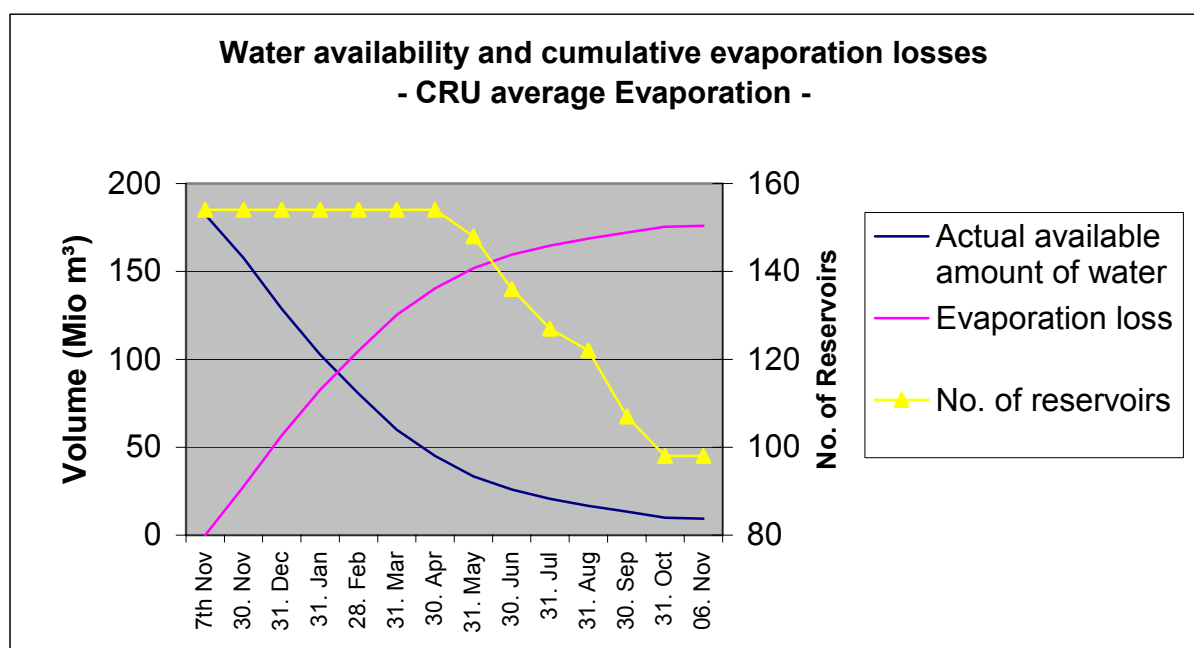


Figure 44: Estimation of Evaporation losses from the Super Reservoir.

Based on decadal monthly potential Evaporation E_p , evaporation losses from the super reservoir were calculated. Depicted in pink are the cumulative water losses. The blue line represents the volume of water that is stored in reservoirs (1-35 ha) throughout the Upper East Region at different times of the year. The Super Reservoir's start volume is 185 Mio m³ (7th Nov) which decreases to an end volume of 9.3 Mio m³ (6th Nov). The yellow line with triangular ticks diagrams the number of dams that contain the corresponding volume at a given time. According to this, the first reservoirs fall dry in May.

²¹ The true potential maximum fill of reservoirs is likely to be earlier than the 7th November, but this date is yet the best reference of maximum fill levels achieved in a comparably wet year.

steps. The reduction from its plateau (154 reservoirs) means that reservoirs dry up and thus fall out of the volume calculations. Figure 44 shows, that the first reservoirs fall dry in May. By the 6th November, the number of water holding reservoirs has decreased to 98.

Depicted in Figure 45 is a variation of the above diagram. Instead of ten-year monthly averages, it uses the ten-year monthly maximum potential evaporation value out of the five CRU cells for a ‘worst-case’ estimation. According to this, the first reservoirs also fall dry in May. The rate at which the reservoirs fall dry from then on is yet higher. By the 6th November, the worst-case estimation ends with a volume of 6.9 Mio m³ that is stored in 85 remaining reservoirs, compared to 9.3 Mio m³ in 98 reservoirs of the average based estimation.

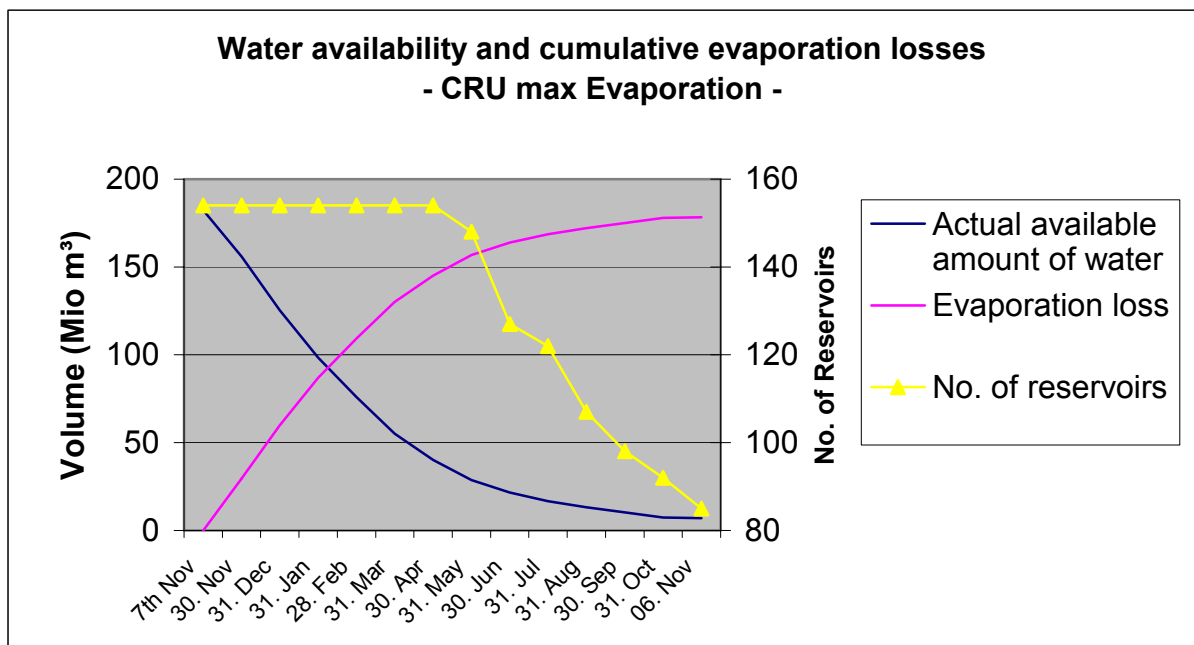


Figure 45: Worst-case Estimation of Evaporation losses from the Super Reservoir.

In contrast to Figure 34, the above depicted worst-case estimation of evaporation losses is based on the decadal monthly maximum of the five CRU-cells. The Super Reservoir's end volume of 6.9 Mio m³ (6th Nov). The yellow line with triangular ticks shows the number of reservoirs that contain the corresponding volume at a given time. According to the worst case scenario, the first reservoirs also fall dry in May, but the rate at which the reservoirs subsequently fall dry is higher.

An important point to make clear is that the above diagrams only take into account evaporation losses from the reservoir. In addition, seepage (groundwater recharge), draft for irrigation, and other uses reduce the available volumes simultaneously, which yet represent productive *uses* in contrast to the unproductive evaporation *losses*. Nevertheless, these influencing factors modify the above graph and, e.g. cause the first reservoirs to fall dry at earlier stages and at an explicitly higher rate than through sheer evaporation losses. Likewise neglected is the inflow of runoff during the evaporation period, which counteracts the volume

reduction. In accordance with Upper East's climate (Chapter 2), the influence of inflow gains importance only from July onwards.

5.4 Outlook

Having found a number of relations between area, depth and volume that can be made use of in various ways, an outlook can be given concerning the use of the data, but also with regard to technical improvements.

Probable uses of the found relationships are manifold. Of importance to the people in the Upper East Region is the evaluation of reservoir development potential and the irrigation potential that can be made use of to improve their economic situation. As explained before, agricultural activities are the backbone of the Upper East's rural society and are furthermore seen as the most promising sector for economic development. Having visited a large number of reservoirs throughout the Upper East Region, it became clear that the revenue from growing tomatoes, onions, and rice as cash crops is vital. This impression is backed by the Ghana Living Standard Survey that identified the Upper East's mean annual household income and per capita to vastly depend on agricultural production (64 % of total income), which often is the only source of monetary income to a large proportion of the population. Of likewise high importance is the agricultural production for the food supply of the local population (after ASENSO-OKYERE et al. pp. 73, 104). Furthermore, the economic value of water can be assessed, based on the different demands of the various crop types.

Besides the socio-economic values, the findings can also help to improve environmental modeling (in its widest sense). The storage volumes and surface areas can e.g. help to improve and regionalize runoff-, climate-, and land use/land cover-change modeling that yet, if at all, took into account reservoir water storage throughout a landscape in terms of a parameterized representation only. For a (Volta-) basin-wide evaluation of the evaporation losses, the data can e.g. help to improve and validate the precipitation recycling ratio (VAN DE GIESEN et al. 2002, p. 159) within the Volta basin, that expresses the contribution of locally evapo(transpi)rated water to the amount of rainfall within the basin. Thus, the atmospheric water budgets of incoming humidity, locally evaporated and evapotranspired water, and outgoing humidity may be assessed with greater precision.

As elevation and drainage data becomes available that is more precise, the reservoirs can also be included in node-link networks (modeling software such as WEAP), taking into account each reservoir's own depth-volume equations and catchment. It could be used to evaluate potential sites of reservoir constructions that make use of excess runoff, but do not affect

downstream reservoirs. The integration of this data within such a network becomes especially interesting, when introducing the fourth dimension. The fill and depletion of reservoirs could be modeled for different times and different rainfall and evaporation conditions. After subtracting the evaporation losses, the remaining irrigation potential could be derived for each time of the year, and in combination with crop water requirements, resource management, risk-assessment for different crop-types and famine early warning can be possible.

The second branch of the outlook aims at further improvements in the volume-by-area estimation. So far, the relations between the three involved variables area, volume and depth referred to dimensions and aspect ratios as derived from a triangle-based pyramid. Although the average of all reservoirs closely resemble the expectations that were based on such a simplified shape, a more precise representation of reality is expected to be achieved by introducing the flexion of the shoreline and the reservoir basin shapes. This improvement is mainly of importance when including each reservoir in a node-link network as described above. Plotted in Figure 46 is the length of a reservoir against half its width at the dam wall. The flexion of the depicted curves are calculated from the term

$$y = (1 - x^p)^{1/p} \tag{33}$$

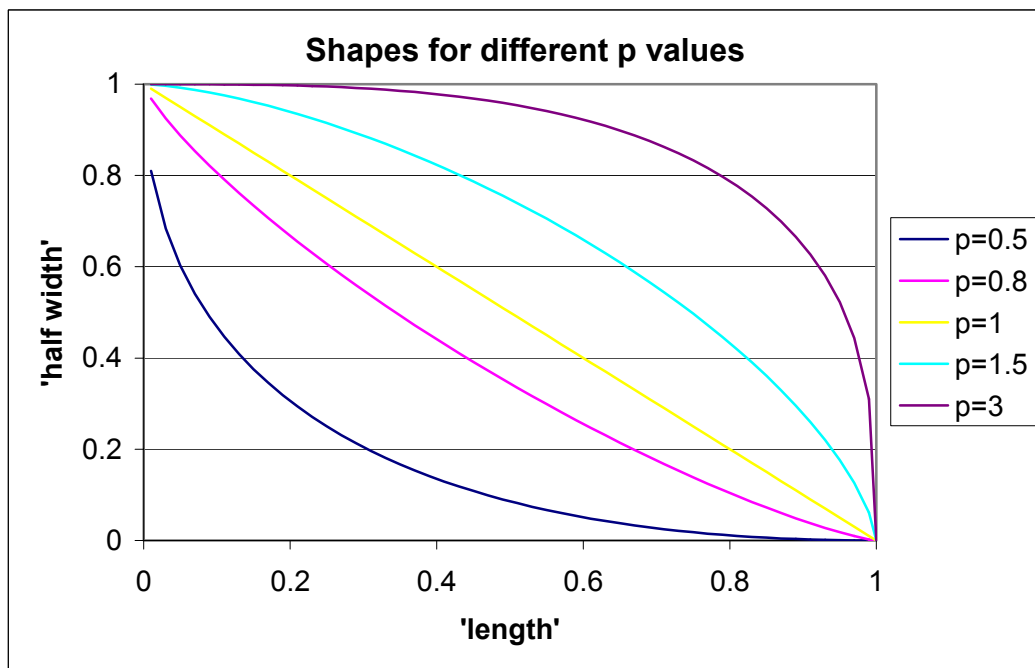


Figure 46: Reservoir shapes regarding their flexion.

By changing the factor p , the flexion of the reservoir shores can be adjusted. For $p = 1$ the reservoir shows a triangular shape, p 's < 1 indicate concave shorelines in relation to the length axis, whereas p 's > 1 represent convex shapes. (unitless).

Mirroring these curves along the x-axis gives the surface shape with respect to the curvature, e.g. for $p=1$ we get a familiar triangular shape, lower p -values cause concave shorelines such as the end of a trumpet, whereas p -values above 1 represent convex shorelines.

Information on the length and width of reservoirs are expected to be derivable by introducing a method such as described by SAGAR/GANDHI/RAO (1995). According to their approach, a centroid is derived for every reservoir, which is used to compute the largest possible incircle as well as the smallest encircle (Figure 47). The radii of each reservoirs in- and encircle can be related in terms of a length-width ratio, that can be introduced in the above described flexion calculation.

Furthermore, circularity-, elongation-, and thinness-ratios can be calculated from the circles.

Besides mirroring the different curves along the x-axis (Figure 46), they can also be rotated around the x-axis by half a revolution to then not only describe the flexion of the shoreline, but also of that of the basin itself. As the depth of reservoirs is (in this study) always less than half the

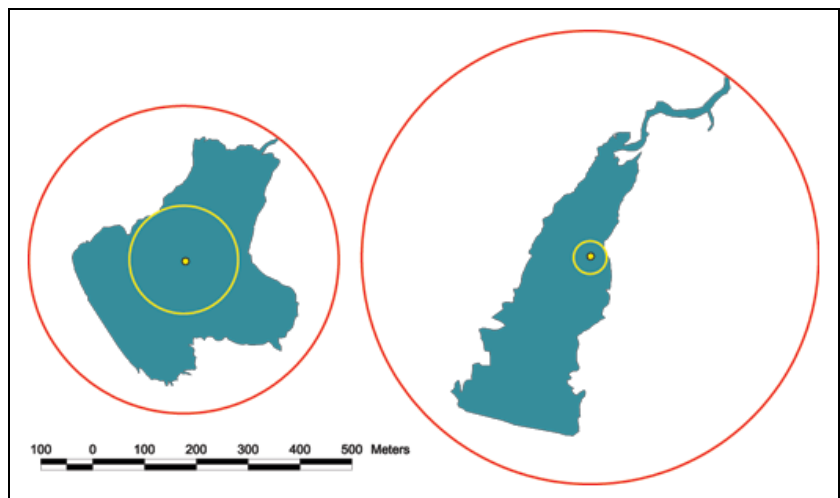


Figure 47: Relation of in- and encircle dimensions for different reservoir shapes.

Depicted to the left is a reservoir (ID 59) with a surface area of 11.49 ha that has a low length-width ratio. In contrast, reservoir 101 to the right, which clearly has a greater length-width ratio. After SAGAR et al. (1999) these relationships are best described through the largest incircle and the smallest encircle around a centroid.

width, a z-axis different from the y-axis were to be introduced (compare with equation 10), which would result in an elliptic rotation of the above depicted curves around the x-axis. Such an elliptic rotation body that takes into account the flexion of a reservoirs outlines is expected to give an even more precise representation of each reservoirs true shape and volume, and may also clarify the strongly negative correlated a 's and b 's of the Area-Volume equations (Figure 33 and equation 26).

An interesting task to look at is the transferability of the gathered information and relationships to other areas. This would enable the derivation of reservoir storage volumes for large areas, just on the basis of classifying reservoir surface areas by means of remote sensing. In order to account for the topographic properties as they occur in other regions, variables should be evaluated that are capable of scaling the area-volume and area-depth relations to the local occurrence. Better elevation data was therefore desirable.

Chapter 6

Conclusion

Water is a scarce and valuable good in semi-arid regions, and the retention of water in reservoirs is an important tool to extend its availability over time. Especially in areas as the Upper East Region of Ghana, where the population is comparably poor and increased agricultural production is seen as the primary opportunity of economic development, further reservoirs are needed. Where water is scarce, its efficient use needs to be the primary guideline in water related planning. Also, the planning of dams needs thorough evaluation to achieve sound water use efficiency. The location and dimensions of planned reservoirs have an influence on already existing reservoirs, which has to be taken into account to avoid negative effects. The present lack of baseline data hinders proper decision making in this respect. Collection and evaluation of such baseline data was the objective of this study.

The aim of this study was to determine reservoir storage volumes in the Upper East Region of Ghana and to estimate the evaporation losses that occur from their surfaces. In order to make volume estimates for a large number of small reservoirs that are spread throughout the Upper East Region, the study combined two kinds of data. These are satellite images and data from reservoir field measurements. The Landsat ETM+ satellite images were used to conduct an up-to-date inventory of reservoirs. As satellite remote sensing may only give information on the extent of the surface area of reservoirs, a randomly selected set of 61 reservoirs was extensively measured during field trips. The field data served to find a function that allows the estimation of reservoir volumes by means of their remotely sensed surface areas. In the analysis of the reservoir measurements, the three attributes 'area', 'depth', and 'volume' were used to evaluate relations of the combinations area-volume, area-depth, and depth-volume. Due to the relatively similar geometric properties of the reservoirs, interrelations between these variables could be adequately described in terms of simple equations.

The possible uses of the dataset are manifold. In order to give an example, unproductive water losses were estimated that occur in terms of evaporation directly from the reservoir surfaces. Based on the evaluated relationships between area, depth, and volume, the reservoir data was therefore aggregated into a “super reservoir” that unites and resembles all of the Upper East’s reservoirs properties. Using ten-year averages of monthly evaporation data, the evaporation loss from the super-reservoir were estimated. In the course of a year, the evaporation losses sum up to a total of 175.7 Mio m³ (or 0.1757 km³), a figure that appears very small compared to the mean annual evaporation losses from Lake Volta, that are estimated at 10.2 km³ (ANDREINEI et al. 2000, p. 16). In relation to the Upper East Regions’ total reservoir storage capacity that was estimated at 185 Mio m³, this amount of water loss is very high.

A full reservoir volume simulation model that takes into account additional water storage reduction through seepage, percolation, or withdrawal was beyond the scope of this thesis. Nevertheless, the results of this study may substitute the unknown ‘storage’ in the water balance for the Upper East Region and contribute to further reservoir related research. The reduction of volumes through evaporation can be observed throughout the year, yielding information that may be of use for efficient water use management or the selection of crops to cultivate that can securely be produced with the given resources.

The impact assessment of dam construction, however, also has to take into account increasing evapotranspiration from the adjacent developing irrigation and gardening schemes. Subtracting the evapotranspiration from the primary land cover, the surplus in evaporation from reservoirs and evapotranspiration from irrigation schemes resemble man-induced changes. The effects of these changes in land use, surface hydrology and atmospheric feedback would need to be evaluated more closely for a complete impact assessment.

Yet, the important point is that the reservoirs supply the poorest population of Ghana with up to 185 Mio m³ of water every year for irrigation, livestock and fishing, and to use it for household and hygienic purposes. Studies like the one presented here may help safeguard continued social benefits of this technology while preventing over-exploitation of the scarce water resources.

Literature

- ACHEAMPONG, P. K. (1988): Water Balance Analysis for Ghana. In: *Geography* (73), pp. 125-131.
- ALFÖLDI, T. (1982): Remote sensing for water quality monitoring. In: JOHANNSEN, C. J./ SANDERS, J. L. (eds.)(1982): *Remote Sensing for Resource management*. Soil Conservation Society of America. Iowa.
- ANDAH, W. E. I. (1992): Optimisation of Irrigation Water Use at the Tono Irrigation Project in Ghana. Case Study. 9th International Advanced Course on Water Resource Management. Water Resources Research and Documentation Center (WARREDOC). Italian University for Foreigners. Perugia.
- ANDREINI, M./VAN DE GIESEN, N./VAN EDIG, A./FOSU, M./ANDAH, W. (2000): Volta Basin Water Balance. ZEF-Discussion Papers on Development Policy. No. 21. ZEF. Bonn.
- ASENSO-OKYERE, W. K./TWUM-BAAH, K. A./KASANGA, A./ANUM, J./PÖRTNER, C. (2000): Ghana Living Standards Survey. Report of the Fourth Round (GLSS 4). Ghana Statistical Service. Accra.
- BALSER, A. W. (1996): Combining Landsat TM and Multi-Temporal ERS-1 Imagery to Improve Classification Accuracy and Detail in the Tanana Flats Wetlands Complex, Interior Alaska. (M. S. Thesis, University of Alaska, Fairbanks. Unpublished).
- BAUMGARTNER, A. (1996): Verdunstung. In: BAUMGARTNER, A./LIEBSCHER, H.-J. (1996): *Allgemeine Hydrologie – Quantitative Hydrologie*. Lehrbuch der Hydrologie, Band 1. 2nd Edition. pp. 334-379. Bornetraeger. Berlin.
- BELWARD, A. S. (1991): Spectral Characteristics of Vegetation, Soil and Water in the Visible, Near-Infrared and Middle-Infrared Wavelengths. In: BELWARD, A. S./VALENZUELA, C. R. (ed.)(1991): *Remote Sensing and Geographical Information Systems for Resource Management in Developing Countries*. pp. 31-53. Kluwert. Dordrecht.
- BEVEN, K. J. (2001): *Rainfall-Runoff Modelling. The Primer*. Wiley & Sons. Chichester.
- BOATENG, E. A. (1959): *A Geography of Ghana*. Cambridge University Press. Cambridge.

- CAMPBELL, J. B. (1996): Introduction to Remote Sensing. 2nd Edition. Taylor & Francis. London.
- CHAVEZ, P. S. Jr. (1989): Radiometric Calibration of Landsat Thematic Mapper Multispectral Images. In: PE&RS (55) No. 9, pp. 1285-1294.
- CHAVEZ, P. S. Jr. (1996): Image-Based Atmospheric Corrections – Revisited and Improved. In: PE&RS (62) No. 9, pp. 1025-1036.
- CHOW, V. T. (ed.)(1964): Handbook of Applied Hydrology. A Compendium of Water-resources Technology. McGraw-Hill. New York.
- DICKSON, K. D./BENNEH, G. (1995): A new Geography of Ghana. 3rd Revised Edition. Longman. London.
- DVWK (ed.)(1996): Ermittlung der Verdunstung von Land- und Wasseroberflächen. Merkblätter zur Wasserwirtschaft, H. 238. Wirtschafts- und Verl.-Ges Gas und Wasser. Bonn.
- EAGLESON, P. S. (1970): Evaporation and Transpiration. In: EAGLESON, P. S. (1970): Dynamic Hydrology. pp. 211-241. McGraw-Hill. New York.
- FRAZIER, P. S./PAGE, K. J. (2000): Water Body Detection and Delineation with Landsat TM Data. In: PE&RS (66), No. 12, Dec. 2000, pp. 1461-1467.
- FRIESEN, J. (2002): Spatio-temporal Rainfall Patterns in Northern Ghana. Diploma Thesis University of Bonn. (Submitted).
- GAO, B.-C. (1996): NDWI – A Normalized Difference Water Index for Remote Sensing of Vegetation Liquid Water From Space. In: Remote Sens. Environ. Vol, 58, pp. 257-266. Elsevier. New York.
- GHANA STATISTICAL SERVICE (2000): Poverty trends in Ghana in the 1990's. Ghana Statistical Service. Accra.
- GLOWA VOLTA PROJECT PROPOSAL (1999): Sustainable Water Use under Changing Land Use, Rainfall, and Water Demands in the Volta Basin. ZEF. Bonn.
- GLOWA VOLTA ANNUAL REPORT 2001 (2002): Sustainable Water Use under Changing Land Use, Rainfall Reliability and Water Demands in the Volta Basin. ZEF. Bonn.
- GRAF, W. L. (1988): Fluvial Processes in Dryland Rivers. Springer Series in Physical Environment 3. Springer. Heidelberg.
- HAYWARD, D./OGUNTOYINBO, J. (1987): Climatology of West Africa. Hutchinson. London.
- HOBBS, M. T./RAMÍREZ, J. A./BROWN, T. C. (2001): The complementary relationship in estimation of regional evapotranspiration: An enhanced Advection-Aridity model. In: Water Resources Research (37), No. 5, 2001, pp. 1389-1403.
- ILOEJE, N. P. (1980): A New Geography of West Africa. New Revised Edition. Longman. London.
- JENSEN, J. R. (1995): Introduction to Digital Image Processing: A Remote Sensing Perspective. 2nd Edition. Prentice-Hall. New Jersey.

- KAMARA, S. I. (1986): The origins and types of Rainfall in West Africa. In: *Weather* No. 41, pp. 48-56.
- KASEI, C. N. (1988): The Physical Environment of Semiarid Ghana. In: UNGER, P.W./SNEED, T. V./JORDAN, W. R./JENSEN, R. (eds.)(1988): *Challenges in Dryland Agriculture – A Global Perspective*. Texas Agricultural Experiment Station, pp. 350-354. TAES. Texas.
- KASEI, C. N. (1990): A Synopsis on the Climate of the North of Ghana. Presented at the 2nd workshop on improving farming systems in the savanna zone of Ghana. April 24-26 1990. Nyankpala Agricultural College. Nyankpala-Tamale, Ghana.
- KITE, G./PIETRONIRO, A. (2000): Remote Sensing of Surface Water. In: SCHULTZ, G. A./ENGMAN, E. T. (eds.)(2000): *Remote Sensing in Hydrology and Water Management*. pp. 217-238. Springer. Heidelberg.
- KNIGHTON, D. (1998): *Fluvial Forms and Processes. A new Perspective*. Arnold. London.
- KOUTSIAS, N./KARTERIS, M./CHUVIECO, E. (2000): The Use of Intensity-Hue-Saturation Transformation of Landsat-5 Thematic Mapper Data for Burned Land Mapping. In: *PE&RS* (66), No. 7, pp. 829-839.
- KONDRATYEV, K. Y./FILATOV, N. N. (eds.)(1999): *Limnology and Remote Sensing. A Contemporary Approach*. Springer-Praxis Series in Remote Sensing. Springer. Berlin.
- LEDGER, D. C. (1964): Some Hydrological Characteristics of West African Rivers. In: *Transactions and Papers*. Institute of British Geographers. Publication No. 35, Dec. 1964. pp. 73-90.
- LEROUX, M. (2001): *The Meteorology and Climate of Tropical Africa*. Springer-Praxis Books in Environmental Sciences. Praxis Publishing. Chichester.
- LHOMME, J.-P. (1997): Towards a rational definition of potential evaporation. In: *Hydrology and Earth System Sciences* (1), No. 2, 1997, pp. 257-264.
- LILLESAND, T. M./KIEFER, R. W. (2000): *Remote Sensing and Image Interpretation*. 4th Edition. Wiley & Sons. New York.
- MANAVALAN, P./SATHYANATH, P./RAJEGOWDA, G. L. (1993): Digital Image Analysis Techniques to Estimate Waterspread for Capacity Evaluations of Reservoirs. In: *PE&RS* (59), No. 9, Sept. 1993, pp. 1389-1395.
- MANDELROT, B. B. (1983): *The Fractal Geometry of Nature*. W. H. Freeman. New York.
- MARCINEK, J./ROSENKRANZ, E. (1996): *Das Wasser der Erde*. 2nd Edition. Perthes. Gotha. pp. 161-177.
- MATHER, P. M. (1999): *Computer Processing of Remotely-Sensed Images. An Introduction*. 2nd Edition. Wiley & Sons. Chichester.
- MEIJERINK, A. M. J./BROUWER, H. A. M./MANNAERTZ, C. M./VALENZUELA, C. R. (1994): Introduction to the use of geographic information systems for practical hydrology. UNESCO International Hydrological Programme IHP-IV M 2.3. Publication No. 23. ITC. Enschede.

- McFEETERS, S. K. (1996): The use of the Normalized Difference Water Index (NDWI) in the Delineation of open water features. In: *Int. J. Remote Sensing* (17), No. 7, 1996, pp. 1425-1432.
- MONTEITH, J. L. (1981): Evaporation and surface temperature. In: *Quart. J. Roy. Met. Soc.* (107), No. 451, 1981, pp. 1-27.
- NEW, M./HULME, M./JONES, P. (1999): Representing Twentieth-Century Representing Twentieth-Century Space-Time Climate Variability. Part I: Development of a 1961-1990 Mean Monthly Terrestrial Climatology. In: *Journal of Climate* (12), No. 3, 1999, pp. 829-856.
- NEW, M./HULME, M./JONES, P. (2000): Representing Twentieth-Century Space-Time Climate Variability. Part II: Development of 1901-1996 Monthly Grids of Terrestrial Surface Climate. In: *Journal of Climate* (13), No. 13, 2000, pp. 2217-2238.
- OBOLI, H. O. N. (1978): A new outline Geography of West Africa. 8th Edition. Harrap Books. London.
- OGUNTUNDE, P. G. (in progress): The dynamics of Evapotranspiration and Complimentary Relations in the Water Balance of the Volta Basin. Dissertation in progress at the Center for Development Research. University of Bonn.
- OJO, O. (1977): The Climates of West Africa. Heinemann. London.
- PENMAN, H. L. (1948): Natural evaporation from open water, bare soil and grass. In: *Proceedings of the Royal Society of London. Series A. Mathematical and Physical Sciences* (193), 1948, pp. 120-145.
- PETERS, M./TETZLAFF, G./JANSSEN, W. (1989): Rainfall intensity of West African Squall Lines. In: *Annales Geophysicae* (7), No. 3, 1989, pp. 227-237.
- PRESS, F./SIEVER, R. (1991): *Allgemeine Geologie*. Spektrum Akademischer Verlag. Heidelberg.
- REES, W. G. (2001): *Physical Principles of Remote Sensing*. 2nd Edition. Cambridge University Press. Cambridge.
- RITCHIE, J. C./SCHIEBE, F. R. (1986): Monitoring suspended sediments with remote sensing techniques. In: JOHNSON, A. I. (ed.)(1986): *Hydrologic Applications of Space Technology*. IAHS Publication No. 160. pp. 233-243. IAHS Press. Wallingford.
- SAGAR, B. S. D./GHANDI, G./RAO, B. S. P. (1995): Applications of mathematical morphology in surface water body studies. In: *Int. J. Remote Sensing* (16), No. 8, 1995, pp. 1495-1502.
- SAGAR, B. S. D./VENU, M./RAO, B. S. P. (1995): Distribution of surface water bodies. In: *Int. J. Remote Sensing* (16), No. 16, 1995, pp. 3059-3067.
- SAGAR, B. S. D./RAO, C. B./RAJ, B. (2002): Is the spatial distribution of larger water bodies heterogeneous? Technical Note. In: *Int. J. Remote Sensing* (23), No. 3, 2002, pp. 503-509.

- SARAF, A. K./CHOUDHARY, P. R./SARMA, B./GHOSH, P. (2001): Impacts of reservoirs on groundwater and vegetation: a study based on remote sensing and GIS techniques. In: *Int. J. Remote Sensing* (22), No. 13, 2001, pp. 2439-2448.
- SCHMIDT-KALLERT, E. (1994): Ghana. Geographische Strukturen, Entwicklungen, Probleme. Perthes Länderprofile. Justus Perthes Verlag. Gotha.
- SCHULTZ, J. (1995): Die Ökozonen der Erde. 2. Auflage. Ulmer. Stuttgart.
- TARBOTON, D. G./BRAS, R. L./RODRIGUEZ-ITURBE, I. (1988): The fractal Nature of River Networks. In: *Water Resources Research* (24), No. 8, 1988, pp. 1317-1322.
- VAN DE GIESEN, N./KUNSTMANN, H./JUNG, G./LIEBE, J./ANDREINI, M./VLEK, P. L. G. (2002): The GLOWA Volta Project: Integrated Assessment of Feedback Mechanisms between Climate, Landuse, and Hydrology. In: BENISTON, M. (ed.)(2002): *Climatic Change: Implications for the Hydrological Cycle and for Water Management. Advances in Global Change Research* (10), 2002, pp. 151-171. Kluwer Academic Publishers. Dordrecht.
- VEIHMEYER, F. J. (1964): Evapotranspiration. In: CHOW, V. T. (1964): *Handbook of Applied Hydrology*. pp. 11-1 – 11-38. McGraw-Hill. New York.
- WEISCHET, W./ENDLICHER, W. (2000): Regionale Klimatologie – 2. Die Alte Welt: Europa, Afrika, Asien. Teubner. Stuttgart.
- WETZEL, R. G./LIKENS, G. E. (1995): *Limnological Analyses*. 2nd Edition, 3rd Print. Springer. New York.
- WHITE, M. E. (1978): Reservoir Surface Area from Landsat Imagery. In: *PE&RS* (44), No. 11, Nov. 1978, pp. 1421-1426.
- WINDMEIJER, P. N./ANDRIESSE, W. (ed.)(1993): *Inland Valleys in West Africa: An Agro-Ecological Characterization of Rice-Growing Environments*. ILRI Publication 52. International Institute for Land Reclamation and Improvement. Wageningen.
- WMO (1974): *International Glossary of Hydrology*. Secretary of the World Meteorological Organization. Geneva.
- WMO (1994): *Guide to Hydrological Practices. Data Acquisition and Processing, Analysis, Forecasting and other Applications*. WMO No. 168. 5th Edition.

WWW - sources

- CRU: CRU05 0.5 Degree 1901-1995 Monthly Climate Time-Series. Climate Research Unit, University of East Anglia, Norwich, UK.
http://www.cru.uea.ac.uk/~markn/cru05/cru05_intro.html (visited 19.04.2002)
- EROS DATA CENTER: ENHANCED THEMATIC MAPPER PLUS (ETM+)
<http://edc.usgs.gov/products/satellite/landsat7.html> (visited 19.05.2002)

- GOND, V./BARTHOLOMÉ, E./OUATTARA, F./NONGUIERMA, A./BADO, L. : Mapping and monitoring small ponds in dryland with the VEGETATION instrument – application to West Africa.
<http://vegetation.cnes.fr/vgtprep/vgt2000/gond.pdf> (visited 24.06.2001)
- GSFC DAAC (2002): NASA GSFC Earth Sciences (GES) Distributed Active Archive Center (DAAC).
http://lake.nascom.nasa.gov/daac-bin/whom/mk_page.cgi.pl?PATH=dataset/TRMM/01_Data_Products/01_Orbital/08_Pr_Prof_2A_25/2001/1 (visited 03.05.2002)
- KARVONEN, T. (2001): Horton Laws. Laboratory of Water Resources. Helsinki University of Technology.
http://www.water.hut.fi/wr/kurssit/Yhd-12.135/kirja/fr_uus_e.htm (visited 17.08.2002)
- KRANJAC-BERISALJEVIC', G./BAYORBOR, T. B./ABDULAI, A. S./OBENG, F. et al. (ed.)(1998): Rethinking Natural Resource Degradation In Semi-Arid Sub-Saharan Africa: The Case of Semi-Arid Ghana. Revised January 1999.
http://www.odi.org.uk/rpeg/soil_degradation/ghlit.pdf (visited: 10.05.2002)
- LANDSAT 7 FACTS
<http://geo.arc.nasa.gov/sge/landsat/17.html> (visited 19.05.2002)
- LANDSAT 7 SCIENCE DATA USERS HANDBOOK
http://ltpwww.gsfc.nasa.gov/IAS/handbook/handbook_toc.html (visited 19.05.2002)
- LUPO, F./REGINSTER, I. (2000): Land-Cover Changes in West Africa: Multitemporal change vector analysis as a coarse scale and change processes categorization with SPOT VEGETATION data.
http://www.geo.ucl.ac.be/Recherche/Teledetection/Projects/Lupo_Reginster.html (visited 19.05.2002)
- TRMM (2002): Tropical Rainfall Measuring Mission Homepage.
<http://trmm.gsfc.nasa.gov/> (visited: 03.05.2002)
- USGS GLOBAL VISUALIZATION VIEWER. Landsat 7 ETM+ coverage of Northern Ghana, path 194/row 54.
<http://glovis.usgs.gov/ImgViewer/ImgViewer.html?path=194&row=54&pixelSize=1000&sensor=7> (visited 19.05.2002)
- VONDER, O.W./CLEVERS, J.G.P.W. (1998): Multisensor RS Capabilities Land. Report 1. Chapter 6: Applications of present and future optical remote sensing satellite sensors.
<http://www.geo-informatie.nl/cgi/projects/bcrs/multisensor/report1/6.htm> (visited 24.06.2001)
- WORLD CLIMATE: Navrongo
<http://www.worldclimate.com/cgi-bin/grid.pl?gr=N10W001> (visited 19.05.2002)
- WORLD METEOROLOGICAL ORGANIZATION/UNESCO: International Glossary of Hydrology.

<http://www.cig.ensmp.fr/~hubert/glu/aglo.htm> (visited 15.08.2002)

WORLDWIDE REFERENCE SYSTEM (WRS)

<http://edc.usgs.gov/glis/hyper/guide/wrs.html> (visited 19.05.2002)

Appendices

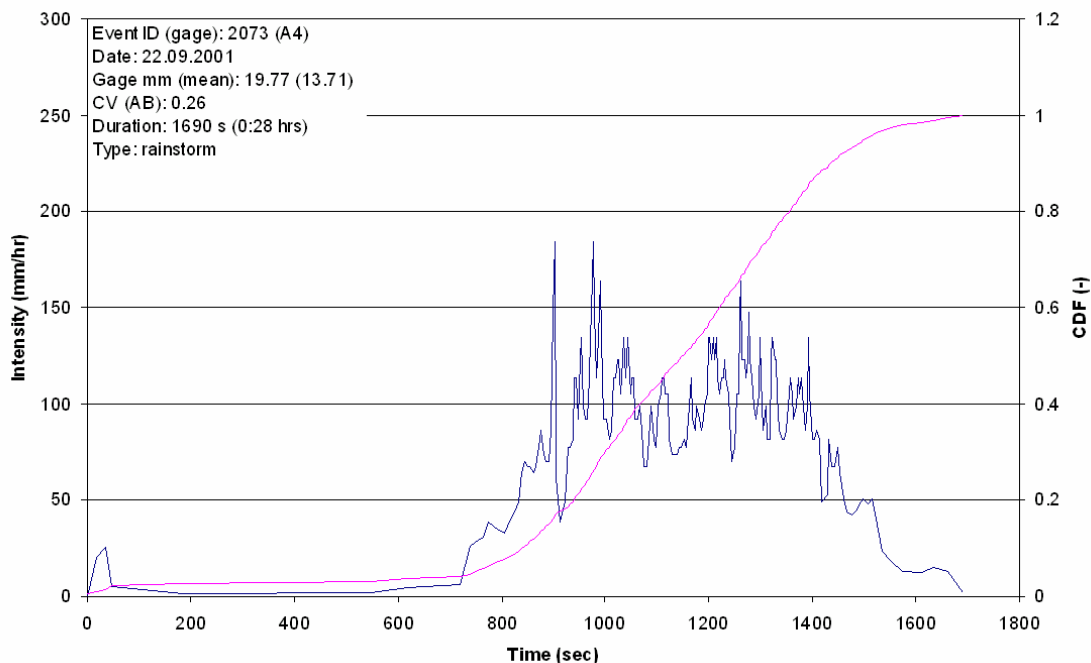
Appendix 1: Summary of Climatic Data at Navrongo

Meteorological Station Navrongo
(Lat.10° 50'N Long. 1°06'W Altitude: 201.3m)

	Jan.	Feb.	Mar.	Apr.	May	Jun.	Jul.	Aug.	Sep.	Oct.	Nov.	Dec.	Average/ Annual
MEAN Temp. °C	27.3	29.8	32.0	32.1	30.5	28.2	26.9	26.4	26.7	28.2	28.1	27.0	28.6
Mean RH (%)	24.0	24.0	35.0	51.0	63.0	72.0	78.0	82.0	81.0	70.0	45.0	30.0	54.6
Sunshine hrs	8.9	8.5	7.7	7.6	8.3	7.9	6.9	6.1	6.9	8.5	9.0	8.5	7.9
Wind speed (km/day)	86	95	95	104	104	95	86	69	60	60	52	69	81
Mean rainfall (mm)	1.0	3.7	18.3	57.4	90.9	125.	193.	265.	173.	48.4	4.8	3.4	986
Radiation (mm/day)	3.58	4.00	4.66	5.18	5.48	5.26	4.98	4.85	5.11	5.26	4.37	5.33	4.69
Pen ET _o (mm/day)	6.00	6.73	6.93	6.68	6.19	5.34	4.73	4.36	4.57	5.20	5.33	5.43	5.62
Pen ET _o (mm/month)	186	188	215	200	192	160	147	135	137	161	160	168	2050

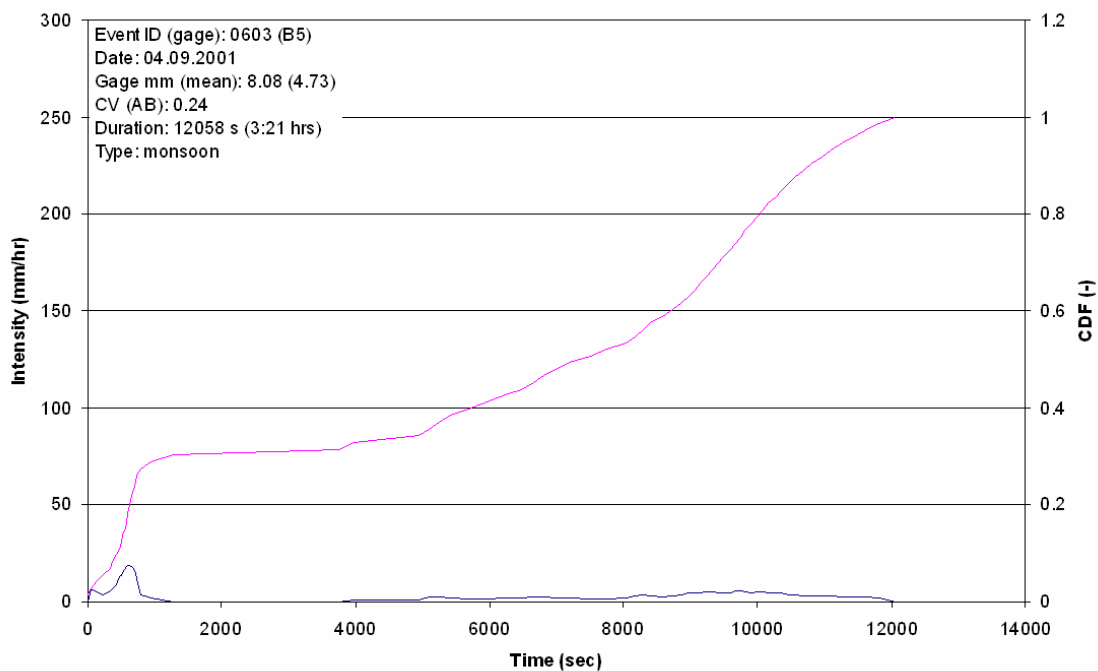
ET_o calculated from long term climatic data (1961-1990) compiled by the Ghana Meteorological Services Department, Accra
(Source: KRANJAC-BERISALJEVIC, G./BAYORBOR, T. B./ABDULAI, A. S./OBENG, F. et al. 1998, pp. 55-56)

Appendix 2: Characteristic Rainfall Patterns for different types of Rainfall



Appendix 2 a: Typical rainfall intensity pattern of a thunderstorm

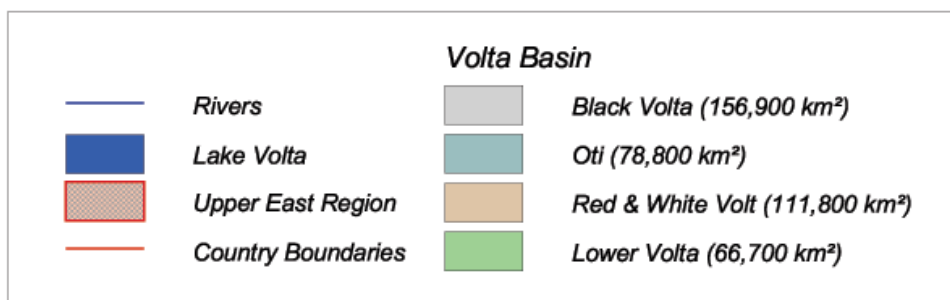
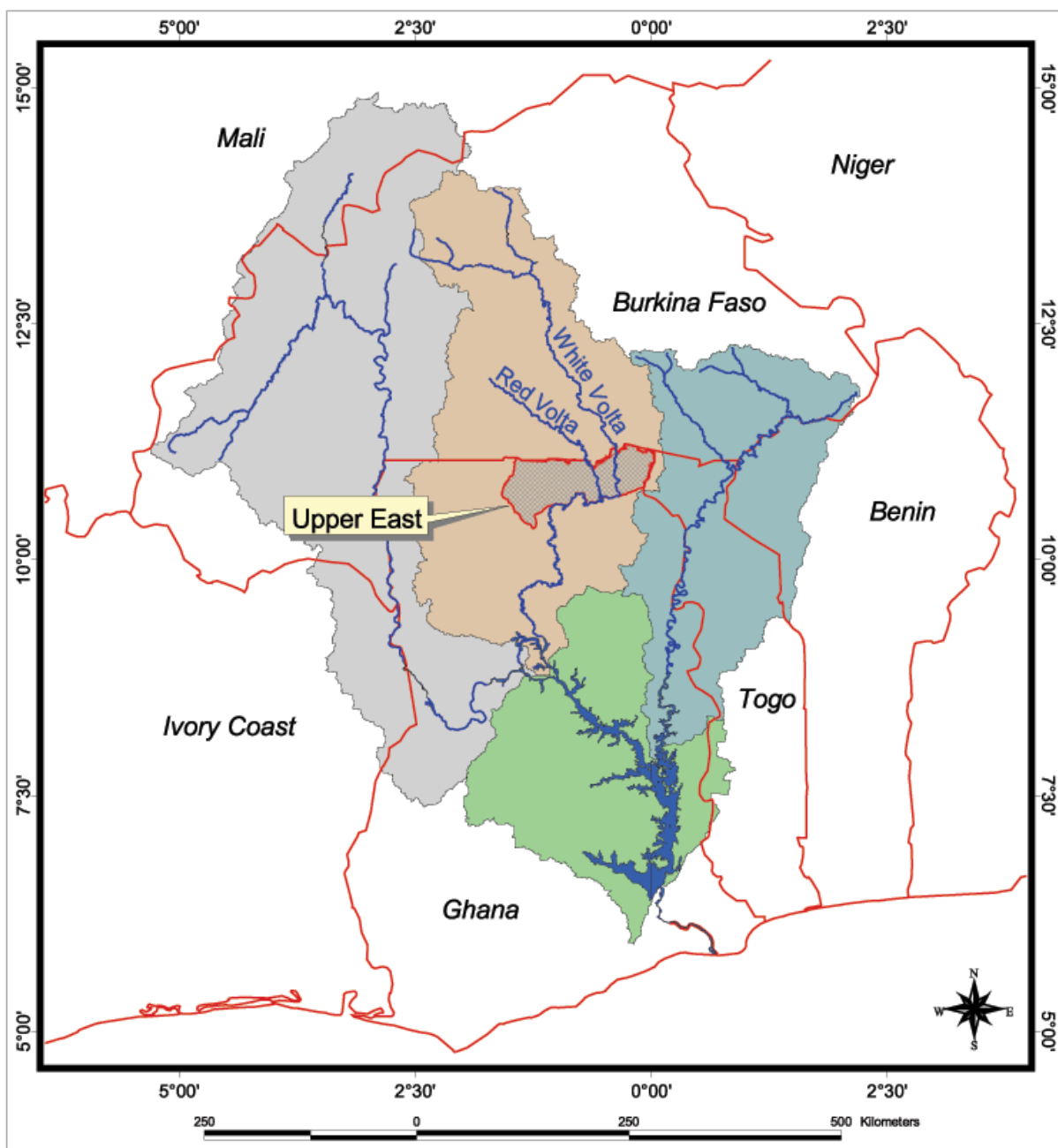
(Source: FRIESEN 2002, p. 76)



Appendix 2 b: Typical rainfall intensity pattern of a monsoonal rainfall event.

(Source: FRIESEN 2002, p. 70)

Appendix 3: The Upper East Region of Ghana within the Volta Basin



Appendix 4: Technical Summary of evaporation calculation with CRU-Data

(P. OGUNTUNDE after M. T. HOBBS/J. A. RAMÍREZ/T. C. BROWN 2001)

(For details, see HOBBS/ RAMÍREZ/ BROWN 2001)

General Penman Equation for potential evaporation

$$\lambda E_p = \frac{\Delta}{\Delta + \gamma} Q_n + \lambda \frac{\gamma}{\Delta + \gamma} E_a,$$

where λ is the psychrometric constant, Δ is the slope of the saturated vapor pressure curve, and Q_n is the net available energy at the surface. E_a represents the “drying power of air” and composes of

$$E_a = f(U_r)(e_a^* - e_a)$$

where $f(U_r)$ is the wind function, (e_a^*) is the saturated vapor pressure, and (e_a) the vapor pressure of the overpassing air.

$$\lambda E_p = \underbrace{\frac{\Delta}{\Delta + \gamma} (R_n - G)}_{P_h} + \lambda \underbrace{\frac{\gamma}{\Delta + \gamma} E_a}_{P_w},$$

thus

$$\lambda E_p = P_h + \lambda P_w$$

$$P_h = \frac{\Delta}{\Delta + \gamma} (R_n - G) = W_1 * W_2$$

$$W_1 = \frac{\Delta}{\Delta + \gamma},$$

$$\text{where } \Delta = \frac{2504 \exp\left(\frac{17.27 T_{mean}}{T_{mean} + 237.3}\right)}{(T + 237.3)^2},$$

and $\gamma = 0.066 K Pa/^\circ C$, T = Temperature (derived from table 2.2 of APPENDIX 2).

The computation of $W_2 = (R_n - G)$ requires

R_n = net radiation

R_a = derived from simple statistical model as a function of latitude

G = ground heat flux

$n/N = f(Octas)$

$R_s = [0.25 + 0.50(f(Octas))]R_a$

$$R_{ns} = (1 - \alpha)R_s = 0.77 R_s \text{ (assumes } \alpha=0.23)$$

$$R_{so} = [0.75 + 2(\text{altitude})/10^5]R_a$$

$$R_{nl} = \frac{\delta}{2} [T_{\max}^{K^4} + T_{\min}^{K^4}] [0.34 - 0.14\sqrt{e_a}] [1.35 R_s / R_{so} - 0.35] = rl_1 * rl_2 * rl_3$$

$$R_n = R_{ns} - R_{nl}$$

To compute the soil heat flux G:

$$G_{month_i} = 0.07(T_{month_{i+1}} - T_{month_{i-1}})$$

or if $T_{month_{i+1}}$ is unknown

$$G_{month_i} = 0.14(T_{month_i} - T_{month_{i-1}})$$

$$P_w = \frac{\gamma}{\Delta + \gamma} E_a = P_{w_1} * P_{w_2}$$

$$P_{w_1} = \frac{\gamma}{\Delta + \gamma}$$

$$P_{w_2} = E_a = \underbrace{0.35(1 + 0.54U_2)}_{ad_1} \underbrace{(e_s - e_a)}_{ad_2} = ad_1 * ad_2$$

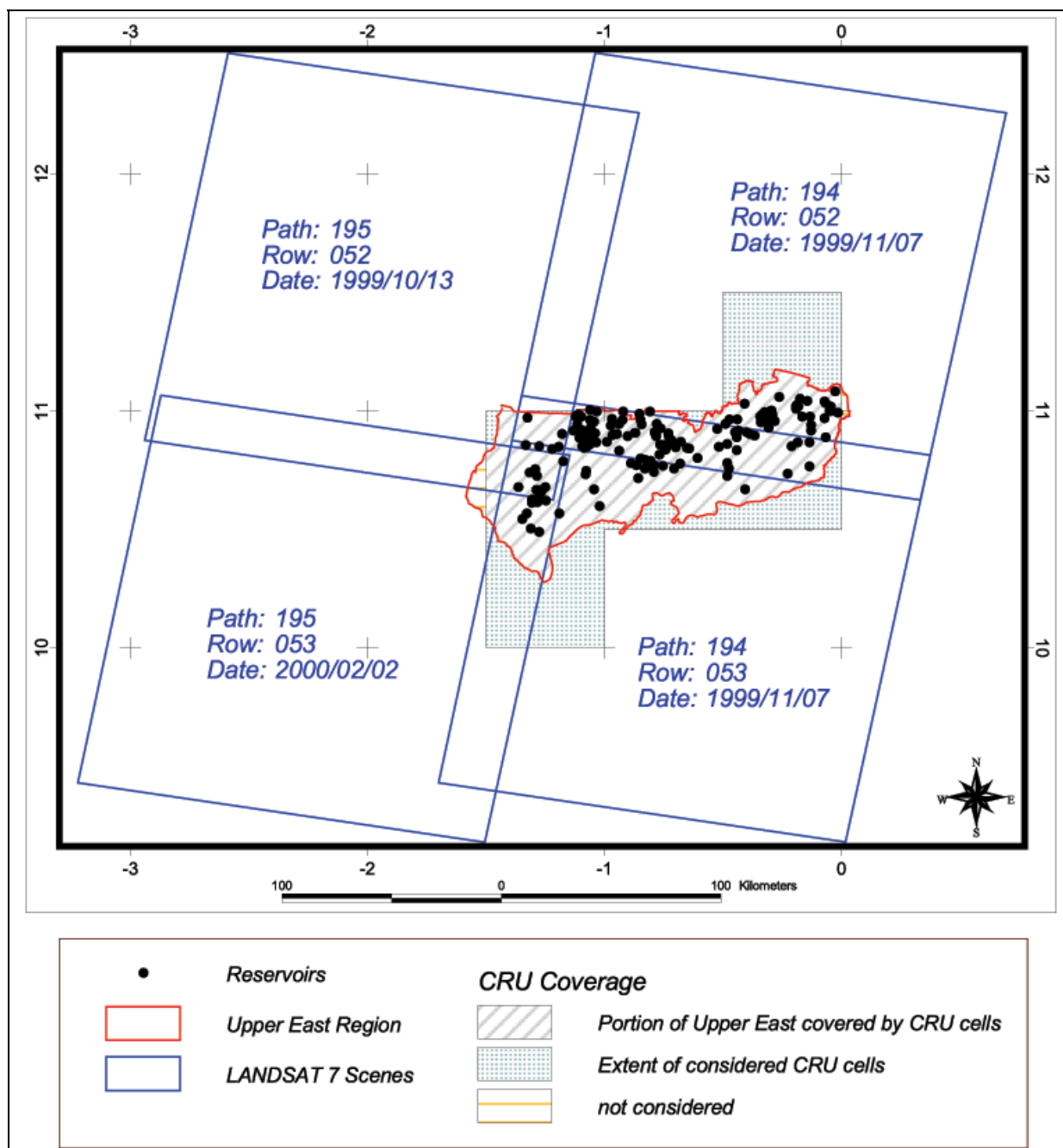
$e_a = \text{given}$

$$e_s = \frac{[e^0(T_{\max}) + e^0(T_{\min})]}{2}$$

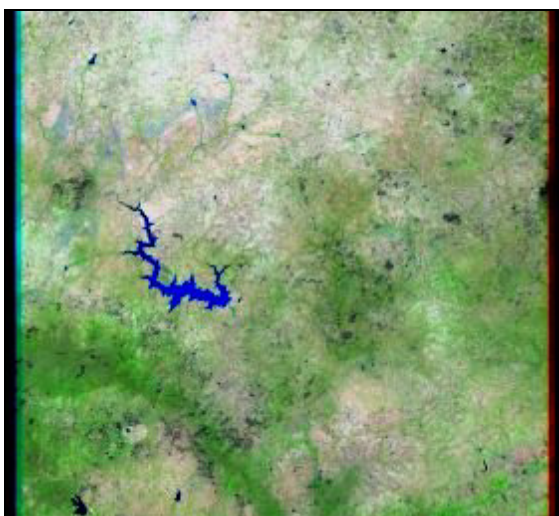
$$e^0(T_{\max}) = 0.611 \exp\left(\frac{17.27 T_{\max}}{T_{\max} + 237.3}\right)$$

$$e^0(T_{\min}) = 0.611 \exp\left(\frac{17.27 T_{\min}}{T_{\min} + 237.3}\right)$$

Appendix 5: Landsat and CRU Coverage

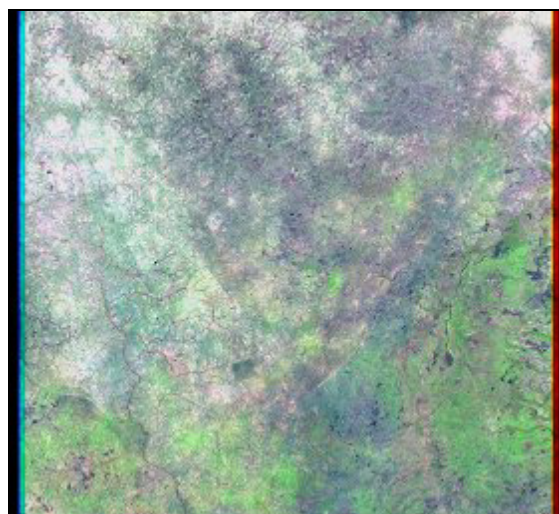


Appendix 6 : LANDSAT ETM+ Scene Parameters



Dataset Attribute	Attribute Value
Scene ID	7194052009931150
Acquisition Date	1999/11/07
WRS Path	194
WRS Row	52
Upper Left	12°30'35"N, 1°02'20"W
Upper Right	12°15'26"N, 0°41'41"E
Lower Left	10°52'31"N, 1°23'25"W
Lower Right	10°37'26"N, 0°20'00"E
Scene Center	11°34'04"N, 0°21'00"W
Cloud Cover	0%
Browse Available	Yes
Day or Night	Day
Flight Path	Descending
Sun Elevation	54.098545
Sun Azimuth	140.242813
Scene Center Time	1999:311:10:13:11.4339148

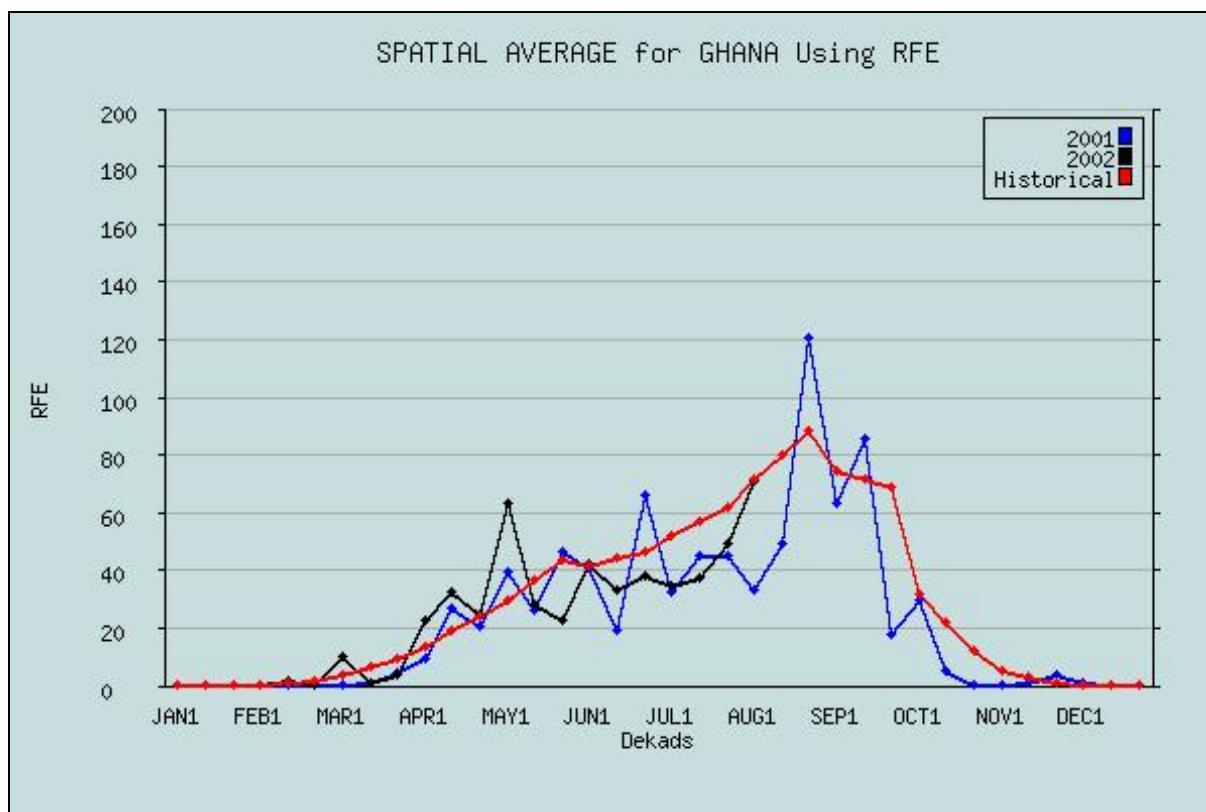
Dataset Attribute	Attribute Value
Scene ID	7194053009931150
Acquisition Date	1999/11/07
WRS Path	194
WRS Row	53
Upper Left	11°03'52"N, 1°21'01"W
Upper Right	10°48'47"N, 0°22'29"E
Lower Left	9°25'49"N, 1°41'59"W
Lower Right	9°10'48"N, 0°01'00"E
Scene Center	10°07'22"N, 0°39'52"W
Cloud Cover	0%
Browse Available	Yes
Day or Night	Day
Flight Path	Descending
Sun Elevation	55.059421
Sun Azimuth	138.656128
Scene Center Time	1999:311:10:13:35.3349763



Dataset Attribute	Attribute Value
Scene ID	7195052009928650
Acquisition Date	1999/10/13
WRS Path	195
WRS Row	52
Upper Left	12'30'34"N, 2'35'18"W
Upper Right	12'15'25"N, 0'51'18"W
Lower Left	10'52'32"N, 2'56'25"W
Lower Right	10'37'28"N, 1'13'00"W
Scene Center	11'34'04"N, 1'53'59"W
Cloud Cover	0%
Browse Available	Yes
Day or Night	Day
Flight Path	Descending
Sun Elevation	59.616997
Sun Azimuth	128.250137
Scene Center Time	1999:286:10:19:28.1321073

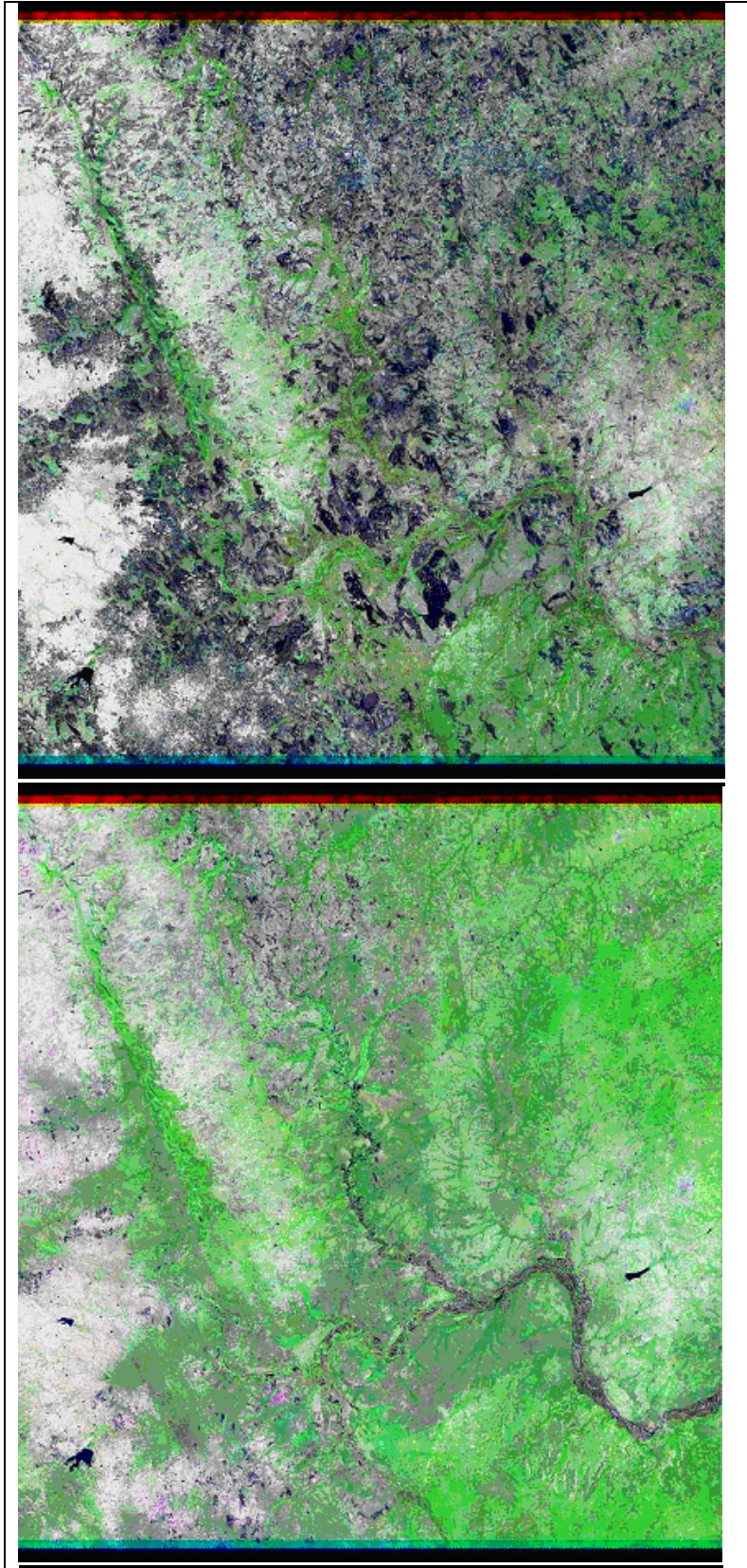
Dataset Attribute	Attribute Value
Scene ID	7195053000003350
Acquisition Date	2000/02/02
WRS Path	195
WRS Row	53
Upper Left	11'03'53"N, 2'52'19"W
Upper Right	10'48'48"N, 1'08'49"W
Lower Left	9'25'47"N, 3'13'19"W
Lower Right	9'10'46"N, 1'30'19"W
Scene Center	10'07'22"N, 2'11'12"W
Cloud Cover	0%
Browse Available	Yes
Day or Night	Day
Flight Path	Descending
Sun Elevation	49.350082
Sun Azimuth	131.496063
Scene Center Time	2000:033:10:19:38.8784959

(Source: USGS Global Visualisation Viewer)

Appendix 7: Spatial Average Rainfall Estimates (RFE) for Ghana

(Source: Africa Data Dissemination Service
<http://edcsnw4.cr.usgs.gov/adds/imgcurves.php?area=GHMILLET&img=RFE>, visited 14.08.2002)

Appendix 8: Effect of Bushfires



Scene 194-053 on the 7 November 1999

Scene 194-053 on the 9 December 1999 with major fire scars

(Source: USGS Global Visualisation Viewer)

Appendix 9: ID and sizes of the randomly selected reservoirs

Category 1

<i>ID</i>	<i>ha</i>
327	2.07
292	1.44
147	1.44
114	1.62
229	2.61
210	2.34
176	1.62
53	2.34
124	2.16
7	1.98
278	1.17
389	2.34
363	1.98
29	2.7
384	1.44
50	1.71
103	1.71
235	1.44
422	1.08
154	1.35
45	2.34
88	1.08
163	2.52
207	2.79
19	2.52

Category 2

<i>ID</i>	<i>ha</i>
63	3.51
20	5.94
1	6.21
91	4.05
304	5.76
247	5.49
268	3.96
358	5.31
182	6.93
286	4.86
179	5.13
72	5.31
224	6.03
181	5.22
90	3.15
9	3.42
230	3.15
421	6.21
96	5.4
238	4.14
227	2.97
105	3.96
151	5.58
42	5.22
206	3.69

Category 3

<i>ID</i>	<i>ha</i>
122	24.57
198	8.37
178	11.88
171	10.53
322	15.84
52	7.02
61	8.73
221	15.75
85	8.73
187	19.8
282	32.49
92	8.1
18	7.38
101	14.58
212	12.87
329	10.17
266	7.83
142	12.51
357	11.43
146	14.58
59	18
133	10.62
306	9.99
137	7.92
100	14.04

The cancelled reservoirs No. 266 and 142 in Category 3 (dam failure) were substituted with the subsequent spares No. 59 and 133.

Appendix 10: Surfer script for 0-replacement of blanking value

(received from Surfer Tech Support)

```
'Blank0.bas replaces the blanking value in a grid file with 0.
' Modified from code by KF. TB - 22 Mar 00.
Sub Main
    'Use existing Surfer 7 instance with a Plot1 window.
    'Set surf = GetObject("Surfer.application")
    'Set plot = surf.Documents("Plot1")

    'Open a new Surfer 7 instance.
    Set surf = CreateObject("Surfer.Application")
    Set plot = surf.Documents.Add(srfDocPlot)
    surf.Visible=True
    Set shapes = plot.Shapes
    Set grid = surf.NewGrid
    grid.LoadFile(GetFilePath( , "grd", "D:\Jens\DiplDataEval\Surfer\Cat1\","Open
Grid File",0),False)

    Debug.Print "Processing GridRow:"
    For row=1 To Grid.NumRows()
    For col=1 To Grid.NumCols()
        If Grid.IsBlanked(row,col) Then Grid.SetNode(row,col,0)
    Next col
    Debug.Print row;
    If row Mod 20 = 0 Then Debug.Print
        Next row
    Debug.Print 'CR
    Grid.SaveFile("D:\Jens\DiplDataEval\Surfer\Cat1\DemoBlank0.grd",
srfGridFmtS7)
    shapes.AddContourMap("D:\Jens\DiplDataEval\Surfer\Cat1\DemoBlank0.grd")

End Sub
```

Appendix 11: Area_(Satellite)-Area_(Field) Deviations in hectares and NDAI

CAT	ID	ha (Sat.)	ha (Field)	NDAI	CAT	ID	ha (Sat.)	ha (Field)	NDAI
Category 1	7	1.98	0.7	-0.4776	Category 3	18	7.38	4.25	-0.2691
	29	2.7	1.63	-0.2471		52	7.02	5.46	-0.1250
	45	2.34	1.37	-0.2615		59	18	11.45	-0.2224
	50	1.71	2.13	0.1094		61	8.73	6.78	-0.1257
	53	2.34	1.7	-0.1584		85	8.73	5.09	-0.2634
	88	1.08	0.66	-0.2414		92	8.1	4.95	-0.2414
	114	1.62	0.93	-0.2706		101	14.58	9.01	-0.2361
	124	2.16	3.7	0.2628		122	24.57	19.49	-0.1153
	147	1.44	0.55	-0.4472		133	10.62	13.53	0.1205
	176	1.62	1.89	0.0769		146	14.58	12.88	-0.0619
	210	2.34	1.65	-0.1729		171	10.53	7.66	-0.1578
	229	2.61	3.99	0.2091		178	11.88	9.98	-0.0869
	235	1.44	0.53	-0.4619		187	19.8	19.4	-0.0102
	278	1.17	1.28	0.0449		198	8.37	6.8	-0.1035
	292	1.44	0.79	-0.2915		212	12.87	13.78	0.0341
	327	2.07	2.15	0.0190		221	15.75	14.12	-0.0546
	363	1.98	1.75	-0.0617		282	32.49	38.28	0.0818
	384	1.44	1.46	0.0069		322	15.84	10.49	-0.2032
	389	2.34	1.73	-0.1499		329	10.17	6.2	-0.2425
	422	1.08	0.87	-0.1077		357	11.43	5.03	-0.3888
Category 2	1	6.21	5.79	-0.0350					
	9	3.42	2.11	-0.2369					
	20	5.94	4.16	-0.1762					
	63	3.51	0.28	-0.8522					
	72	5.31	4.17	-0.1203					
	90	3.15	2.21	-0.1754					
	91	4.05	2.81	-0.1808					
	96	5.4	1.89	-0.4815					
	179	5.13	4.79	-0.0343					
	181	5.22	4.38	-0.0875					
	182	6.93	4.13	-0.2532					
	224	6.03	8.85	0.1895					
	227	2.97	1.6	-0.2998					
	230	3.15	3.38	0.0352					
	238	4.14	3.05	-0.1516					
	247	5.49	4.11	-0.1438					
	268	3.96	5.26	0.1410					
	286	4.86	5.83	0.0907					
	304	5.76	6.34	0.0479					
	358	5.31	2.53	-0.3546					
421	6.21	3.45	-0.2857						

Appendix 12: IDL-Routine to calculate each reservoirs area and volume at all depth steps of 5 cm

```

PRO Reservoirs

;*0 Initialize

; 0.1 File names
filename=STRARR(61)

path='C:\RESERVOIRS\GIS\XYZ_Dat_Cat3\'
filename(41)=path+'-101c3_blancked_scripted0.dat'

CLOSE,2
OPENW,2,'C:\RESERVOIRS\GIS\output3.dat'
FOR filenum=41,60 DO BEGIN          ;Process one file at a time
print,filenum
;*1 Read file

;1.1 Open file

CLOSE,1
OPENR,1,filename(filenum)

;1.2 Determine length of file

teller=0l                          ;Counter
s=""                                ;Dummy variable
WHILE NOT(EOF(1)) DO BEGIN
  readf,1,s
  teller=teller+1
ENDWHILE

;1.3 Define data array
dat={x:0l,y:0l,z:0.}                ;Data structure
data=REPLICATE(dat,teller)          ;Data matrix

;1.4 Read data into array
point_lun,1,0                        ;Point to beginning file
readf,1,data                          ;Fill array
z=data.z                              ;Array with depth data

;*2 Calculate reservoir characteristics

;2.1 Maximum depth
max_d=-MIN(z)                        ;Maximum depth of reservoir
nlevels=fix(max_d/0.05)              ;Number of levels

```

```

;2.2 Define arrays
depth=FLTARR(nlevels+1)           ;Array for depths
depth[0]=max_d
area=FLTARR(nlevels+1)           ;Array for areas
volume=FLTARR(nlevels+1)         ;Array for volumes

;2.3 "Empty" reservoir and calculate area and surface
FOR level=0,nlevels-1 DO BEGIN

;2.3.1 Area & surface
area[level]=total(z lt 0)         ;Surface (=number of all pixels<0)
volume[level]=-total(z)           ;Volume (sum of all pixels)

;3.2.2 Update depth
depth[level+1]=depth[level]-0.05
z=((z+0.05) < 0)                  ;Decrease depth and set z>0 to zero

ENDFOR                               ;Next level

;result=WRITE_SYLK(' C:\ RESERVOIRS \GIS\proef.slk',filename(filenum),startrow=0,
startcol=filenum)
;result=WRITE_SYLK(' C:\ RESERVOIRS \GIS\proef.slk', depth,startrow=1,
startcol=filenum)

PRINTF,2,filename(filenum)
PRINTF,2,'proef'
PRINTF,2,depth
PRINTF,2,'proef'
PRINTF,2,area
PRINTF,2,'proef'
PRINTF,2,volume
PRINTF,2,'proef'

ENDFOR                               ;Next file

CLOSE,/all
PRINT, 'END'
END                                   ;Program

```

Appendix 13: Equation variables for logArea-logVolume Relations

Linear regressions of the form: $y = ax + b$
 Averaged regression $y = 1.5814x - 2.7682$

CAT	ID	EQUATION $y=ax + b$	R^2
Category 1	7	1.4686x -2.6934	0.9887
	29	1.8265x -3.4492	0.9984
	45	1.5287x -2.2481	0.9953
	50	1.8082x -3.7765	0.9973
	53	1.4842x -2.0228	0.9967
	88	1.4878x -2.3772	0.9788
	114	1.6054x -2.7967	0.9836
	124	1.7295x -3.1209	0.9973
	147	1.9082x -3.8355	0.9836
	176	1.8366x -3.4715	0.9883
	210	1.5336x -2.2843	0.9587
	229	1.8701x -3.8763	0.9989
	235	1.4152x -1.8029	0.9944
	278	1.5124x -2.1247	0.9792
	292	1.447x -2.1984	0.9963
	329	1.2983x -1.7023	0.9893
	363	1.7833x -3.1633	0.9453
	384	1.4665x -2.1478	0.9963
	389	1.8468x -3.804	0.9996
	422	1.8652x -3.8627	0.9976
Category 2	1	1.74x -3.3701	0.9856
	9	2.179x -5.609	0.9979
	20	1.6297x -3.0047	0.9928
	63	1.1761x -1.571	0.9958
	72	1.4813x -2.3602	0.9886
	90	2.227x -5.4623	0.9927
	91	1.6252x -2.6462	0.9929
	96	1.6753x -2.7425	0.9968
	179	1.9796x -4.6357	0.9999
	181	1.5889x -2.5533	0.9527
	182	1.9199x -4.529	0.9998
	224	1.4038x -1.9435	0.996
	227	1.941x -4.186	0.9982
	230	1.7104x -3.1015	0.996
	238	1.8941x -3.8524	0.9955
	247	1.4993x -2.2599	0.9791
	268	1.9812x -4.6135	0.9985
	286	1.4874x -2.1975	0.9971
	304	1.7671x -3.5649	0.9949
	358	1.9649x -4.2952	0.9952
421	1.567x -2.6906	0.9908	

CAT	ID	EQUATION $y=ax + b$	R^2
Category 3	18	1.5171x -2.2006	0.9981
	52	1.5594x -2.6268	0.995
	59	1.5161x -2.6616	0.979
	61	1.682x -3.2115	0.9902
	85	1.7317x -3.348	0.9955
	92	1.7193x -3.431	0.9973
	101	1.6524x -3.1331	0.998
	122	1.5635x -2.7728	0.9957
	133	1.4616x -2.157	0.9923
	146	1.5763x -2.7377	0.9966
	171	1.7272x -3.7965	0.9954
	178	1.5034x -2.4392	0.9976
	187	1.6744x -3.2225	0.9983
	198	1.6523x -3.2573	0.9961
	212	1.6805x -3.3133	0.9893
	221	1.706x -3.4816	0.9978
	282	1.6017x -3.0413	0.9973
	327	2.0593x -4.5754	0.9951
	332	1.4769x -2.3824	0.9943
	357	1.6931x -3.1134	0.9977

	R^2	a	b
min	0.9453	1.1761	-5.6090
max	0.9999	2.2270	-1.5710
median	0.9955	1.6524	-3.1015
mean	0.9918	1.6707	-3.0959
std	0.0106	0.2068	0.8902
var	0.0001	0.0428	0.7925
COVAR (a;b)			-0.1757
CORREL (a,)			-0.9705

Appendix 14: Variables for Equations used for logDepth-logVolume extrapolation

Linear regressions of the form: $y = ax + b$

CAT	ID	a	b
Category 1	7	3.64832084	4.42182416
	29	2.1752527	3.42742575
	45	2.56165963	3.01017235
	50	2.18245843	3.87850404
	53	3.06851514	2.73386186
	88	2.90349005	3.52726439
	114	2.92857867	3.58871608
	124	2.24382001	3.43724249
	147	2.06801619	3.52671334
	176	1.97628709	3.43396266
	210	2.9293964	3.18077675
	229	2.07532074	3.76016336
	235	2.94551909	2.57735785
	278	2.21519576	2.96132663
	292	3.19307345	3.32912773
	327	2.02320279	3.74439625
	363	1.83044953	3.34552774
	384	2.75842345	3.1215407
	389	2.10596181	3.75622522
	422	2.12843502	3.73450358
Category 2	1	2.09879862	3.74716566
	9	2.57665761	4.40571683
	20	2.97945267	3.67382978
	63	3.98261133	3.29103019
	72	3.36910479	3.45432822
	90	2.06585821	3.97815755
	91	2.38516784	3.21853327
	96	2.49197894	3.07344364
	179	2.08471981	4.1011352
	181	2.02460344	3.44590562
	182	2.38719917	4.24914078
	224	3.34548869	3.03112109
	227	2.18034959	3.81039332
	230	2.3118278	3.47266247
	238	2.12835885	3.62040323
	247	2.87504266	3.24781781
	268	2.24331863	4.0430948
	286	2.80922134	3.12607731
	304	2.38909614	3.81531137
	358	2.12730228	3.82207966
421	2.48989641	3.57129169	
Category 3	18	2.81368422	2.92915947
	52	2.9662813	3.44619464
	59	3.2595138	3.85012897
	61	2.47554144	3.75675279
	85	2.56499227	3.6491422
	92	2.21938072	3.88965897
	101	2.8305089	3.69717198
	122	2.44680352	3.82264919
	133	2.63125996	3.34989889
	146	2.75891001	3.55362556
	171	2.54145257	4.33857123
	178	2.89712906	3.47307816
	187	2.54064892	3.78491227
	198	2.77460165	3.95028644
	212	2.60748023	3.91399716
221	2.48177809	3.98296721	
282	2.79134544	3.87250366	
329	4.07729443	3.19082437	
332	2.74463183	3.65428411	
357	2.24129191	3.61891701	

	a	b
Avg	2.58970429	3.58065568
Min	1.83044953	2.57735785
Max	4.07729443	4.42182416
STD	0.48170013	0.38877907
CORREL	-0.24701241	

Appendix 15: Variables for Equations used for logDepth-logArea extrapolation

Linear regressions of the form: $y = ax + b$

CAT	ID	a	b
Category 1	7	2.4434472	4.819618216
	29	1.1889848	3.76485333
	45	1.66575867	3.439386711
	50	1.20323438	4.232349588
	53	2.05950137	3.205746939
	88	1.90649815	3.950650864
	114	1.77801969	3.963109624
	124	1.29324375	3.792521243
	147	1.06623612	3.850040948
	176	1.05966596	3.759495353
	210	1.79101744	3.563815409
	229	1.1082396	4.083397423
	235	2.06567065	3.092692271
	278	1.41801699	3.362175564
	292	2.19844987	3.817577964
	327	0.97734595	4.03947493
	363	0.96096205	3.649589073
	384	1.87089795	3.592016654
	389	1.13968503	4.093578889
	422	1.13826976	4.071706012
Category 2	1	1.18375796	4.092312422
	9	1.1853265	4.597576503
	20	1.80412336	4.097182566
	63	3.36031833	4.120118201
	72	2.23720969	3.924757216
	90	0.91652522	4.236792093
	91	1.45525119	3.609649165
	96	1.48225145	3.47198352
	179	1.0531085	4.413454538
	181	1.19791151	3.784180709
	182	1.24341688	4.57212462
	224	2.37251774	3.545482718
	227	1.12031387	4.118153787
	230	1.34523615	3.843979748
	238	1.11812261	3.945581939
	247	1.85740376	3.67823863
	268	1.12965942	4.369056866
	286	1.88137247	3.58040186
	304	1.34317434	4.177296808
	358	1.07621172	4.130365561
421	1.57047525	3.994828068	

CAT	ID	a	b
Category 3	18	1.85035866	3.382198338
	52	1.8882728	3.895693917
	59	2.08178897	4.299325688
	61	1.4537262	4.143545947
	85	1.47141598	4.04148886
	92	1.28597913	4.257507792
	101	1.70599724	4.134139878
	122	1.55316063	4.220898032
	133	1.77636175	3.774199461
	146	1.74206399	3.993098735
	171	1.46216051	4.707893195
	178	1.92206853	3.933188256
	187	1.51380979	4.186156461
	198	1.66808247	4.361287024
	212	1.52678543	4.304926531
	221	1.45098126	4.376052408
	282	1.73629613	4.318563792
	329	3.10162718	3.768521297
	332	1.84587282	4.088786786
	357	1.31910114	3.976878323

	a	b
Avg	1.58397941	3.977240414
Min	0.91652522	3.092692271
Max	3.36031833	4.819618216
STD	0.48618914	0.353165933
CORREL		-0.19145361

Appendix 16: Equation variables for extrapolated logDepth-logVolume Relations

Linear regressions of the form: $y = ax + b$
 Averaged regression $y = 2.4092313x + 3.55260182$

CAT	ID	a	b
Category 1	7	1.911255	3.778990
	29	3.177871	4.180377
	45	1.084769	3.750371
	50	2.889095	2.901984
	53	2.904951	3.679698
	88	1.962354	3.440158
	114	2.635950	3.003259
	124	1.425491	3.719739
	147	2.979269	3.443634
	176	3.213581	2.694086
	210	3.219993	3.856764
	229	2.408467	3.767114
	235	4.789159	3.535989
	278	3.494107	3.439020
	292	2.399230	3.679395
	327	3.194917	3.600523
	363	1.140429	3.842775
	384	2.427621	3.210010
	389	1.826827	3.886833
	422	2.512753	3.069091
Category 2	1	2.803789	3.702965
	9	2.856651	3.575091
	20	2.368606	3.845547
	63	2.138301	3.462802
	72	2.694186	3.325982
	90	2.733171	3.562437
	91	1.652097	3.376780
	96	1.751640	4.209515
	179	1.809088	3.445561
	181	2.902335	3.471742
	182	1.374706	4.061040
	224	1.884604	3.473560
	227	1.411962	4.027031
	230	2.447459	3.822380
	238	2.491415	3.955422
	247	3.022925	3.166690
	268	2.516512	3.937703
	286	2.232956	4.035016
	304	3.487808	2.986188
	358	1.654372	3.703378
421	1.679306	3.805685	

CAT	ID	a	b
Category 3	18	2.239642	3.484932
	52	3.196121	2.560685
	59	1.851673	3.656337
	61	2.950903	3.229520
	85	1.625077	4.040160
	92	2.269461	2.955656
	101	2.698002	3.910877
	122	2.925463	3.089841
	133	3.430234	3.364717
	146	2.224345	3.844885
	171	1.415104	3.707834
	178	4.360187	3.151359
	187	2.731723	3.656839
	198	2.090834	3.647734
	212	1.593347	3.794039
	221	1.536475	3.367004
	282	3.001443	3.116223
	329	1.510742	3.652537
	332	2.333021	3.574911
	357	1.467334	3.470299

	a	b
Avg	2.4092313	3.55260182
Min	1.084769	2.560685
Max	4.789159	4.209515
STD	0.75703887	0.35846981
CORREL	-0.42459364	

Appendix 17: Equation variables for extrapolated logArea-logVolume Relations

Linear regressions of the form: $y = ax + b$
 Averaged regression $y = 1.51716132x - 2.45191019$
 Coefficient of correlation (a;b): -0.95880605

CAT	ID	a	b
Category 1	7	1.30056887	-2.08786858
	29	1.65044462	-2.77352439
	45	1.58243204	-2.43933683
	50	1.18471564	-1.29439217
	53	1.56036852	-2.30806037
	88	1.67580386	-3.01999258
	114	1.60664776	-2.79223029
	124	1.65343966	-2.80790352
	147	1.54946672	-2.58872985
	176	1.70722505	-2.97274334
	210	1.68782575	-2.84840895
	229	1.51529114	-2.38185059
	235	1.54725597	-2.22450207
	278	1.60044716	-2.42532879
	292	1.56029666	-2.59183716
	327	1.44790539	-2.14094333
	363	1.59889222	-2.46829521
	384	1.60427953	-2.64637596
	389	1.32557841	-1.77382322
	422	1.28909195	-1.77850443
Category 2	1	1.61456564	-2.82831712
	9	0.91516467	-0.4571687
	20	1.61017341	-2.91747661
	63	1.42520984	-2.33604359
	72	1.56181489	-2.6907241
	90	1.24429588	-1.42904793
	91	1.66818004	-2.81153506
	96	1.69522725	-2.81671021
	179	1.30537886	-1.70019052
	181	1.57324103	-2.47986883
	182	1.13555006	-1.1648453
	224	1.47008742	-2.22598204
	227	1.47670424	-2.37791753
	230	1.66486925	-2.91479206
	238	1.65605534	-2.87776534
	247	1.58872463	-2.61418866
	268	1.43855465	-2.24496748
	286	1.55496215	-2.47754862
	304	1.65603598	-3.07286912
	358	1.48051438	-2.32102629
421	1.48555072	-2.3596089	
Category 3	18	1.56137002	-2.37887894
	52	1.57777465	-2.70289333
	59	1.54674312	-2.79318832
	61	1.65675389	-3.09772146
	85	1.63055877	-2.91049032
	92	1.42057306	-2.16126755
	101	1.64348956	-3.09145052
	122	1.52502318	-2.59142082
	133	1.51668759	-2.39829927
	146	1.56892676	-2.70244203
	171	1.19798064	-1.43044952
	178	1.51000589	-2.46739505
	187	1.61675466	-2.9456082
	198	1.49357999	-2.55850915
	212	1.64824238	-3.15785941

	a	b
Avg	1.51716132	-2.45191019
Min	0.915165	-3.157859
Max	1.707225	-0.457169
STD	0.15418855	0.51824289
CORREL	-0.95880605	

Appendix 18: Equation variables for extrapolated logArea-logDepth Relations

Linear regressions of the form: $y = ax + b$
 Averaged regression $y = 0.68333521x - 2.73218229$
 Coefficient of correlation (a;b): -0.962744743

CAT	ID	a	b
Category 1	7	0.409258	-1.972467
	29	0.841054	-3.166444
	45	0.600327	-2.064757
	50	0.831093	-3.517477
	53	0.485554	-1.556565
	88	0.524522	-2.072203
	114	0.562423	-2.228946
	124	0.773249	-2.932565
	147	0.937879	-3.610871
	176	0.943694	-3.547812
	210	0.558342	-1.989827
	229	0.902332	-3.684580
	235	0.484104	-1.497186
	278	0.705210	-2.371040
	292	0.454866	-1.736486
	327	1.023179	-4.133107
	363	1.040624	-3.797849
384	0.534503	-1.919943	
389	0.877435	-3.591851	
422	0.878526	-3.577101	
Category 2	1	0.844767	-3.457052
	9	0.843649	-3.878743
	20	0.554286	-2.271010
	63	0.297591	-1.226109
	72	0.446985	-1.754309
	90	1.091077	-4.622668
	91	0.687167	-2.480430
	96	0.674649	-2.342371
	179	0.949570	-4.190883
	181	0.834786	-3.158982
	182	0.804236	-3.677065
	224	0.421493	-1.494397
	227	0.892607	-3.675893
	230	0.743364	-2.857476
	238	0.894356	-3.528756
	247	0.538386	-1.980312
	268	0.885223	-3.867588
286	0.531527	-1.903080	
304	0.744505	-3.110018	
358	0.929185	-3.837875	
421	0.636750	-2.543706	

CAT	ID	a	b
Category 3	18	0.540436	-1.827861
	52	0.529584	-2.063099
	59	0.480356	-2.065207
	61	0.687887	-2.850293
	85	0.679617	-2.746666
	92	0.777618	-3.310713
	101	0.586167	-2.423298
	122	0.643848	-2.717618
	133	0.562948	-2.124680
	146	0.574032	-2.292165
	171	0.683919	-3.219820
	178	0.520273	-2.046331
	187	0.660585	-2.765312
	198	0.599491	-2.614551
	212	0.654971	-2.819602
	221	0.689189	-3.015926
	282	0.575939	-2.487228
329	0.322411	-1.215014	
332	0.541749	-2.215097	
357	0.758092	-3.014840	

	a	b
Avg	0.68333521	-2.73218229
Min	0.297591	-4.622668
Max	1.091077	-1.215014
STD	0.18434176	0.81868882
CORREL	-0.96274474	

Erklärung

Ich versichere, dass ich die Arbeit selbständig verfasst habe, dass ich keine anderen Quellen und Hilfsmittel als die angegeben benutzt und die Stellen der Arbeit, die anderen Werken dem Wortlaut oder dem Sinn nach entnommen sind, in jedem Fall als Entlehnung kenntlich gemacht habe. Das gleiche gilt auch für beigegebene Zeichnungen, Kartenskizzen und Abbildungen.

Bonn, den 02.09.2002

(Jens Liebe)